UNIVERSITY OF CAPE TOWN
IYUNIVESITHI YASEKAPA • UNIVERSITEIT VAN KAAPSTAD

Extending the annular in-plane torsional shear test specimen to applications at high strain rates

Muhsin Osman

Dissertation presented in fulfilment of the requirements for the degree of Master of Science in Engineering specialising in Mechanical Engineering

Faculty of Engineering and Built Environment

University of Cape Town (UCT)

2021

Blast Impact and Survivability Research Unit

Declaration

1. I am presenting this dissertation in fulfilment of the requirements for my degree.
2. I know the meaning of plagiarism and declare that all of the work in the dissertation, save for that which is properly acknowledged, is my own.
3. This dissertation has been submitted to the Turnitin module (or equivalent similarity and originality checking software) and I confirm that my supervisor has seen my report and any concerns revealed by such have been resolved with my supervisor.
4. I hereby grant the University of Cape Town free licence to reproduce for the purpose of research either the whole or any portion of the contents in any manner whatsoever of the above dissertation.

Signed by candidate

Signature

Date

UNIVERSITY OF CAPE TOWN

Abstract

Faculty of Engineering & the Built Environment

Department of Mechanical Engineering

MSc Mechanical Engineering

Extending the annular in-plane torsional shear test specimen to applications at high strain rates

by MUHSIN OSMAN

The in-plane torsion test is a well-established test used for the characterisation of sheet metals. The specimen is intended to deform in planar simple shear and is designed to be machined with a continuous annular shear zone. As a result, there are no "edge effects" or geometric discontinuities to generate instabilities, thus large true strains up to 1 can be achieved. Before this research, the specimen had only been used for material characterisation in the quasi-static regime. The aim of this research was to conduct further quasi-static testing using the in-plane torsion test and to extend its use into the dynamic regime. Quasi-static tests were performed on a quasi-static torsional (QST) system that was designed to be integrated onto a Zwick universal testing machine. Dynamic tests were performed on a modified torsional split Hopkinson bar (TSHB) system. The TSHB system adopted a nested configuration which allowed for a longer incident bar, and thus larger obtainable strains. Two quick-release mechanisms were used, one using a novel reusable wedge and the other using fracture-pins. All specimens were manufactured from Al 1050 H14. Typical results agreed with material test data available in the literature. Both systems attained large strains at near-constant strain rates and together, allowed for material characterisation over a large range of strain rates. Near-uniform deformations were observed for specimens with lower strain gauge widths. An added feature of the specimen was the flat reverse face, which together with the nested configuration of both systems allows for the possibility for full-field DIC measurement in the future. An estimation method for steady-state flow stress is presented with the steady-state flow stress found to be rate dependant. Finally, a relationship between the steady-state flow stress and strain rate for all experimental results is proposed.

Acknowledgements

I wish to thank the following people whose assistance was a milestone in the completion of this dissertation.

First and foremost, I would like to thank my supervisor, Mr Ernesto Ismail. Without his assistance and dedicated involvement in every step throughout the process, this dissertation would have never been accomplished. His advice, support and understanding of my needs as a student, helped bring this project to a successful conclusion.

I would like to pay my special regards to my co-supervisor, Mr Trevor Cloete, for his constant support, availability, and constructive suggestions. His technical knowledge and insight of this work was invaluable.

A special mention must go to Mr Pierre Smith and the rest of the workshop staff who manufactured all the components I needed as well as Mr George Du Plessis and Mr Willie Slaverse who were always willing to assist me when I experienced any electronic problems. Thanks also go to the support and administration staff in the department as well as the technical staff in the Centre for Materials Engineering.

Getting through my MSc required more than academic support, and I have many people to thank for listening and, at times, having to tolerate me over the duration of my degree. I wish to show my gratitude to my colleagues at BISRU, especially Abraar Harneker, who have been unwavering in their personal and professional support during my degree.

Most importantly, none of this could have happened without my family. To my parents who offered encouragement and support throughout my degree and helped me in more ways than I can describe.

Contents

List of Figures

List of Tables

Nomenclature

Δ	change or increment
ε	strain
$\dot{\varepsilon}$	strain rate
γ	shear strain
Ω	Ohm (electrical resistance)
ρ	density
σ	stress
τ	shear stress
θ	angle of twist

A	area
b	width of castellation
b_t	width of castellation opening
C	torsional rigidity
c	wave velocity
D	inner-most diameter
d	diameter of pin holes
D_s	inner-most diameter of castellation
E	Young's modulus
F	force
F_p	effective force per pin
G	shear modulus
H	overall thickness of specimen
h	thickness of gauge section
I	electrical current
i	incident

J	polar moment of inertia
l	length
N	number of pin holes
N_s	number of machined castellations
N_t	number of castellation openings
R	PCD of pin holes
r	moment arm
r	radius
r	reflected
r_i	inner radius
S_e	edge spacing
S_p	pin spacing
T	torque
t	time
t	transmitted
W	width of gauge section
w	wall thickness of tube

BISRU	Blast Impact and Survivability Research Unit
DAQ	Data acquisition
DIC	Digital Image Correlation
FEM	Finite element modelling
FET	Field-effect transistor
JC	Johnson-Cook
PCD	Pitch Circle Diameter
$PPM/°C$	parts per million per degree Celcius
QST	Quasi-static torsional
SHPB	Split Hopkinson Pressure Bar
TSHB	Torsional Split Hopkinson Bar
USB	Universal Serial Bus
WEDM	wire electrical discharge machining
ZA	Zerilli-Armstrong

o	original or initial
t	tube
y	yield
eq	equivalent
nom	nominal
$true$	true or natural

p	plastic
t	total

Chapter 1

Introduction

1.1 Background

Shear deformation is encountered in building construction, designing for mechanical machining, high-speed travel, and impact accidents, among others [1]. Shear testing is therefore required to understand the mechanical response of materials. For small deformations, up to approximately 20 % strain, material models can be used to obtain shear stress and shear strain mechanical properties by converting from tension and compression testing. This conversion rarely holds into the large strain range with axial tests consistently providing higher estimates of flow stress than shear tests provide. Therefore, testing should be performed directly in shear at the relevant temperature, strain and strain rate, to accurately predict the mechanical behaviour of materials at high strain [1].

Tension and compression testing also suffer from complexities such as necking and barrelling, as well as stress states involving both hydrostatic and deviatoric components which makes data interpretation challenging [2]. Many of these difficulties can be eliminated by using a torsion test as it involves only one component of shear stress and shear strain with no hydrostatic component. It also does not suffer from volumetric change which allows for the potential to achieve larger strains.

Accurate material properties are required to build precise computational models. The material properties, which include shear stress, shear strain and shear strain rate, are obtained by performing experimental tests on well-designed experimental systems. A broad range of experimental techniques are therefore required to obtain material properties over a large range of strain rate regimes since material properties for a specific material may vary from the quasi-static regime to the dynamic regime. The most common technique used for testing in the quasi-static regime is uniaxial tensile testing while the most common apparatus for testing in the dynamic regime is the split Hopkinson pressure bar (SHPB). The SHPB has capabilities of strain rates up to 10^4 and accurately determines the material properties for a given material [1].

The aim of this dissertation is to design and develop torsional testing techniques for testing in both the quasi-static and the dynamic testing regimes. A specimen compatible with both systems will be designed and manufactured from sheet metal. The specimen design is a modification of the in-plane torsion specimen. While a great deal of research has been carried out on testing the in-plane torsion specimen in the quasi-static regime, the extension of the specimen to testing in the dynamic regime is research that, to the author's knowledge, has never been attempted before. A further contribution is the ability to test sheet metal dynamically in torsion. Both of these features form a neat and novel contribution.

1.2 Objectives of dissertation

The main objective of this dissertation is to develop a specimen and associated testing apparatus and techniques that can be used to characterise sheet metal over a large range of strain rates. The following tasks are completed as part of the dissertation:

- Design and fabricate a new annular in-plane torsional specimen.
- Design and fabricate the mechanical components of a quasi-static torsional (QST) system.
- Design and fabricate the mechanical components of a torsional split Hopkinson bar (TSHB) system.
- Assemble the QST system apparatus and configure the system with the required instrumentation and data acquisition systems.
- Assemble the TSHB apparatus and configure the system with the required instrumentation and data acquisition systems.
- Develop a MATLAB script to analyse the experimental data and acquire the required material properties for each experiment.
- Propose a relationship between the steady-state flow stress and the strain rate using all experimental data.
- Comment on the performance of the QST and TSHB systems as well as the new annular in-plane torsional specimen over the large range of strain rates.

1.3 Outline of dissertation

A literature review is presented in Chapter 2. The review begins with an overview of some existing shear test specimens. Some existing quasi-static and dynamic torsional testing systems along with some existing constitutive equations for material modelling are then discussed. An in-depth description of the TSHB system's theory, components and instrumentation are presented in Chapter 3, as well as developments in the field of TSHB systems. Chapter 4 reviews the existing work in BISRU pertaining to TSHB systems and critically reviews the existing TSHB systems presented.

Chapters 5-7 cover the design aspect of the dissertation. Chapter 5 presents the design of the annular in-plane torsional specimen including the specifications and geometry. Chapter 6 presents the quasi-static torsional system while Chapter 7 presents the modified torsional split Hopkinson bar system. Chapter 8 documents the data processing procedure while Chapter 9 presents the results of the experimental work. Conclusions and recommendations are discussed in Chapter 10.

Chapter 2

Literature review

This chapter presents an overview of literature pertaining to this dissertation. It begins with a brief discription of shear localization, the investigation of which was a primary motivation for the design of the systems developed in this dissertation. It then reviews five specimen geometries used for the characterisation of materials in shear, as described in literature. A selection of existing quasi-static and dynamic torsional testing devices are then reviewed. Such devices are used to characterise materials over a large range of strain rate regimes. Finally, the chapter reviews some existing constitutive equations for material modelling highlighting the benefits and shortcomings of each.

2.1 Understanding shear localization

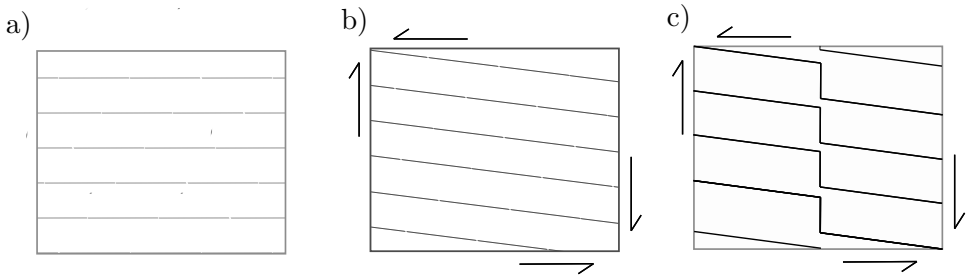

Figure 2.1: Shear localization process, adapted from [3].

Caspar [3] reviewed the mechanism of shear localization which is illustrated in Figure 2.1. Figure 2.1 (a) shows thin lines on the surface of a portion of an undeformed material. When the undeformed material undergoes shear, the thin lines begin to slant at a uniform angle. This deformation is known as homogenous deformation and is shown in Figure 2.1 (b). Further shear in the plastic range leads to the hardening of the material. Non-uniform deformation may begin to occur where some form of weakness exists, such as a discontinuity, scratch, or void, leading to shear occurring at high strain rates near the weakness. This increase in local deformation leads to the plastic heating of the material.

Thermal softening of the material results where there is not enough time for the heat generated to be conducted away from zones where shear occurs at high strain rates. Where the thermal softening dominates the hardening of the material, the strength of the material decreases. As a result, the shear is localized into a thin planar region. This final form is known as shear localization or shear banding and is shown in Figure 2.1 (c).

2.2 Shear test specimens

Current shear test specimens can be divided into two categories: translational fixture movements and rotational fixture movements [4].

2.2.1 Translational shear test specimens

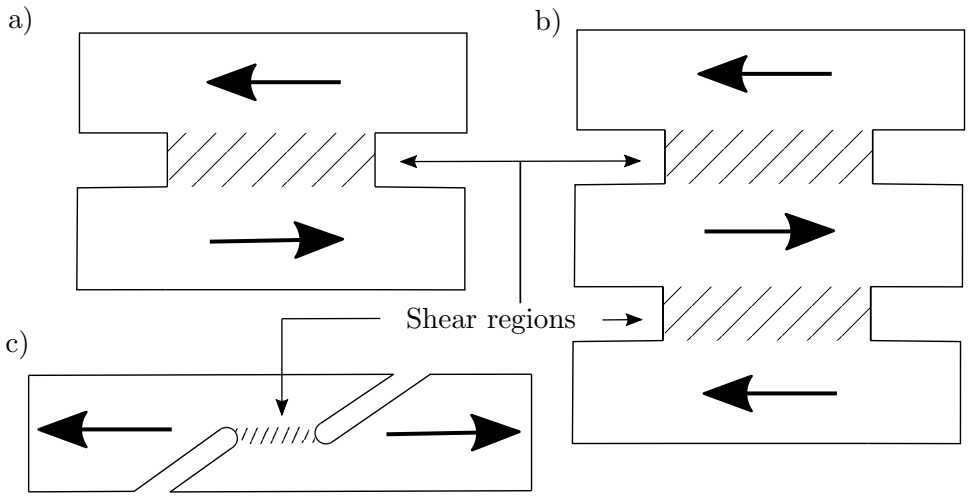

Figure 2.2: Translational shear test specimens, adapted from [4].

Translational fixture movements (where axial or radial displacement of the edge of the specimen drives deformation) typically involve the relative displacement of two opposing edges in opposite directions with a single sided shear specimen, shown in Figure 2.2 (a) [4]. However, the resultant motion produces an unwanted reaction moment on the clamping fixtures [5]. To avoid this, Miyauchi [6] suggested a specimen with the same kinematics but with two symmetrical shear zones, shown in Figure 2.2 (b). The three bars of the specimen were all clamped, with the two shear zones being the regions connecting the bars. Shear deformation was achieved by applying an opposing axial load to the middle bar resulting in deformation in the connecting regions. However, this resulted in the rotation of the principal stress direction in the two shear zones. Premature failure due to stress concentrations at the edges can be reduced by adding slits at the free edges in the specimen. An et al. [7] indicated that the response is also dependent on the geometry (especially the length of the shear zone) of the specimen.

ASTM B831 [8] specifies a specimen involving diagonal cuts that can be compatible with testing devices designed for tensile tests, shown in Figure 2.2 (c). This resulted in a much simpler clamping configuration and evaluation. However, the kinematics led to the possibility of a rotating shear zone during deformation. The single shear zone allowed for the material response to be studied in greater detail compared to the Miyauchi specimen [8]. The shear stress is calculated using the tensile force required to maintain a parallel movement of the two lateral grips. A very stiff clamping tool and well aligned fixture device both reduce the rotation.

2.2.2 Rotational shear test specimens

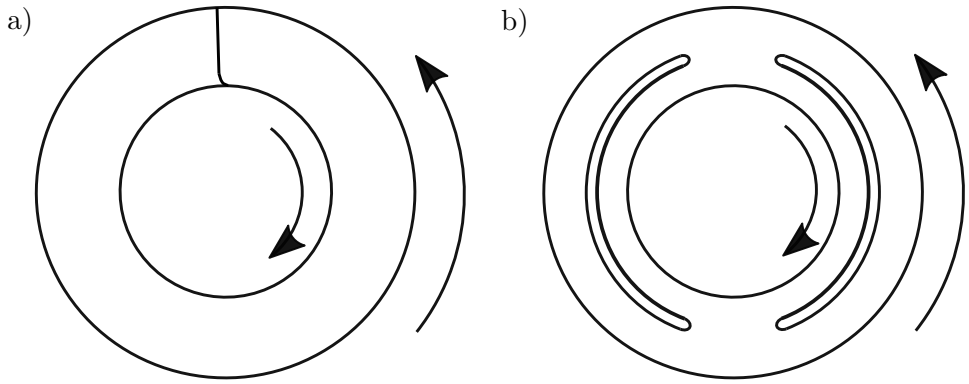

Figure 2.3: Rotational shear test specimens, adapted from [4].

Rotational fixture movements typically involve the rotation of the outer rim of a round sheet specimen relative to its centre. Marciniak [4] proposed a round sheet specimen clamped concentrically at the centre and the outer rim, with shear deformation occurring in the annulus between the clamps, shown in Figure 2.3 (a). This resulted in torsion in the sheet plane between the clamps. Further development of the specimen led to an in-plane torsion test developed by Tekkaya et al. [9] which was used for flow curve determination. Due to there being no edges in the specimen and therefore no edge effects, large deformations could be achieved. The so called "twin bridge shear test" with round slits proposed by Brosius et al. [10] allowed for a shear test with specific orientation to the rolling direction, shown in Figure 2.3(b). Instead of a force couple, the loading is applied as a moment therefore no additional unwanted reaction moment has to be compensated for by the clamping fixtures [4].

2.3 Quasi-static and dynamic torsional devices

This section briefly reviews some existing quasi-static and dynamic torsional testing systems with emphasis placed on understanding the method of loading and the strain rate testing capability of the testing system.

2.3.1 Baker and Yew quasi-static design

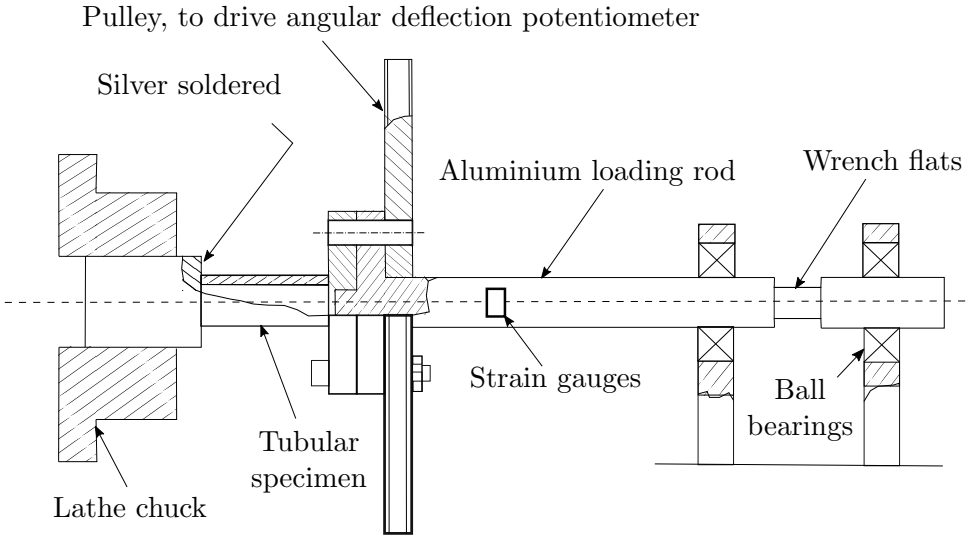

Figure 2.4: Baker and Yew quasi-static design, adapted from [11].

Baker and Yew [11] designed the quasi-static system shown in Figure 2.4. The experimental apparatus was incorporated on a standard lathe bed where one end of the specimen was fixed in the lathe chuck and the other end was attached to a bearing-supported loading rod. A tubular specimen was used and the torque was applied by the twisting of the loading rod. The loading rod was machined from high-strength aluminium due to its relatively low shear modulus that allowed for good accuracy in the measurement of relatively low magnitude torque. Strain gauges located on the loading rod were used to measure the torque applied to the specimen while the angular motion of the specimen end of the loading rod drove a single-turn precision wire-wound potentiometer that was used to measure the angle of twist. In order to resolve the angular motion of the specimen (down to approximately 0.03 °), the angular motion of the specimen was multiplied using a pulley arrangement. A lever fitted to the wrench flats of the loading rod acted as the mechanism through which the twisting moment was applied. A winding of a cable on a slowly rotating shaft system which connected to the lever was used for the lowest shear strain rate (approximately 4×10^{-4} /s) while the twisting moment was applied by hand for the highest shear strain rate (approximately 3×10^{-1} /s), which was the largest obtainable with this arrangement. Shear stress values of approximately 62 MPa and shear strains of approximately eight percent were recorded.

2.3.2 Hydraulic torsion test machine

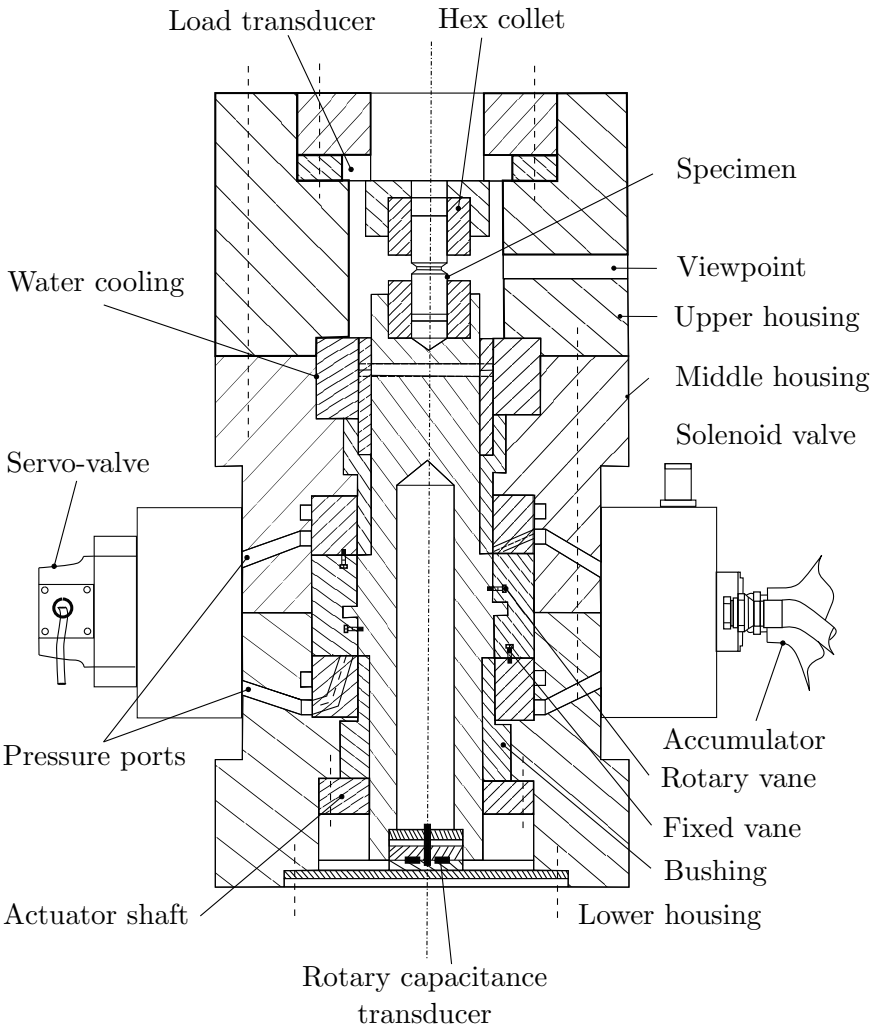

Figure 2.5: Hydraulic torsion test machine, adapted from [1].

The high-speed hydraulic machine, shown in Figure 2.5, employed a torsional actuator instead of the standard linear hydraulic actuator commonly found in axial test machines [1]. A stiff loading system and reaction frame together with low inertia moving parts were required, which was achieved by enclosing the system. The enclosing of the system introduced axial loads which could not be compensated for. The system also featured an integral shaft, specimen and load transducer and had a vane torsional actuator that allowed for a rotation of approximately 170 °.

The system can be used for both quasi-static and dynamic testing. This is achieved by firstly employing a servo valve and servo control-loop for operating at low velocities while using a solenoid-triggered quick release valve that conveys pressure from an accumulator directly to the actuator at high velocities. Shear strain rates of approximately 10 /s are obtainable in the quasi-static regime while shear strain rates up to 300 /s are obtainable in the dynamic regime. To facilitate maintenance of alignment and coaxiality, the rotary actuator shaft, specimen and load transducer are built into the machine thus requiring no transient mechanical engagement or impact. However, at higher speeds the specimen undergoes rapid acceleration resulting in the load transducer experiencing resonance and inertial effects.

Shear stresses results are inferred from the load transducer which consists of a strain gauge element placed between the specimen and the upper housing while the rotation is obtained from a rotary capacitance transducer attached to the actuator shaft. A thin-walled cylindrical specimen with a gauge length of 3.2 mm and 6.4 mm inner radius is used.

2.3.3 Torsional impact machine

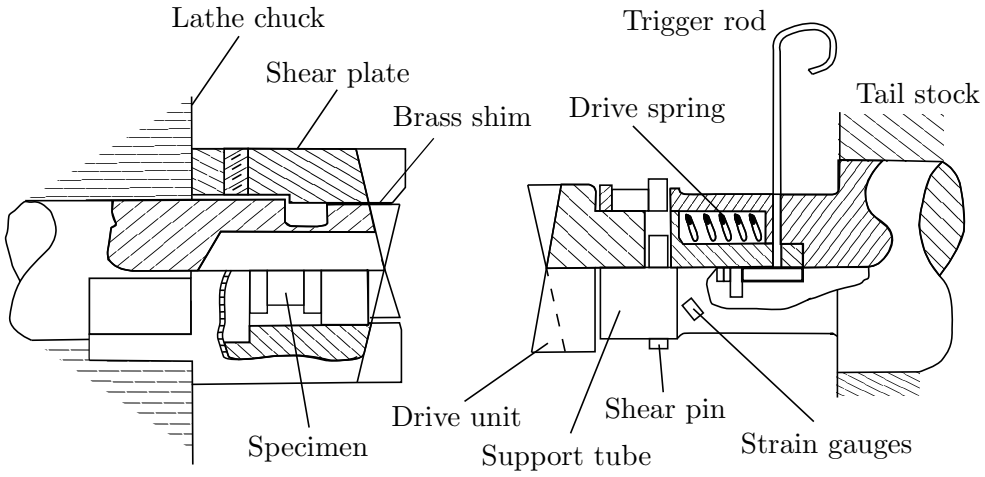

Figure 2.6: Torsional impact machine, adapted from [12].

The key components of torsional impact loading are summarised in [1]. Torsional impact loading methods have the potential to test materials at strain rates of up to 10^3 /s. Specimens were first manufactured as solid, round specimens but more recently, short thin-walled tubular specimens have been used. These specimens obtain nearly homogeneous stress and strain states. Such an apparatus makes use of a drive mechanism, an engagement mechanism, as well as a stationary supported mechanism. A drive shaft or flywheel acts as the driving mechanism and stores the energy required to deform the specimen. The driving mechanism is first brought up to speed, after which the engagement mechanism couples the torsional load to the specimen. Important requirements for the system are the alignment and concentricity of the drive mechanism and specimen, data acquisition systems with adequate frequency response, a load mechanism with high stiffness and low inertia and the ability to maintain a near-constant strain rate in the specimen by supplying sufficient energy via the drive mechanism.

Such a system is shown in Figure 2.6 which utilises a commercial lathe bed and drive mechanism [12]. The specimen is rotated in the lathe chuck. The lathe chuck has a speed range of 500 rpm to 2000 rpm and is brought up to speed before engagement with the specimen. Once the drive mechanism is brought up to the correct speed, a release mechanism, in this case a trigger rod, allows a compressed spring to engage the drive mechanism with the specimen using mating tapers.

2.4 Constitutive equations for numerical modelling

According to Peroni et al. [13], understanding the behaviour of materials at different strain rates and temperatures is fundamental to accurately reproducing the material response in finite element based modelling (FEM). These properties include material properties such as yield strength, ultimate strength, total elongation, a plastic flow curve and work-hardening. The preciseness of the finite element based model depends on the chosen constitutive equation which generally describes the inelastic flow of materials under quantified loading conditions. Under the assumption of incompressibility in the plastic regime, the true stress vs true plastic strain curve can be obtained by subtracting the elastic strain component from the nominal stress vs nominal strain curve.

2.4.1 Literature review

Prusty et al. [14] reviewed some of the existing constitutive equations and described the benefits and shortcomings of each. Factors influencing their success include applicability, accuracy and computational cost. The stress in a body can be expressed as a function of various inputs, known as a constitutive equation. In this work, stress is expressed as a function of the strain, strain rate and temperature fields.

$$\sigma = f(\varepsilon, \dot{\varepsilon}, T) \quad . \tag{2.1}$$

Two material models that are extensively used in the modelling of the rate-dependent plastic deformation of metals are the Johnson-Cook (JC) model and the Zerilli-Armstrong (ZA) model. Both models describe the temperature and strain rate dependence as well as strain-hardening of metals. The JC model attempts to capture strain hardening with a power law and rate sensitivity with a logarithmic relationship. The model is visco-plastic and does not include kinematic hardening. The model is also isotropic and has been used to accurately represent the yield and plastic flow bahaviour of variuos metals [15]. The JC model is available in most commercial FEM codes. This makes the model easy to implement and use. The equation for the JC model is expressed as

$$\sigma = \left[A + B\varepsilon_{pl}^{n}\right]\left[1 + Cln\left(\frac{\dot{\varepsilon}_{pl}}{\dot{\varepsilon}_{pl(0)}}\right)\right]\left[1 - \left(\frac{T - T_r}{T_m - T_r}\right)^{m}\right] \tag{2.2}$$

where A is the yield stress at the reference strain rate and temperature, B is the strain-hardening coefficient, C is the strain rate hardening coefficient, $\dot{\varepsilon}_{pl(0)}$ is the reference plastic strain rate, T_r is the reference temperature, T_m is the melting temperature, m is the thermal softening exponent and n is the strain hardening exponent. The first set of brackets represent the strain dependence, the second set represents the strain rate dependence, and the third set represents the temperature dependence.

The ZA model is based on thermal activation analysis and incorporates the effects of the hardening due to strain and strain rate as well as thermal softening. Lee et al. [16] found the ZA equation to be in good agreement with experimental results for tests conducted on low, medium, and high carbon steels subjected to dynamic compression. The constitutive equation for the ZA model can be expressed as

$$\sigma = c_0 + c_1\varepsilon_{pl}^{n} + c_2\exp[(-c_3 + c_4 \ln \dot{\varepsilon}_{pl})T] \tag{2.3}$$

where c_0 is the athermal stress component, c_1 is the work hardening coefficient, ε_{pl} is the plastic strain, c_2 is the thermal stress coefficient, c_3 is the thermal softening coefficient, c_4 is the temperature coefficient and strain rate coupling term, $\dot{\varepsilon}_{pl}$ is the dimensionless plastic strain rate, n is the work hardening component and T is the current absolute temperature.

Majzoobi et al. [17] used a combination of Johnson-Cook (JC), Zerilli-Armstrong (ZA) and power-law-plasticity (PL) to model tensile and compression experiments on two different plain carbon steels. The JC model and ZA model were found to accurately predict the flow behaviour of the materials. The authors found the PL model was not appropriate, attributing its failure to the absence of the temperature effect. The equation for the PL model is expressed as

$$\sigma = K\varepsilon_{pl}^{n}\dot{\varepsilon}_{pl}^{m} \tag{2.4}$$

where K is the strain hardening coefficient, n is the strain hardening exponent and m is the strain rate sensitivity. To describe the flow behaviour of DP1000 steel, Song et al. [18] improved the ZA model by introducing a strain-rate sensitivity parameter. This resulted in five material parameters and was found to result in a better correlation and fit compared to the JC model. The improved equation is expressed as

$$\sigma = \sigma_0 + c_1\dot{\varepsilon}_{pl}^{m} + c_5\varepsilon_{pl}^{n} \tag{2.5}$$

where σ_0 is the initial yield strength, c_1 is the strain rate hardening coefficient and c_5 is the strain-hardening coefficient. Kim et al. [19] conducted compressive SHPB tests on Al 1050 H14 and fitted a modified Johnson-Cook model to the experimental results. The model was found to accurately predict the flow behaviour. The modified JC model equation is expressed as

$$\sigma = \left[A + B\epsilon_{pl}^{n}\right]\left[1 + Cln\left(\frac{\dot{\epsilon}_{pl}}{\dot{\epsilon}_{pl(0)}}\right)\right]^{p} \tag{2.6}$$

where A, B, and n can be obtained through quasi-static testing, $\epsilon_{pl(0)}$ is the reference strain rate for quasi-static testing and C and p are the parameters for high strain rate.

Some material models are tailored to specific materials. The above constitutive equations were reviewed due to their assumption of an elasto-plastic stress vs strain relationship and their incorporation of a strain rate effect term. These assumptions match the behaviour of the material tested in this dissertation.

Chapter 3

Torsional split Hopkinson bar testing

In torsional split Hopkinson bar (TSHB) testing, the acquisition of dynamic material properties is done by applying the theory of torsional elastic wave propagation in cylindrical bars. The basic system consists of two bars, an incident bar and transmission bar, with the specimen connecting the two bars. A rectangular wave pulse (the incident wave) is generated in the incident bar and propagates towards the specimen. Upon reaching the specimen, part of the incident wave is reflected back along the incident bar (the reflected wave) while part is transmitted through the specimen into the transmission bar (the transmitted wave). Strain gauges are placed on either side of the specimen to record the three waves and the recorded signals are used to infer the dynamic stress and strain of the specimen. The theory governing the operation of TSHB as well as the existing TSHB systems are discussed in this chapter.

3.1 Components of TSHB

According to Yu et al. [5], a standard torsional split Hopkinson bar setup commonly requires the following components:

1. Two long bars with uniform cross-section. The bars may either be solid or hollow and are commonly known as the incident bar and transmission bar. Hollow bars (tubes) can be used to magnify the amplitude of the recorded signals as well as match the hollow shape of the specimen.

2. A means of generating the torsional wave in the incident bar as well as bearing and alignment fixtures. The alignment fixtures maintain the one-dimensional wave propagation condition by allowing coaxial adjustment and correct alignment.

3. Strain gauges, strain amplifiers as well as a data acquisition system are also required to transfer, magnify, and record the strain histories.

3.2 Elementary requirements

To ensure correctness of experimental results, all experiments should meet the following four elementary requirements [5]:

1. One-dimensional stress wave propagation in the bars should be maintained. Therefore, the bars should be manufactured from isotropic homogeneous materials and should be long and straight with the bars being uniform in the axial direction. The bars should remain in the elastic zone during the experiment and should have a length to diameter ratio that is greater than 20 to readily allow for the separation of the incident and reflected waves.

2. The specimen should be in stress equilibrium which is controlled by three factors; the rise time of the incident wave, the mechanical impedance ratio between the specimen and the bar material, as well as the length of the specimen. Stress equilibrium of the specimen can be facilitated by both a longer rise time of the incident wave and a shorter specimen.

3. A specimen with a thickness to average radius ratio smaller than 0.1. This ensures the uniform pure shear stress state in the specimen cross-section.

4. An appropriate connection method between the specimen and the bars that prevents any damage at the interface.

3.3 Compression vs torsion

One of the most widely used techniques for determining the stress versus strain characteristics of materials at high strain rates is the split Hopkinson pressure bar (SHPB). However, stress wave dispersion effects are a fundamental issue with SHPB testing. Stress wave dispersion effects result due to different frequency components in the compressive pulse having different propagation velocities [20]. This is particularly significant for higher frequency components that travel at a lower velocity than the main pulse. Pulse shaping can be employed to shape the incident pulse and reduce the high frequency component of the loading pulse in order to reduce the stress wave dispersion effect as it significantly affects the experimental accuracy [20].

A nearly homogeneous state of pure shear that eliminates geometric instabilities at large strains is achieved when using torsional loading in conjunction with a thin-walled tubular specimen [21]. The torsional loading condition allows for storage of very large shearing strains as well as ensures that the primary mode torsional waves are not dispersive in the bar [21]. This allows for the study of materials over very large strain regimes.

3.4 Derivation of wave equation

The concept of elastic torsional wave propagation in rods is used in the experiments to acquire the dynamic properties of the tested materials. Using Rao [22], the basic equation for this analysis is derived. Consider a differential element of a cylindrical rod shown in Figure 3.1.

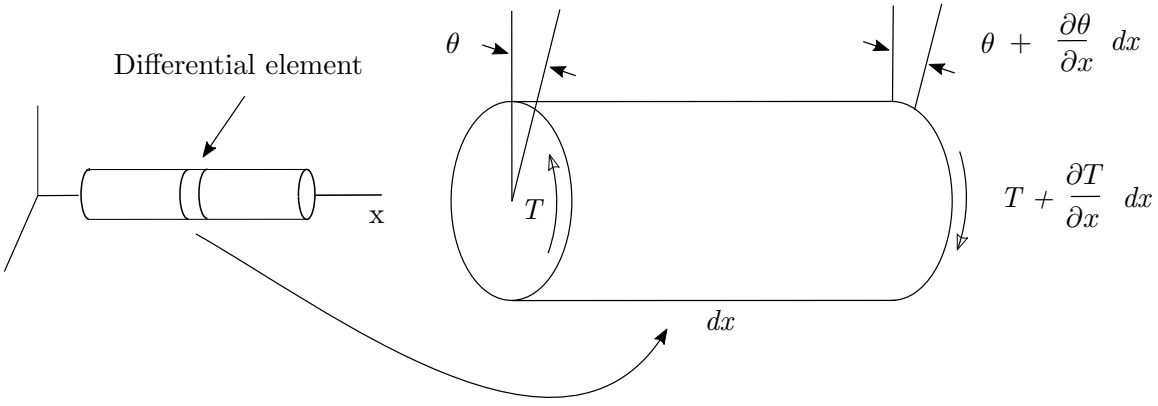

Figure 3.1: Schematic of a rod subjected to a torsional load.

Taking the differential element to represent a portion of the rod subjected to variable torques at either end, from Newton's Law the equation of motion for the differential element becomes

$$-T + \left(T + \frac{\partial T}{\partial x}dx\right) = \rho J \frac{\partial^2 \theta}{\partial t^2} \tag{3.1}$$

where ρ is the density of the rod and J is the polar moment of inertia of the rod. The equation reduces to

$$\frac{\partial T}{\partial x} = \rho J \frac{\partial^2 \theta}{\partial t^2} \quad . \tag{3.2}$$

The torque, T, and the angle of twist, θ, share the kinematic relationship

$$T = C \frac{\partial \theta}{\partial x} \tag{3.3}$$

where C is the torsional rigidity of the rod. This can be calculated by the product of the polar moment of inertia, J, and the shear modulus, G, of the bar. Substituting this relationship into equation (3.3) yields

$$\frac{\partial}{\partial x}\left(JG \frac{\partial \theta}{\partial x} \right) = \rho J \frac{\partial^2 \theta}{\partial t^2} \quad . \tag{3.4}$$

Assuming the rod has a uniform material composition and cross-sectional area, we can simplify the equation to

$$\frac{\partial^2 \theta}{\partial x^2} = \frac{\rho}{G} \frac{\partial^2 \theta}{\partial t^2} \tag{3.5}$$

$$\frac{\partial^2 \theta}{\partial t^2} = c^2 \frac{\partial^2 \theta}{\partial x^2} \text{ with } c = \sqrt{G/\rho} \tag{3.6}$$

where c represents the velocity of the propogation of the torsional wave.

3.5 Elastic wave reflection

According to Rossing et al. [23], who conducted a study on elastic waves in solids, the boundary condition for the case of a free end that occurs when the end of the bar has nothing attached to it is given by

$$\frac{\partial \theta(0,t)}{\partial x} = 0 \quad . \tag{1.16}$$

The boundary condition for the case of a fixed end that occurs when the end of the bar is not permitted any movement, either rotationally, laterally or vertically is given by

$$\theta(0,t) = 0 \quad . \tag{1.17}$$

Assuming the boundary conditions are in their ideal form, then each boundary condition has two important idealised characteristics. For the case of the free end, the reflected wave is of the opposite sign to the incident wave and the displacement doubles in magnitude at the location where the wave reflection occurs. Therefore, the measurements for strain should be at a distance from the free end. For the case of the fixed end, the reflected wave is identical to the incident wave. For this boundary condition, the stresses superimpose to give twice the magnitude at the location where the wave reflection occurs.

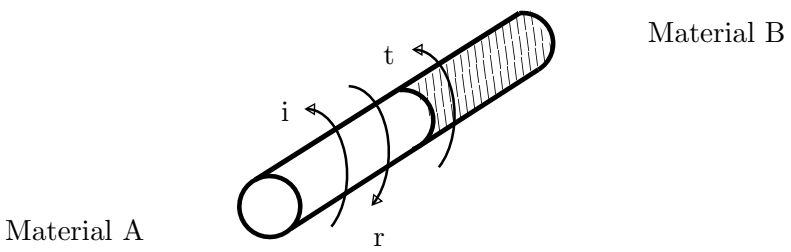

Figure 3.2: Incident,reflected and transmitted waves.

When a travelling wave arrives at an interface, part of the wave is transmitted across the interface and part is reflected. The wave can therefore be divided into three parts: the incident (i), reflected (r), and transmitted (t) waves as shown in Figure 3.2. These phenomena occur because the second material may have a different acoustic impedance that disturbs the momentum balance at the interface. The acoustic impedance is a useful property for characterising the interaction a travelling wave has when it encounters a boundary between two materials [24].

For the case where the impedance differs between the materials, a reflected wave is created to achieve momentum balance. The acoustic impedance is the product of the density of the material and the wave speed of the material [24]. A greater difference in acoustic impedance between the materials results in a smaller transmitted wave and a larger reflected wave. Furthermore, the incident wave will have a magnitude equal to the sum of the reflected wave and the transmitted wave.

3.6 Stress wave propagation

One method for inducing a travelling torsional wave in the bar is the stored elastic energy method that involves the mechanical release of a stored torque. The stored torque is generated by the twisting of one end of the incident bar and holding the bar in place using a clamping mechanism. For reference, stored elastic energy method configurations will be considered to be oriented as in Figure 3.3 with a rigid fixture on the left end of the incident bar and the transmission bar to the right of the specimen, with its right hand end without constraint.

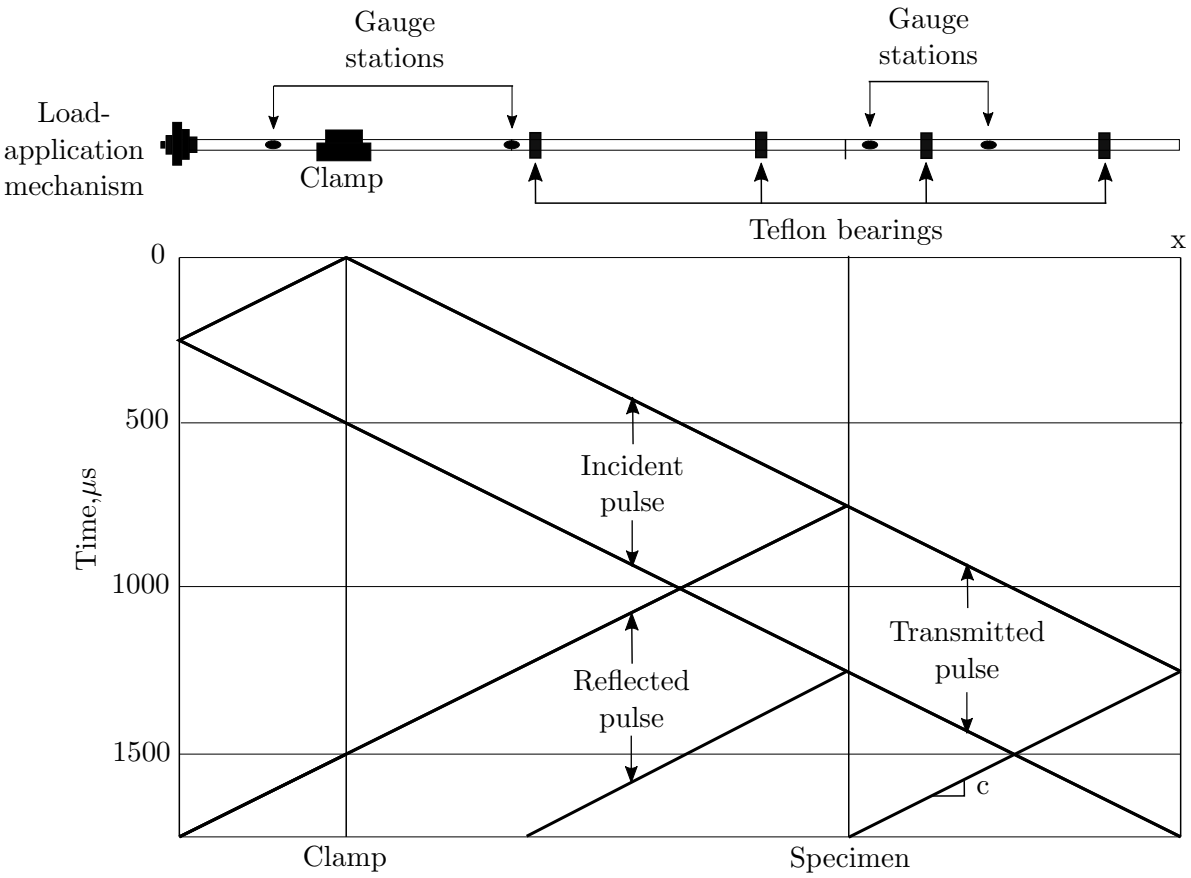

Figure 3.3: Lagrange x-t diagram for split Hopkinson bar testing.

Figure 3.3 shows a Lagrange x-t diagram that illustrates the positioning of the shear wave front as a function of time. The diagram corresponds to the system used and discussed in Chapter 7.

As seen from the diagram, when the clamping mechanism is released, half of the torque stored between the loading end and the clamping mechanism propagates as a wave pulse (at the wave speed of the incident bar) towards the specimen interface. The other half of the stored torque travels at the same speed as a wave pulse towards the loading end and unloads the torque stored at that end. The unloading pulse reflects completely at the loading end and travels towards the specimen interface thereby releasing the torque to zero. The total duration of the shear pulse that acts on the specimen is equivalent to the time taken for the unloading shear pulse to travel toward the loading end and back to the clamping mechanism. Control of the duration of the shear pulse can be achieved by moving the clamping mechanism [25].
The incident bar is split into two regions, the initially isolated clamped region and the free region; with a primary requirement being that the clamped region be significantly shorter than the free region (of the order of 1:4) to allow for the waves to occur independently [26]. Important factors include the cross-section, diameter, and the material of the bars used. Aluminium is the most commonly used material for the bars, but some researchers have used steel and titanium [26].

3.7 Desired wave profile

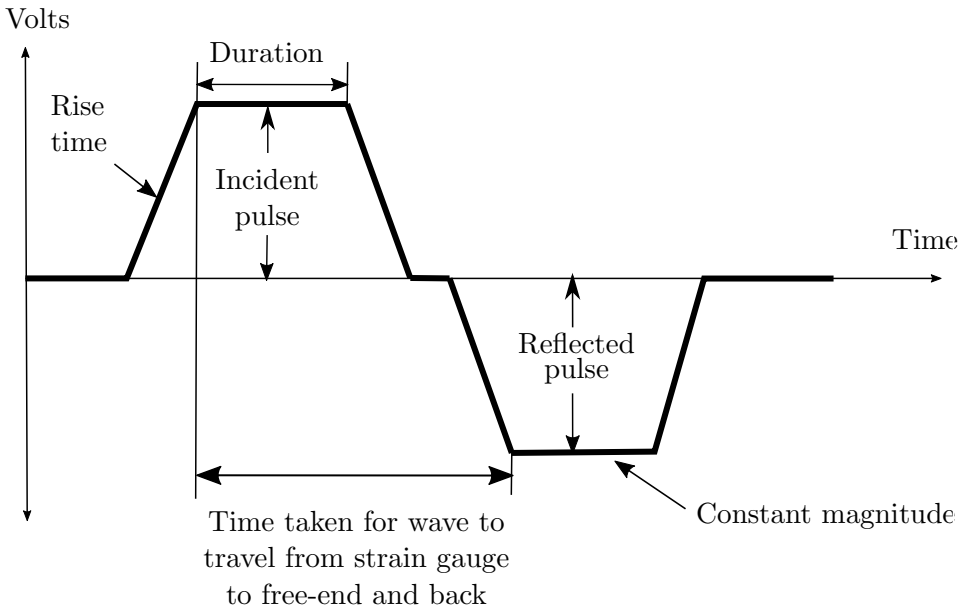

Figure 3.4: Incident and reflected wave profile.

Figure 3.4 shows the important features of the incident wave including its magnitude, rise time and duration. Square waves offer many attractive characteristics but are undesirable for SHPB testing with trapezoidal shaped waves being preferred. This is due to the reduction of high-frequency content from the waves and thus dispersion effects being considerably reduced when increasing the rise time in the incident wave. For the case where a pulse is compounded with many different frequencies, a larger amplitude will lead to an increase in dispersion effects. Correspondingly, dispersion effects are reduced when the amplitude of the wave decreases.

The challenge for investigators has therefore been the trade-off between increasing the rise time thereby reducing the dispersion effects, and allowing for a peak value duration long enough to allow for adequate material characterisation. Since no dispersion is present in TSHB testing, a smooth square pulse is desirable. A square pulse instantaneously rises to a maximum value which allows for constant strain rate tests over long durations.

3.8 Strain measurements

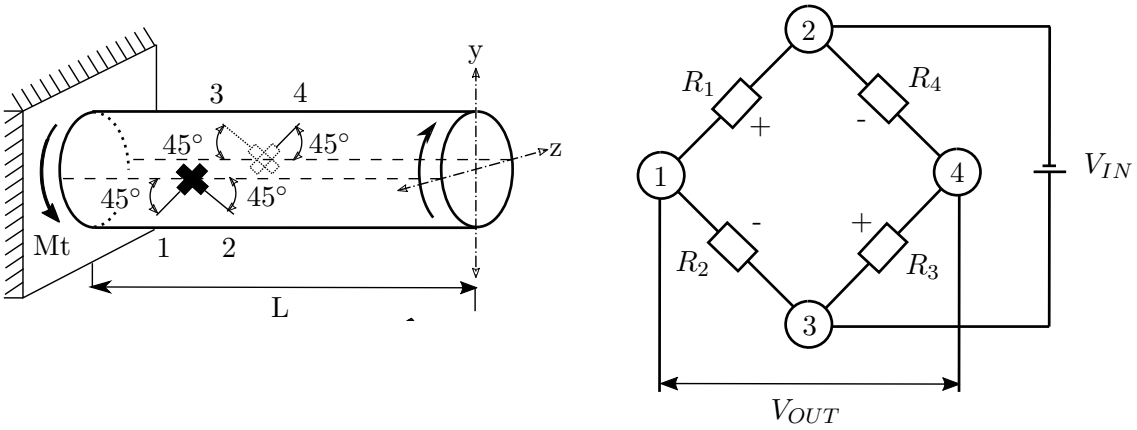

Figure 3.5: Full bridge strain gauge configuration used for torque measurement, adapted from [25].

Figure 3.5 shows the configuration of a strain gauge bridge used for torsional strain measurements. The strain gauges are oriented at a 45 ° angle to the axis of the bar with each pair attached diametrically opposite the other on the surface of the bar. The configuration ensures only shear strains are measured while axial and bending strains are neglected [25].

The relationship between measured strain, ε, and shear strain, γ, is given by

$$\gamma = \mid \varepsilon_1 - \varepsilon_2 \mid = 2\varepsilon \quad .$$

The relationship between shear strain, γ, and torque, T, is given by

$$T = \frac{\pi r^3 G \gamma}{2}$$

where r is the radius of the bar, G is the shear modulus of the bar and γ is the shear strain recorded by the strain gauges [25].

3.9 Existing TSHB systems

This section briefly reviews some of the existing work on TSHB testing systems including some of the methods to generate the torsional wave as well as the design of specimens used in TSHB testing.

3.9.1 Loading mechanisms

According to Yu et al. [5], there are roughly five types of loading mechanisms. These are discussed in this sub-section.

3.9.1.1 Pre-stored loading

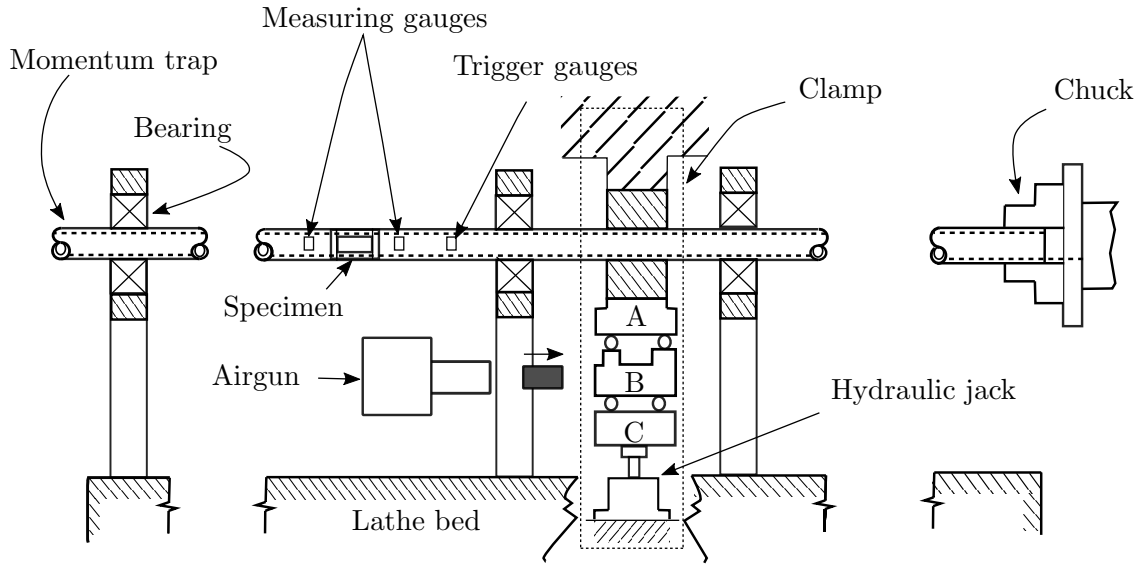

Figure 3.6: Baker and Yew TSHB design, adapted from [11].

Baker and Yew [11] pioneered the work on the TSHB shown in Figure 3.6. Two 4130 steel tubes were used together with two central stands on a lathe bed. One end of the incident tube was firmly clamped in a lathe chuck with the specimen silver-brazed between the two tubes. A specially designed clamp was then placed in the middle of the incident tube and, when engaged, would fix the middle section of the incident tube. An added feature of this system was the extra tube that was employed as a momentum trap. This avoided the transmission of a reflected wave back to the specimen from the free end of the transmission tube. A hydraulic jack provided the clamping force and once the desired torque was applied; the clamp was released by rapidly removing support B with a projectile fired from an airgun. Rise times obtained were approximately 30 μs.

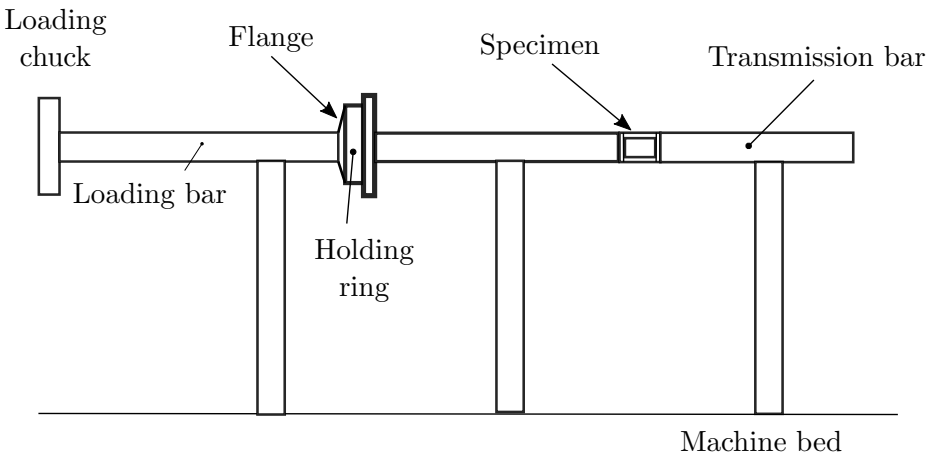

Figure 3.7: Lewis and Campbell TSHB design, adapted from [27].

Lewis and Campbell [27] designed the TSHB configuration shown in Figure 3.7. The clamp consisted of a tapered flange machined at the centre of the loading bar. A fixed holding ring was cemented to the loading bar using an epoxy adhesive. The loading bar was then loaded, in this case using a motor and gear box configuration, until the fracture load of the epoxy adhesive was reached; after which the torsional pulse was generated. Rise times of about 25 μs were produced with the release time being attributed to the time required for a crack to propagate around the cemented joint. After release, the amplitude of the wave remained nearly constant indicating a minimal effect from the friction between the flange and the ring.

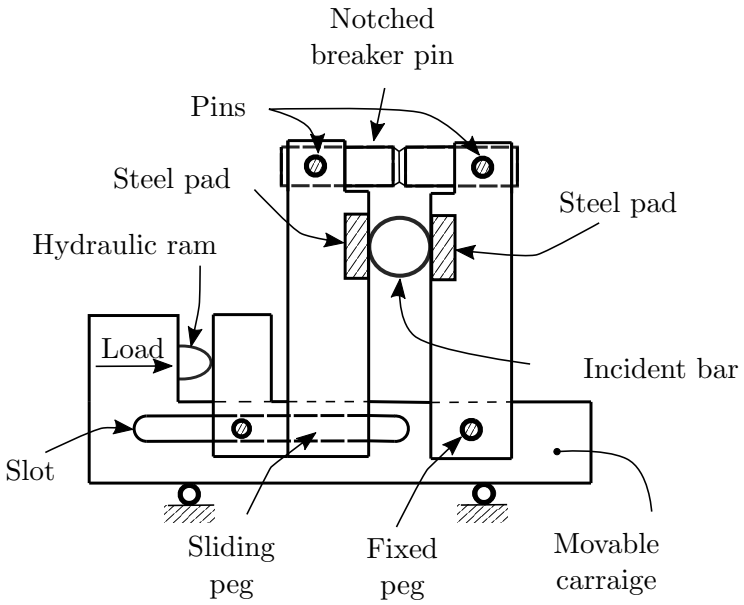

Figure 3.8: Duffy clamp design, adapted from [1].

The friction clamp designed by Duffy [1], shown in Figure 3.8, utilised a hydraulic cylinder to tighten the clamp on the bar. A notched bolt, sometimes referred to as a fracture-pin in other work [28], was used to hold the two jaws together at the top while the bottom of the jaws was hinged to a sliding peg on the one side and a fixed peg on the other. After the desired torque was loaded, the hydraulic pressure was increased until the notched bolt fractured, thereby releasing the torque. Rise times were consistently approximately 100 μs.

3.9.1.2 Explosive loading

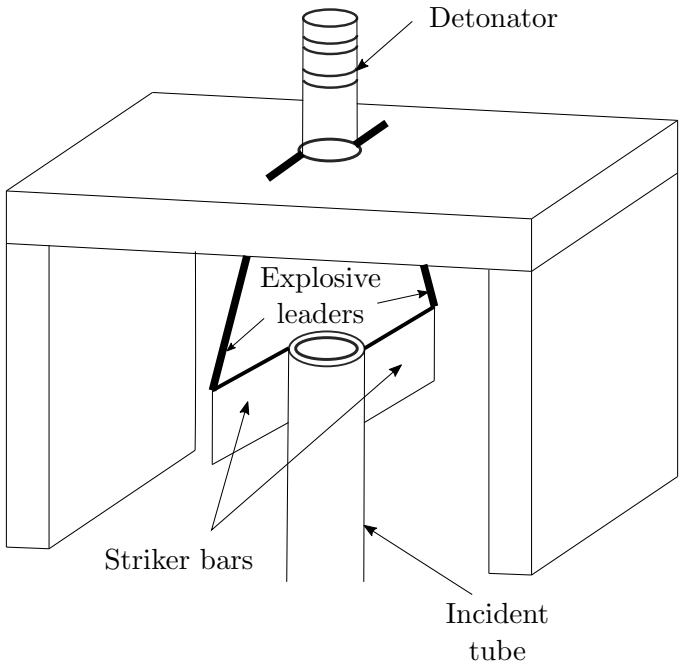

Figure 3.9: Duffy et al. explosive loading TSHB, adapted from [29].

Duffy et al. [29] originally initiated a torsional wave using explosive loading, shown in Figure 3.9, where the experimental apparatus consisted of a split Hopkinson bar loaded in torsion with the tubes being held vertically. Explosives placed at the top end of the incident tube provided the torsional impact once detonated, which induced a torsional pulse that propagated down the tube. Data acquisition was done in the conventional manner using electrical-resistance strain gauges cemented on the surfaces of the tubes. The specimen was cemented to the Hopkinson bar using epoxy adhesive and was machined as a thin section within a short tube (i.e. a tubular specimen).

A layer of sheet explosive was placed at the end of two striker bars which were in contact with short projections at the upper end of the incident tube. This ensured symmetrical loading at the loading end of the incident tube. The two separate layers on the striker bars were then connected to each other by a fine "leader" of explosive. Detonation took place at the centre of this leader with an important detonation criterion being the simultaneity of the two explosions. To ensure a purely torsional wave was generated, equal impulses had to be provided by each explosive, therefore the charge of the explosives had to be the same. Tests showed a time difference of less than 0.1 μs between the two explosive charges.

Due to large amplitude high frequency components superposed on the main pulse, a pulse smoother was added to the experimental apparatus. The pulse smoother was placed in a region between the striker bars and the specimen and could be considered as a dummy specimen. The pulse smoother was found to greatly reduce fluctuations in the magnitude of the torsional pulse. Explosive loading produced a torsional wave with a short rise time of approximately 7-10 μs and short duration. Results for specimens made from 1100-0 aluminium showed strain rates of 800 /s.

3.9.1.3 Impact loading

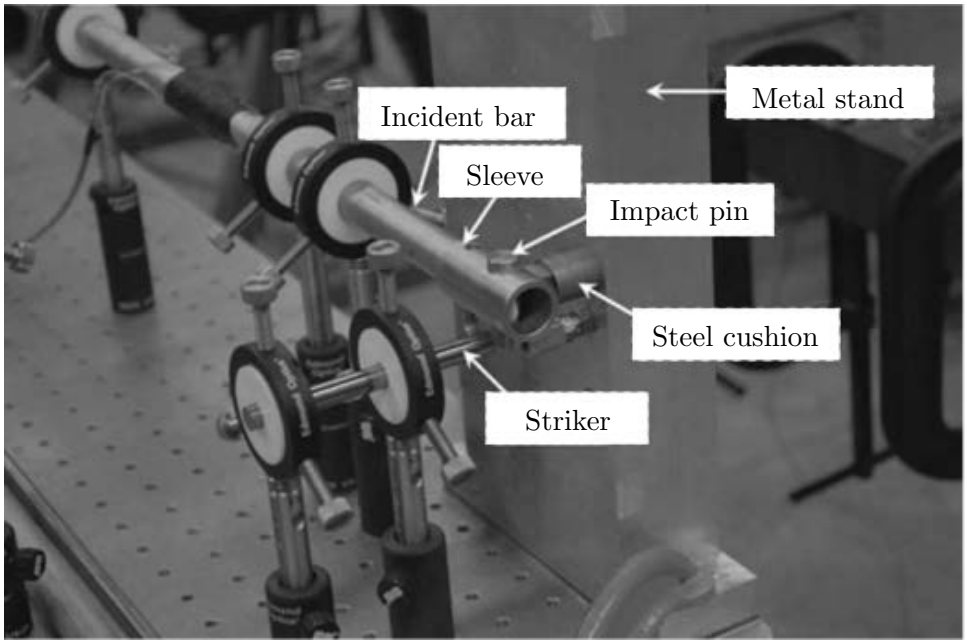

Figure 3.10: Nie et al. direct impact loading TSHB, adapted from [30].

Nie et al. [30] made a first attempt at using direct impact loading as a loading technique as shown in Figure 3.10. A pin was mounted perpendicularly to the axis of the bar at one end of the incident bar. A striker was then used to directly impact the pin which resulted in the generation of the loading pulse. A stainless steel thin-walled hollow tube was used as the incident bar to enhance the measurement of the low-amplitude wave signals generated when characterising soft materials. To ensure even contact upon impact, the bottom side of the pin was flattened and positioned with its flattened side facing the striker. A moment was generated once the striker hit the pin which resulted in the rotation of the incident bar and, due to the non-symmetrical nature of loading, a bending wave was created simultaneously with the torsional wave. To minimise the magnitude of the bending wave, a steel cushion was installed along the circumference at the end of the bar.

Through different combinations of striker velocities and pulse shapers, the incident pulse shape could be easily adjusted to satisfy the required loading conditions for a certain material. The conventional transmission bar was replaced by a torque sensor which directly measured the torque signal at the output end of the specimen. A gel sample was used and bonded to a steel adapter. The steel adapter included an internally geared ring which was engaged to the incident bar and an external ring which was glued directly to the torque sensor. The gear design allowed for fast mounting and dismounting of the specimen. Due to the high stiffness of the load cell assembly as well as the low amplitude of the transmitted load, the external adapter remained stationary allowing for the shear strain to be determined directly from the displacement of the internal ring. Strain gauges mounted on the incident bar measured the input signal.

Rise times ranged from 110-200 μs for the materials tested, with durations ranging from 200-350 μs. Claus et al. [31] modified this technique by replacing the striker with a Hopkinson pressure bar as well as replacing the torque sensor with a transmission tube as shown in Figure 3.11.

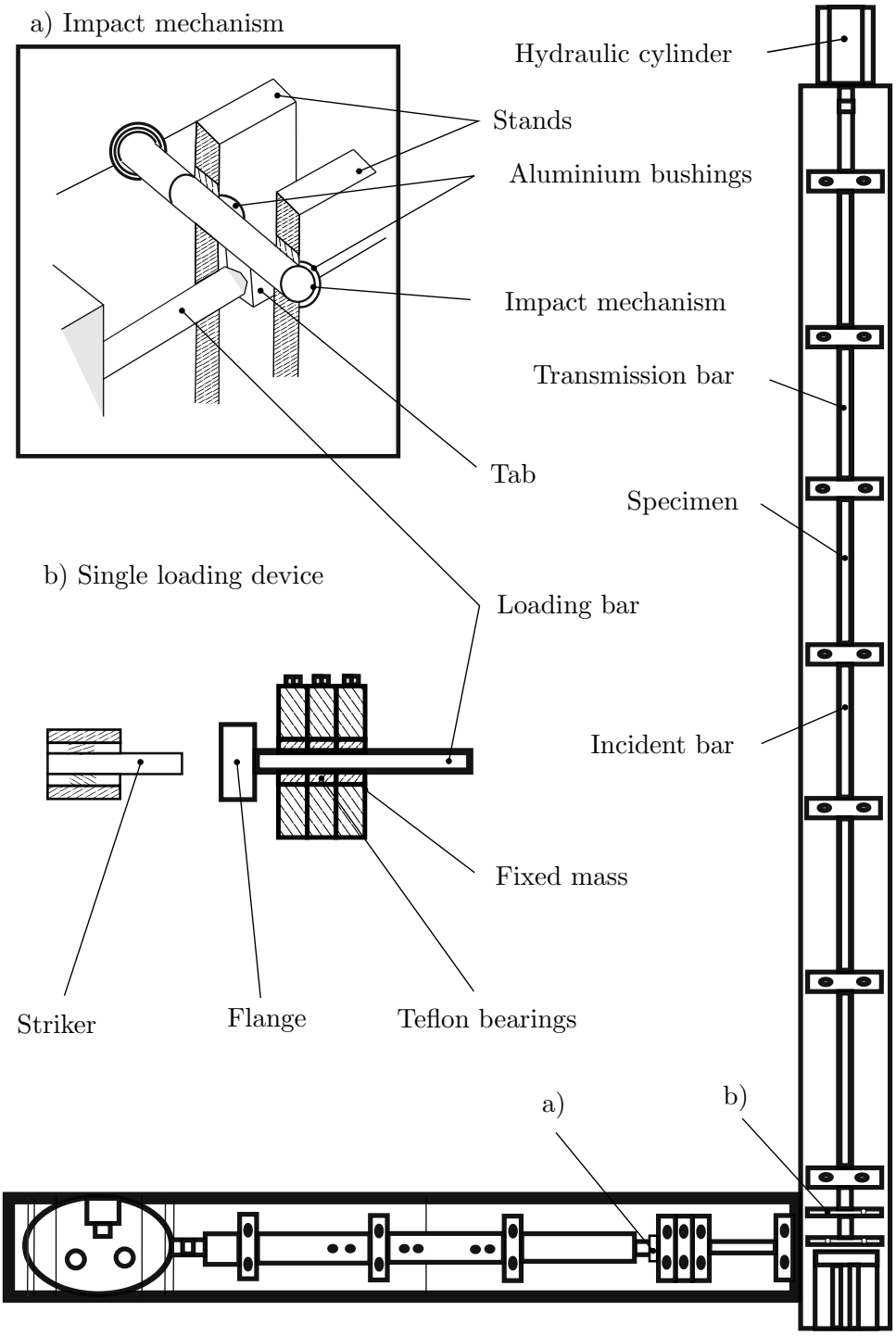

Figure 3.11: Claus et al. direct impact loading TSHB, adapted from [31].

The striker length, velocity, and the pulse shaper geometry were the typical considerations when the desired waveform was generated and could be directly applied to control the torsional wave rise time, amplitude, and duration. Though a major advantage of this technique is the capability to control the loading profile, the fact that a lateral load is exerted on the bar end results in a bending wave inevitably being present in the loading wave. Therefore, the larger the torsional amplitude, the larger the bending wave interference, resulting in a higher difficulty degree in eliminating the bending wave invalidating the pure shear assumption.

3.9.1.4 Electromagnetic loading

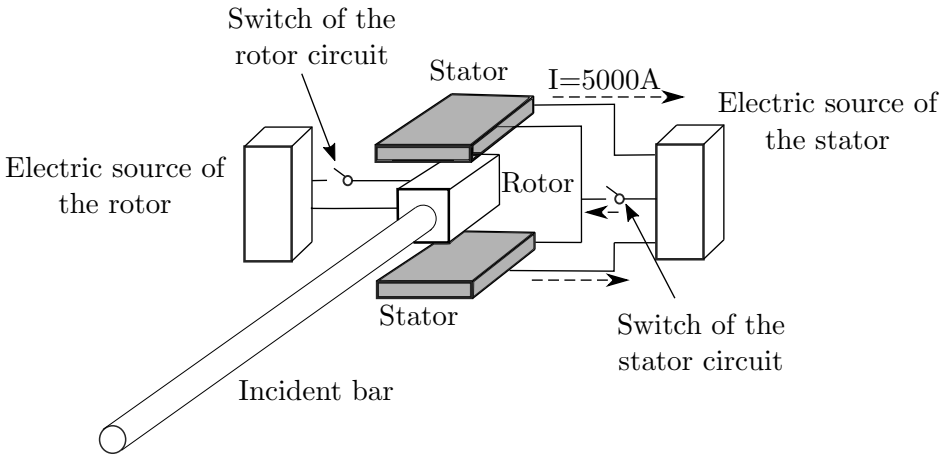

Figure 3.12: Fang et al. electromagnetically loaded TSHB, adapted from [32].

A new approach to creating the torsional loading pulse was attempted by Fang et al. [32] that used a motor as shown in Figure 3.12. The electromagnetic motor contained two electrical circuits, a rotor circuit and a stator circuit. The rotor circuit contained the rotor, the electric source and a switch; while the stator circuit contained the stator, the electric source and a switch. Within the stator circuit magnetic field, which is built by applying a large constant current to the stator circuit, the connection of the rotor circuit generates an instantaneous torque on the rotor. The generated torque is then transmitted into the incident bar as a torsional wave. An annular rubber specimen was used and was bonded to the incident and transmission bars using an instant adhesive.

The rise time was approximately 700 μs which ensured the specimen stress was in an equilibrium state while the strain rate was approximately 8 /s. The magnitude of the generated pulse could be controlled by adjusting the current in both circuits. The loading technique showed good repeatability in the experimental results which verified the reliability of this technique.

3.9.1.5 Flywheel loading

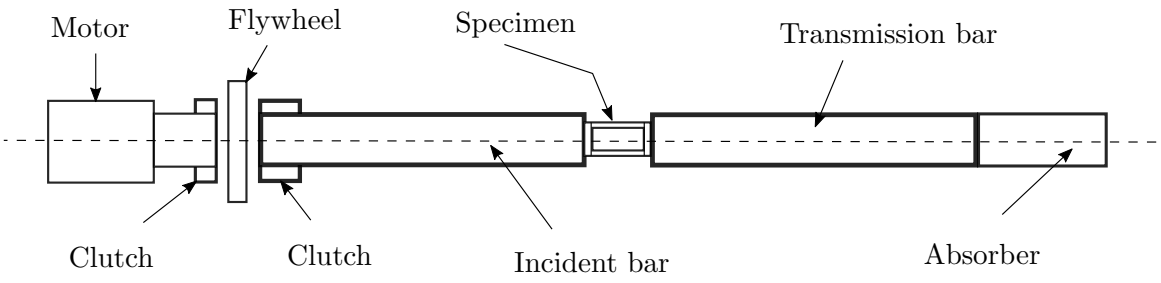

Figure 3.13: Fang et al. flywheel loading TSHB, adapted from [5].

Yu et al. [5] discussed a novel design by Fang et al. who developed a loading technique using a flywheel as the integral load source, shown in Figure 3.13. The loading apparatus consisted of a motor, two electromagnetic clutches and a flywheel. The magnetic force generated by the electromagnetic clutches can position the flywheel between the clutches. The left electromagnetic clutch is turned on which attracts the flywheel. Upon engagement of the flywheel and the

clutch, the motor is turned on which accelerates the flywheel to the required rotational speed. The flywheel is then disengaged from the left clutch and switched over to the right electromagnetic clutch. The torsional wave is generated by the friction between the flywheel and the right clutch. Rise times were approximately 200 ms with durations approximately 600 ms. The very high rise time minimises its capability to test at high strain rates.

3.9.2 TSHB specimens

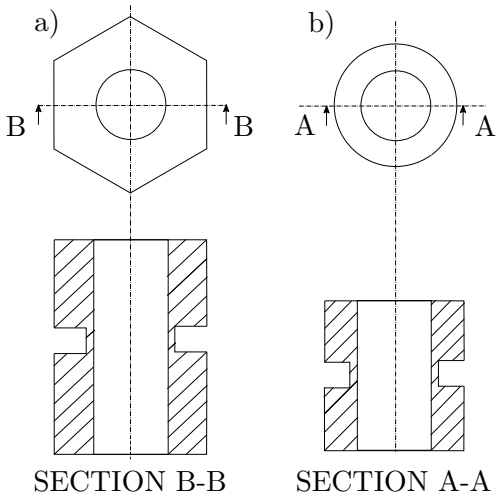

Figure 3.14: TSHB specimens, adapted from [1].

The key components of standard TSHB specimens are summarised in [1]. Standard TSHB specimens, shown in Figure 3.14, are short, thin-walled tubes with integral flanges machined from bar stock and are commonly polycrystalline in nature. There are two methods of holding the specimen in position: via mechanical means and by cementing the specimen flanges with epoxy cement.

Mechanical connections must be as rigid as possible which prevents loss of motion between the bars and the specimens as the torsional wave passes. Based on this requirement, threaded connections are not appropriate. However, hexagonal flanges on the specimen with matching sockets in the end of the bars have been used with success. Small set screws are used to hold the driving faces of the bar's hexagonal sockets against the specimen flanges. For specimens with higher flow stresses, the hexagonal sockets are filled with warm glycol phthalate before the tightening of the set screws to enhance rigidity.

Cemented connections are rigid and only provide enough strength for specimens with low flow stresses. The faces of the flanges are directly chemically bonded (glued) to the bar ends. An adapter is used on specimens with higher flow stresses to increase the surface area of the glue. Cemented connections require long time to cure and cannot be used at higher temperatures. The bar ends also have to be cleaned after each test.

An important value in determining the dimensions of the flanges, as well as the design of the adapter or mechanical connection, is the torsional mechanical impedance. The impedance should closely match that of the bars to ensure that the stress pulses do not undergo reflection. To achieve a nearly homogeneous state of strain, short specimens should be used. Short specimens ensure the desired state of strain is achieved after a few reflections of the loading pulse within the specimen.

Chapter 4

TSHB testing in BISRU and motivation for dissertation

This chapter discusses the existing work in BISRU relating to TSHB systems including the latest load-application mechanism, which is an adaptation from a previous design, as well as the clamping mechanisms. The two clamping mechanisms, designed as part of undergraduate research projects, include the fracture-pin clamping mechanism and the wedge-release clamping mechanism.

The torque generation system and the clamping mechanism are integral to the operation of the TSHB prestored energy method. The torque generation system should ensure a purely torsional load is generated in the system while the clamping mechanism should hold the desired torque without slipping and rapidly release the torque to produce the desired stress pulse. The chapter ends with a critique of the work reviewed in the literature review and builds the motivation for this dissertation.

4.1 Existing work in BISRU

4.1.1 Load-application mechanism

A torque generation system was designed as part of an undergraduate research project [33] and is shown in Figure 4.1. A hydraulic jack is integral to the operation of the system where the extension of the hydraulic jack results in the rotation of the loading arm which imparts a torsional load onto the incident bar. To minimise the effect of the bending moment created due to the mechanics of the loading system, support structures are positioned on either side of the loading arm. Bushings pressed into the support structures minimise the friction and wear during the rotation of the loading arm.

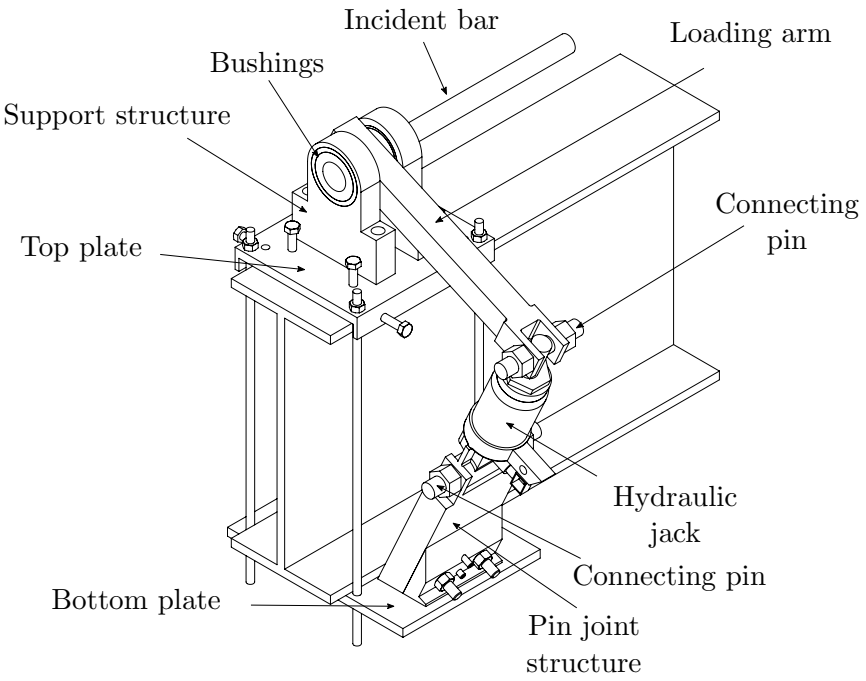

Figure 4.1: Load-application mechanism

4.1.2 Wedge-release clamping mechanism

Figure 4.2 (a) shows an isometric view of a clamping mechanism designed by Nake [34] where a wedge plays an integral role in its operation. Figure 4.2 (b) shows a cross-section of the clamping and release components. Clamping is achieved by the tightening of the clamp pad with the lead screw from the one side and constraining the support using a wedge from the other. The pads have a curvature matching the circumference of the incident bar. Once the desired torque has been stored in the bar, the wedge is struck and drops, releasing the incident bar.

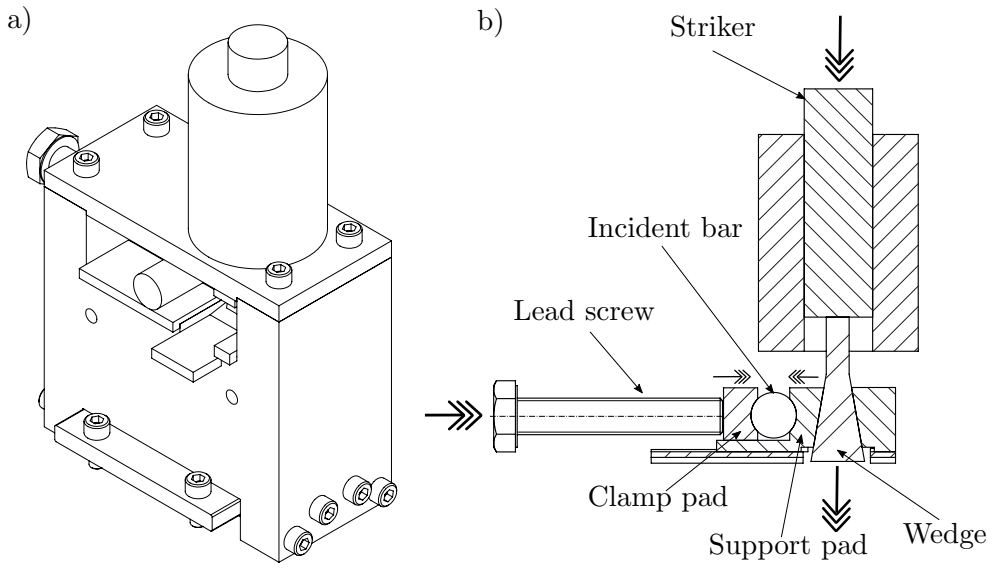

Figure 4.2: Wedge-release clamping mechanism

4.1.3 Fracture-pin clamping mechanism

Figure 4.3 shows a clamping mechanism designed by Purnell [35], which was based on the work of Gilat et al. [36] who developed a clamp to hold and then release a tensile load through the use of a fracture-pin. Clamping is achieved by pushing the lower end vice jaws together with the lead screws. Once the required torque is applied, one lead screw is tightened up to the point where the fracture-pin fractures, releasing the incident bar. The fracture-pin is designed with a notch in the middle to ensure fast uniform fracture. The two vice jaws have a curvature matching the circumference of the incident bar. Prior to every test the surface of the bar and the arms are cleaned with acetone to ensure good grip when clamping.

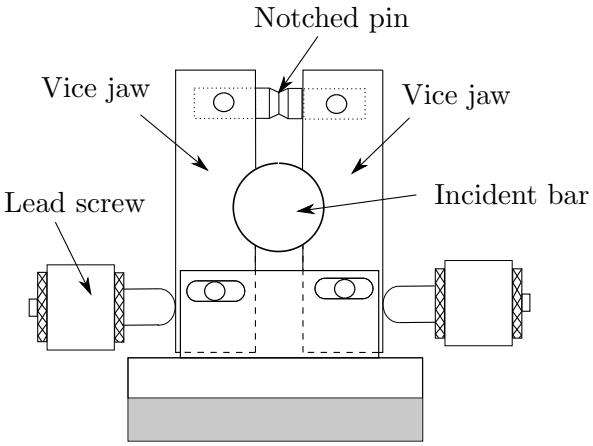

Figure 4.3: Fracture-pin clamping mechanism, adapted from [35].

4.1.4 I-beam

A stable frame to mount all the TSHB system components was required. The frame had to be adjustable to accommodate for the possibility of an uneven floor. A steel I-beam mounted on adjustable support legs was purchased for this purpose with a length of 3.5 m.

4.1.5 Amplifier boxes

The amplifier boxes, an example of which is shown in Figure 4.4, were built to magnify the strain measurements. They are fitted with Texas Instruments INA110 amplifiers which are fast-settling FET-input instrumentation amplifiers. The amplifiers are ideal for high speed data acquisition systems such as TSHB systems.

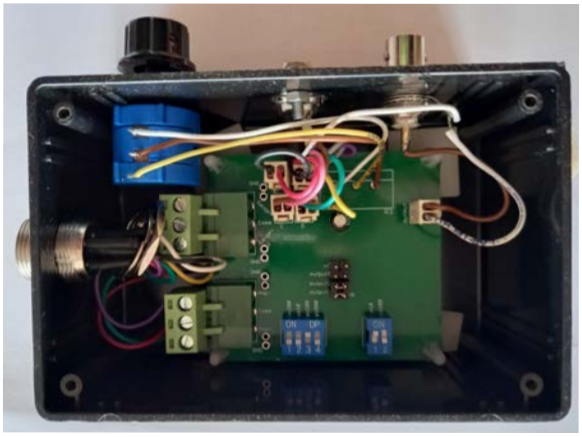

Figure 4.4: Amplifier box

4.2 Critical review

The following findings are made based on the reviewed literature:

- Existing specimen types for the characterisation of sheet metal are prone to crack initiation at the free edges. This fracture occurrence is attributed to inhomogeneous stress distribution and therefore results in the failure to achieve shear under the desired conditions.
- Quasi-static systems commonly have the following fundamental characteristics. The specimen is often fixed at one end with the loading system connected to the other. The system must have a stiff loading system and reaction frame and may incorporate an integral shaft. Maintenance of alignment and coaxiality is crucial to the system operating successfully.
- Review of the existing TSHB systems showed that they can be divided into five categories. The prestored energy method is the most commonly used with a good loading profile. The same components can be reused for every experiment, apart from the fracture-pins when that type of clamping mechanism is used. The loading mechanism highly influences the ability to generate a purely torsional wave. Explosive loading produces the fastest rise times but introduces high-amplitude frequencies in the loading profile and has very short test durations. Other disadvantages include complications due to explosive detonation and the necessity for new explosives for every experiment. Impact loading produces acceptable rise times and allows for the capability to control the loading profile. However, the bending wave introduced to the system upon impact eliminates the assumption of pure shear.
- Two newer methods of loading are the electromagnetic clutch and flywheel. While not many researchers have explored these techniques, early indications are that electromagnetic loading allows for good repeatability from test to test as well as an ability to control the loading profile via adjusting of the system's current. The slow rise times of both systems make them incapable of testing at high strain rates.
- The assumption of one-dimensional stress wave propagation as well as stress equilibrium of the specimen is crucial to the operation of TSHB.

.

4.3 Project aim

Based on the existing work regarding shear testing techniques that was reviewed, a new specimen, and associated apparatus, for the quasi-static and dynamic torsional and shear testing of sheet metals is introduced. While existing TSHB tubular specimens allow for uniform shear, they do not work for characterising sheet metal. A new experimental specimen therefore was designed with the following features:

- the specimen will have a continuous shear region.
- the specimen will be used for characterisation of sheet metal.
- the specimen will have a convenient surface for Digital Image Correlation (DIC).

DIC is a non-contact optical strain field measurement technique. The technique allows for the measurement of full-field displacements and strains directly on the surface of a specimen [37]. The general strain state of a specimen can be evaluated by averaging the data within a box while the strain history of localization points and failure locations can be tracked by point data [37]. The implementation of DIC is beyond the scope of this project, but future usage was incorporated in the design decisions.

There are no free edges where crack initiation can initiate in the continuous gauge section of the annular in-plane torsional specimen. For isotropic materials, the resulting stress state only varies radially, allowing for large strains to be achieved. Since no experimental testing apparatus exists for the new specimen in BISRU, two new testing systems were designed. The main goal was to develop systems that can be used to test a wide variety of materials under different strain rates. The first system, developed for quasi-static testing, was integrated on a Zwick universal testing machine, and focused on characterising materials at low strain rates. The second system, developed for dynamic testing, focused on modifying and improving the TSHB apparatus for the characterisation of materials at high strain rates.

The quasi-static system was designed with a stiff loading system and an integral shaft. Maintenance of alignment and coaxiality was achieved by incorporating fine tolerance bushings into the housing. One end of the specimen was fixed with the other connected to the loading system. The TSHB system design adopted the prestored energy method since considerable work has been done on this system in BISRU. A nested configuration was adopted to allow for a longer incident bar and thus large obtainable strains. The configuration also allowed the flat face of the annular in-plane torsional specimen to be outward facing, thereby allowing for the potential for DIC to be adopted.

The design scope was constrained by selecting a specific material to characterise and defining the total strain and range of strain rates to be tested. The goal was to produce a specimen that undergoes pure shear in the gauge section of the specimen. A rate dependant equation suitable for a constitutive equation was developed and then calibrated to match the material properties obtained. The following chapters document the design of the annular in-plane torsional specimen, quasi-static torsional system, and the torsional split Hopkinson bar system.

Chapter 5

Specimen design

This chapter covers the design of the annular in-plane torsional specimen including details regarding its specific geometry and manufacture. Specimen measurement techniques and methods for mounting and dismounting of the specimen are also discussed.

5.1 Requirements

The specimen has the following requirements:

- Specimens should achieve axially symmetric shear conditions.
- Specimens should be able to generate a homogeneous stress and strain field in a predefined gauge section, when subjected to an appropriate load.
- Specimens should have a continuous gauge section.
- Specimen failure should occur within the desired gauge section.
- Specimens should be fabricatable from sheet materials.
- Specimens should have a flat and accesible surface on which DIC could be used to measure strain.
- Specimens should be common to both quasi-static and dynamic testing devices.
- Specimens should be suitable for testing on a modified torsional split Hopkinson bar system configuration with an incident bar nested inside a transmission tube.

5.2 Geometry nomenclature

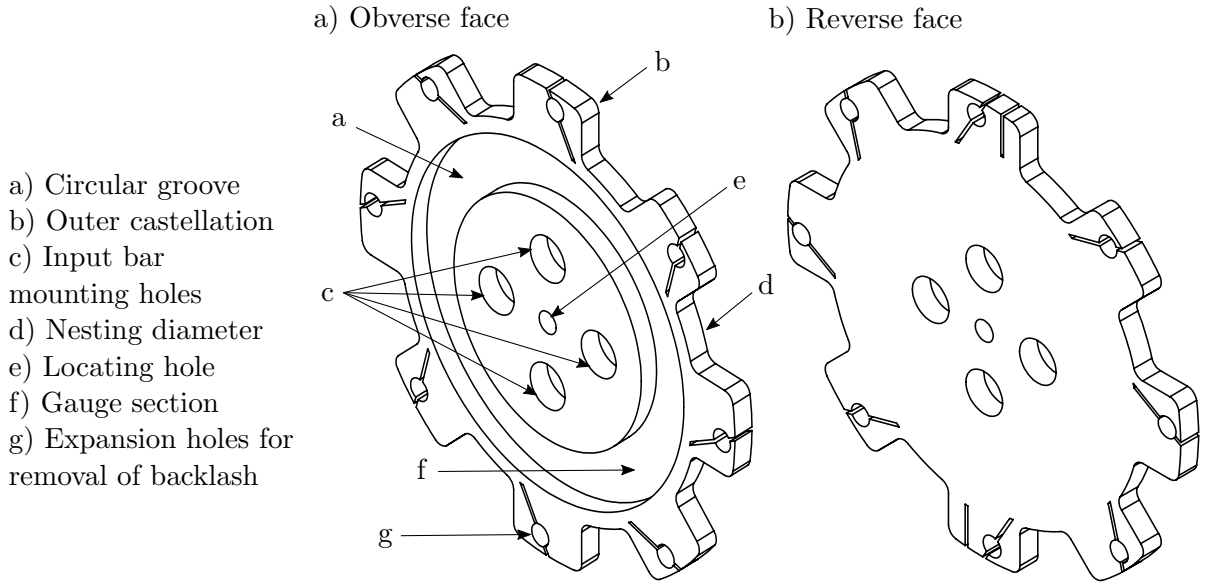

Figure 5.1: Annular in-plane torsional specimen features.

Figure 5.1 shows a specimen with a rectangular profiled circular groove on one face of the specimen. The continuous circular groove removes the possibility of edge effects. Machining the groove from one face removes any impurities that might exist at the mid-thickness of the sheet material. By reducing the thickness of the gauge section of the specimen, the strength and stiffness is reduced within this region which causes failure to occur within the gauge section. By ensuring deformation primarily occurs in the gauge section, undesirable effects in other regions of the specimen are minimal, thereby not disturbing the ideal shear conditions. The reverse face of the specimen provides a flat surface on which DIC could be used to measure strain in the future.

The nesting diameter of the specimen is limited by the dimensions of the transmission tube used in the TSHB experiments (discussed in Chapter 7) and was chosen to be a sliding fit into the inner diameter of the transmission tube. The outer castellations on the specimen are designed to be press-fitted into matching castellations that are machined on the transmission tube. The holes in the castellations are used to ensure good mechanical connection via self-tapping screws. The slits are designed into the castellations to allow the screw holes to hinge about the edge of the slit. Four holes in the centre portion of the specimen allow pins located on the input bar to be press-fitted on and function as the mounting mechanism of the specimen to the input bar during mounting. The hole located at the very centre of the specimen ensures concentric positioning of the specimen on the input bar. The specimens have gauge section thicknesses ranging from 0.2 mm to 0.4 mm and gauge section widths ranging from 0.5 mm to 5 mm. The low overall thickness of the specimen makes it possible for the specimen to be manufactured from sheet metal.

5.3 Calculations and analysis

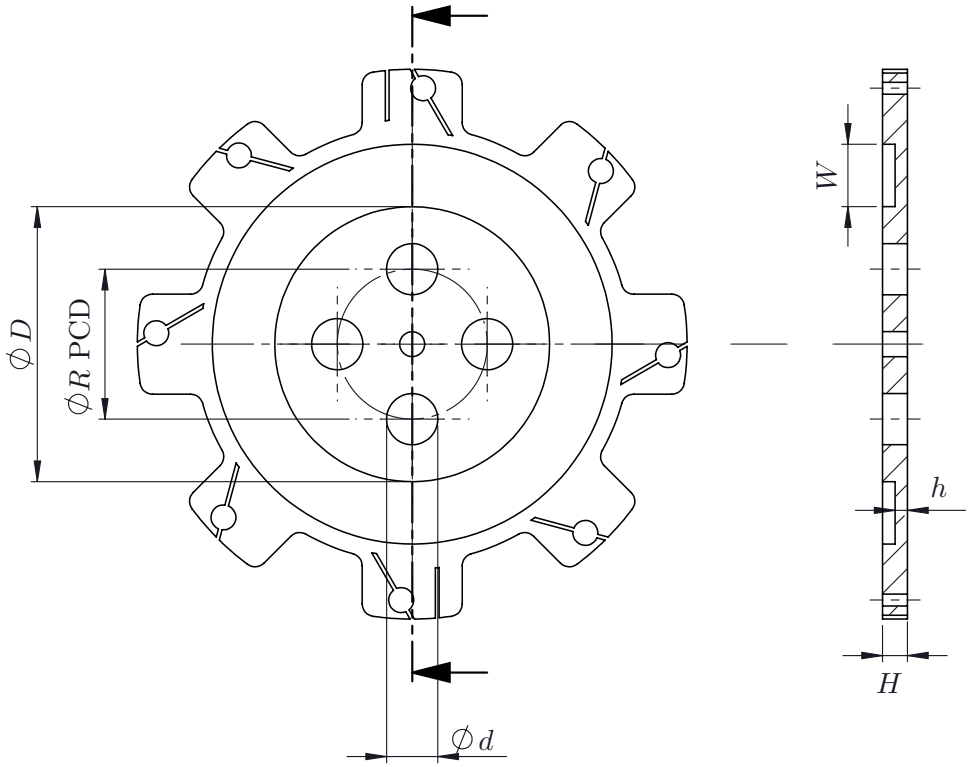

Figure 5.2: Specimen dimension variables.

Figure 5.2 shows the important specimen dimension variables where the region with the thinnest cross-section is referred to as the gauge section. d is the diameter of the pin holes in the centre section; R is the pitch circle diameter (PCD) of the pin holes; and N is the number of pin holes to be used for mounting. H is the overall thickness of the specimen; h is the thickness of the gauge section; and W is the width of the gauge section. D is the inner-most diameter of the gauge section and is where yielding of the gauge section will commence.

It is important to ensure that the gauge section shears before the pin holes at the centre of the specimen experience any plasticity. The pin hole stresses must not come close to or exceed the stress experienced in the gauge section to minimise plastic deformation at the pin hole regions.

The fundamental relationship between torque and stress is

$$T = Fr = \sigma A r \tag{5.1}$$

where F is the force, r is the moment arm, σ is the stress and A is the area.

Condition 1: The load required for plastic deformation in the gauge section is

$$T = \frac{\tau_y \pi D^2 h}{2} \tag{5.2}$$

where T is the torque, τ_y is the shear yield stress, the projected area of the inner circle is $\pi D h$ and the moment arm is $\frac{D}{2}$.

Condition 2: The load required before the pin holes become plastic is

$$T = \frac{\sigma_y dHRN}{2} \tag{5.3}$$

where T is the torque and the projected area of the pin is dH.

The aim is to ensure that state 1 occurs before state 2, therefore

$$\tau_y \pi D^2 h < \sigma_y dHRN \quad . \tag{5.4}$$

Re-arranging equation (5.4) results in the criterion

$$\frac{h}{H} < \frac{\sigma_y dRN}{\tau_y \pi D^2} \quad . \tag{5.5}$$

It is also important to ensure that the pins do not fail when the specimen is loaded. The correct geometry and number of pins therefore had to be selected. The important variables include the pin diameter, d, pin spacing, S_p, effective force per pin, F_p and edge spacing (distance from pin to the edge of the input bar), S_e. The specimen has the following selection limits:

- the spacing between pins must be greater than 5 mm.
- the effective force per pin must be below the double shear strength of the pin after a safety factor of 2 is applied.
- the edge spacing between the edge of the pin and the edge of the input bar must be 2 mm.

The equations used for the calculation of these variables are attached in Appendix A.

Nominal pin diameter (mm)	Double shear strength (kN)	Double shear strength (kN) applying safety factor of 2
1.0	1.5	0.75
1.5	3.4	1.70
2.0	5.5	2.75
2.5	8.0	4.00
3.0	13.0	6.50
4.0	22.0	11.00

Table 5.1: Double-shear strength for DN 6325 dowel pins [38].

Table 5.1 shows the double shear strength for selected pin diameters that are used as a limiting factor for pin selection with a safety factor of 2 applied to reduce the risk of failure. In general, a safety factor of 2 was preferred since reliable materials were used and loading and environmental conditions were not severe [39].

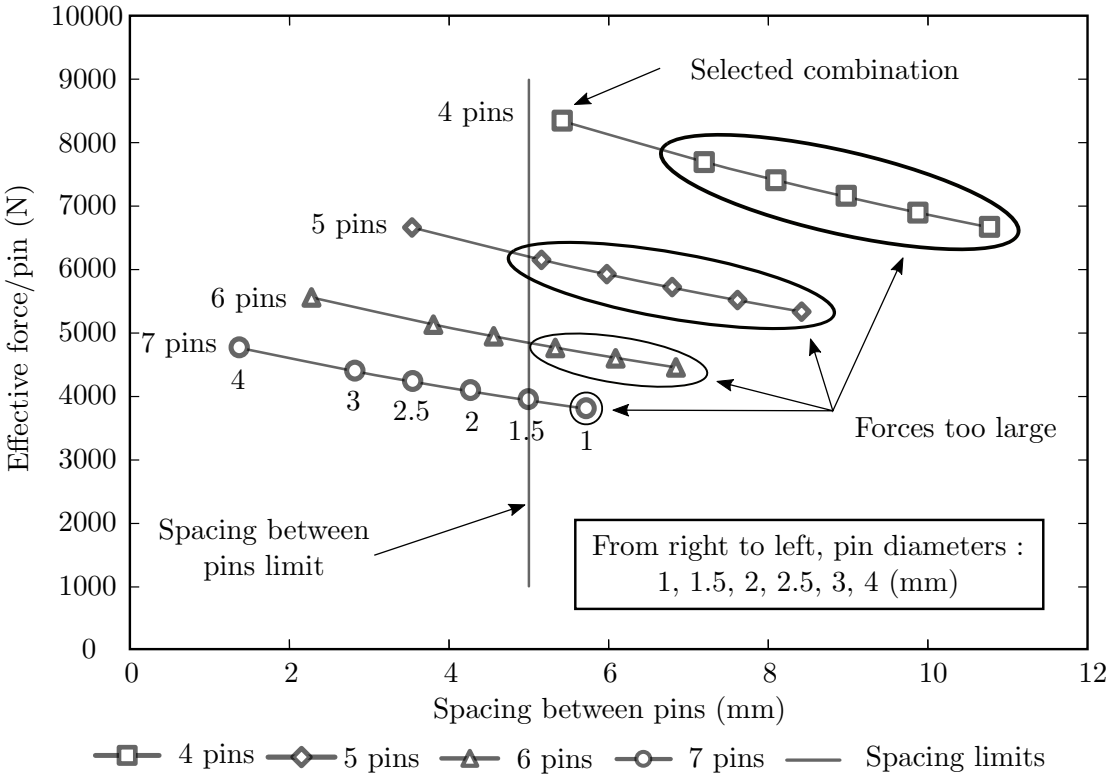

Figure 5.3: Specimen pin hole geometry selection.

Figure 5.3 shows the results of the comparison between pin variables and pin diameters for an edge spacing of 2 mm. Only four or more pins are considered, as fewer pins result in extremely large forces. The number of pins variable runs from the four pins curve at the higher force region to the seven pins curve at the lower force region. This agrees with the design equations that suggest the effective force per pin decreases with an increase in the number of pins. The pin diameter variable runs from right to left on each curve with diameters increasing from 1 mm to 4 mm. The figure shows that most combinations fall outside the acceptable range either due to the effective force per pin being higher than the double shear strength of the pin or because the spacing between the pins falls below the design limit. Only one combination is acceptable and is therefore selected for the specimen design. The selected combination is:

- Four pins of diameter 4 mm.
- 2 mm edge spacing.
- Inner-most diameter of 22 mm to allow for a 1 mm shoulder outside of the gauge section of the specimen to assist when removing the specimen from the 20 mm input bar.

The selected values are then substituted back into equation (5.5) and, assuming a von Mises criterion relationship between the normal stress and shear stress,

$$\frac{h}{H} < 0.21 \quad . \tag{5.6}$$

A sheet metal with sheet thickness 2 mm is selected to allow for a gauge section thickness range of 0.2 mm - 0.4 mm.

Figure 5.4 shows the specimen castellation dimension variables while Figure 5.5 shows the outer tube dimension variables. b is the width of the castellation; D_s is the inner-most diameter of the castellation; b_t is the width of the opening in the castellation machined in the tube and w is the wall thickness of the outer tube. The other key variables are the number of castellations machined on the specimen, N_s, and the number of openings in the castellations machined in the tube, N_t. An investigation was done to determine the geometry of the specimen castellation based on the forces that the castellation experiences.

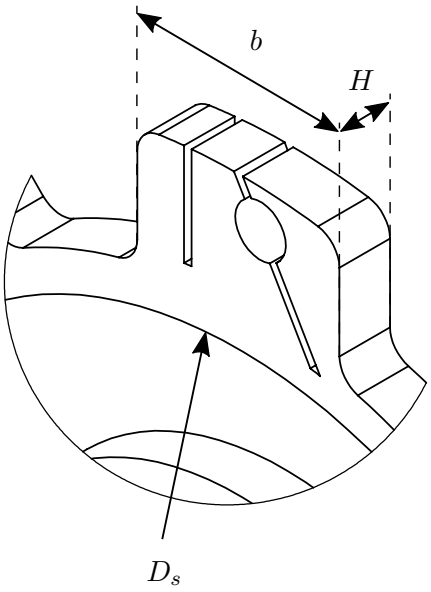

Figure 5.4: Specimen castellation dimension variables.

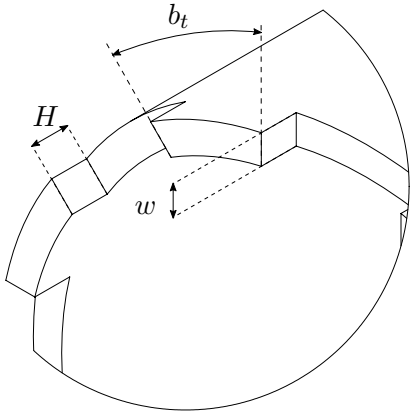

Figure 5.5: Outer tube dimension variables.

The two forces on the specimen castellations are the normal force acting on the face and the shearing force. They are defined as follows:

$$\text{Normal stress} = \sigma_y = \frac{F}{A} = \frac{2T}{D_s w H N_s} \rightarrow T = \frac{\sigma_y D_s w H N_s}{2} \tag{5.7}$$

$$\text{Shearing stress} = \tau_y = \frac{F}{A} = \frac{2T}{D_s b H N_s} \rightarrow T = \frac{\tau_y D_s b H N_s}{2} \tag{5.8}$$

Another important requirement is to ensure that the gauge section shears before either the crushing or the shearing of the castellation occurs. Thus

$$\tau_y \pi D^2 h < \tau_y D_s b H N_s \rightarrow \frac{\pi D^2 h}{D_s H} < b N_s \rightarrow \boxed{8.94\ mm < b N_s} \tag{5.9}$$

$$\tau_y \pi D^2 h < \sigma_y D_s w H N_s \rightarrow \frac{\tau_y \pi D^2 h}{\sigma_y w D_s H} < N_s \rightarrow \boxed{3.19 < N_s} \tag{5.10}$$

For the limiting case where the outer tube is made from the same material as the specimen, the following parameters are required for the outer tube:

$$\boxed{8.94\ mm < b_t.N_t} \tag{5.11}$$

$$\boxed{3.19 < N_t} \tag{5.12}$$

By using the conditions in equations (5.9) - (5.12) together with a safety factor of 1.8, the following two criteria need to be met when choosing the specimen castellation width and outer

tube castellation opening width. In this case, a safety factor of 1.8 is adopted since the selection criteria is limited when a safety factor of 2 is used.

$$b > 5mm \tag{5.13}$$

$$b_t > 5mm \tag{5.14}$$

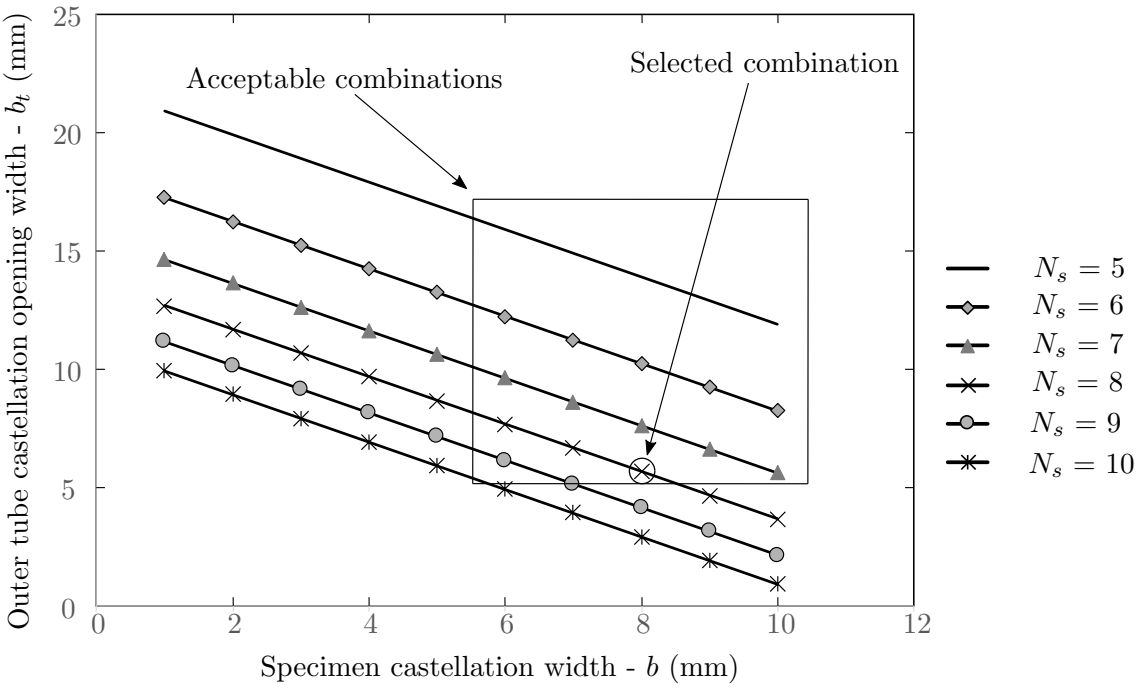

Figure 5.6: Specimen castellation dimension design selection.

Figure 5.6 shows the specimen castellation width against outer tube castellation opening width based on the number of castellations. The figure suggests a number of acceptable combinations. The combination chosen is eight castellations with a specimen castellation width of 8 mm which results in an outer tube castellation opening width of approximately 5.8 mm. This is selected due to the fact that the outer tube is made from a material twice as strong as the specimen. The selection of outer tube material allows for the specimen to deform plastically while the bars remain in the elastic state. A further factor was the desire for the number of castellations to be an even number.

The shear stress, τ, is calculated by

$$\tau = \frac{T}{\pi {r_i}^2 h} \tag{6.15}$$

where T is the torque, h is the local thickness of the gauge section (during deformation and at point of facture), and $r_i = D/2$ is the inner-most radius. The strain is calculated by

$$\gamma = \tan\phi = \frac{r_i \theta}{W} \tag{6.16}$$

where θ is the angle of twist, W is the width of the gauge section, and r_i is the inner-most radius.

5.4 Material and manufacturing process

The material used for the experimental tests was Aluminium 1050 H14. Aluminium 1050, according to Aalco [40], is a popular grade of aluminium for sheet metal. It is often used where moderate strength is required and has high ductility, excellent corrosion resistance as well as a highly reflective finish. Common applications include chemical process plant equipment, food industry containers, and as lamp reflectors, among others. Temper type H14 indicates a sheet that has been work hardened by rolling to half hard (hardened but still very ductile) without annealing after rolling. The rolling process and crystallographic structure of the sheet material results in significant anisotropic behaviour.

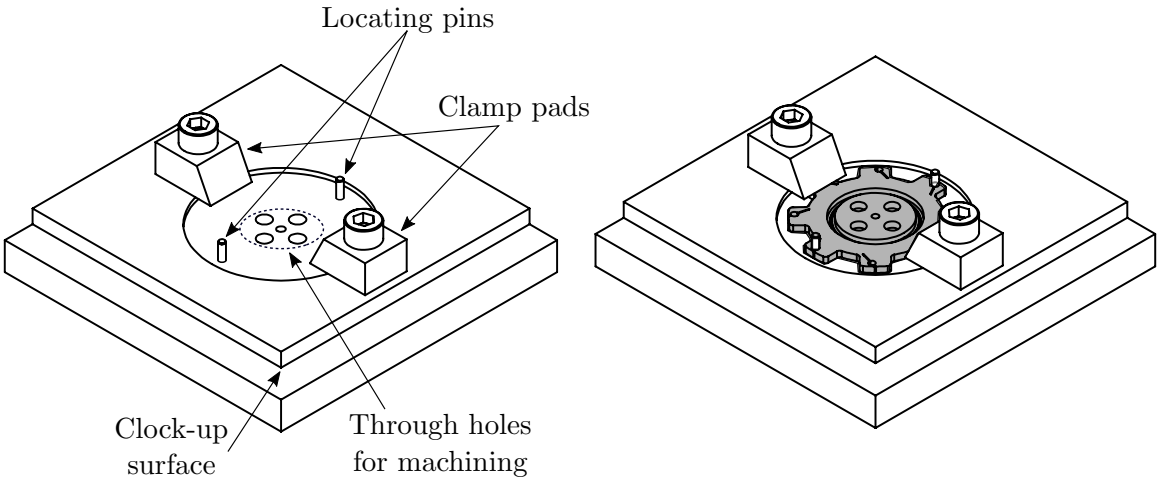

Figure 5.7: Machining fixture

A half sheet of aluminium sheet metal 1050 H14 (1250 mm x 1250 mm) was purchased and cut into 60 mm x 60 mm squares. The castellations, backlash removal slot and the 2 mm holes (for the self-tapping screws) were then machined using wire electrical discharge machining (WEDM). A special fixture, shown in Figure 5.7, was machined to house the WEDM machined specimen to assist in the milling operation. The specimen was clamped in the fixture; after which the gauge section, central alignment hole, and mounting holes were machined. Lastly, the mounting holes were reamed for a good fit.

The specimen geometry only varies by the thickness and width of the gauge section and thus the method of machining is the same for all specimen geometries. Two lines, perpendicular to each other, were scribed on the reverse face through the centre of the specimen. The displacement of these lines allow for the direct observation of the angle of twist of the specimen. Specialised milling tools were ordered to achieve the desired gauge section thicknesses and widths.

5.5 Specimen measurement

After machining, the actual dimensions of each specimen were measured. A Vernier calliper suffices for all measurements, except for the measurement of the gauge section dimensions. Therefore, a technique to measure the two critical dimensions was developed. Two methods are used, the first involving a custom-designed cone tool used together with a tube micrometer and the second involving miniature bearing balls together with a tube micrometer.

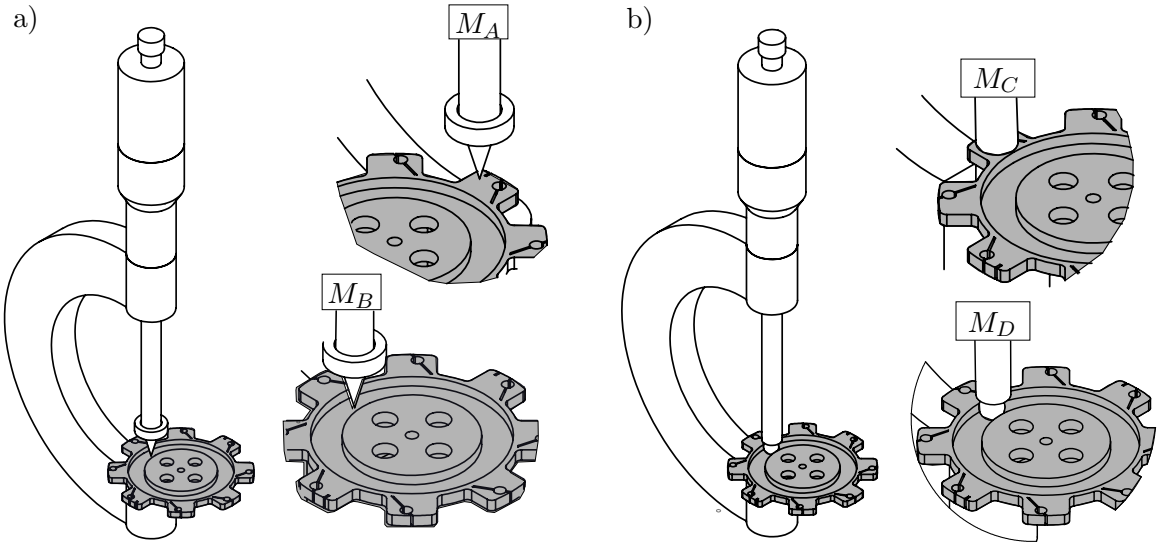

Figure 5.8: Measuring technique: (a) Cone tool, and (b) Bearing ball.

Figure 5.8 (a) shows the cone tool measuring technique. The specimen is placed on a metrology table after which a measurement of the overall thickness of the specimen, M_A, is taken. The cone tool is then placed into the groove of the gauge section ensuring that the tip is against the bottom edge of the groove, after which a thickness measurement is taken, M_B. These two measurements are used to infer the gauge section thickness. A second cone-like tool is used to measure the gauge section width. The tool is once again used in conjunction with a tube micrometer and measurements are taken that are used to infer the gauge section width.

The second method, shown in Figure 5.8 (b) made use of miniature bearing balls ranging from 0.5 mm to 6 mm in diameter. Each bearing ball's dimensions are verified prior to it being used. A measurement is first taken of the overall thickness of the specimen, M_C, by using the tube micrometer after which the bearing ball is placed into the groove and a second measurement is taken, M_D. These two measurements are used to infer the gauge section thickness while the gauge section width is measured using the same bearing balls and a similar process. For the case where the width is extremely small, a double groove is machined to allow the micrometer head to contact the smaller bearing balls. The calculation of the specimen gauge section width is attached in Appendix B.

5.6 Specimen mounting and dismounting

Care must be taken when mounting and dismounting the specimen to ensure no damage is done to the specimen, specifically no bending of the specimen or added deformation of the gauge section. Specialised tools were designed for the mounting and unmounting procedures.

5.6.1 Specimen mounting onto input bar

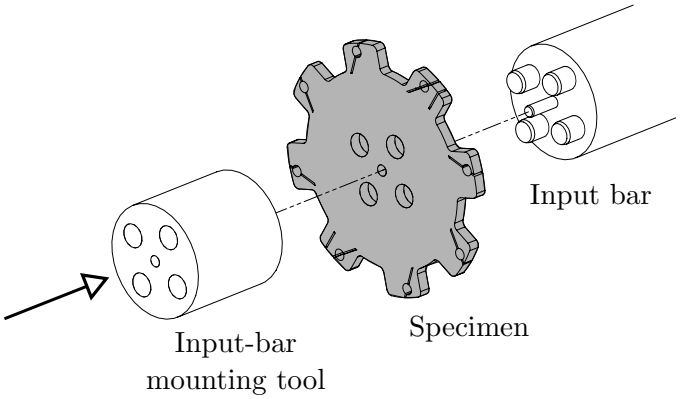

Figure 5.9: Specimen to input-bar mounting technique.

The tool shown in Figure 5.9 is used to assist in mounting the specimen onto the input bar. The five holes in the specimen are first aligned with the five pins on the input bar. The tool is then placed against the reverse face of the specimen and then lightly struck with a soft-blow hammer, resulting in press fitting the specimen onto the input bar.

5.6.2 Specimen mounting onto output tube

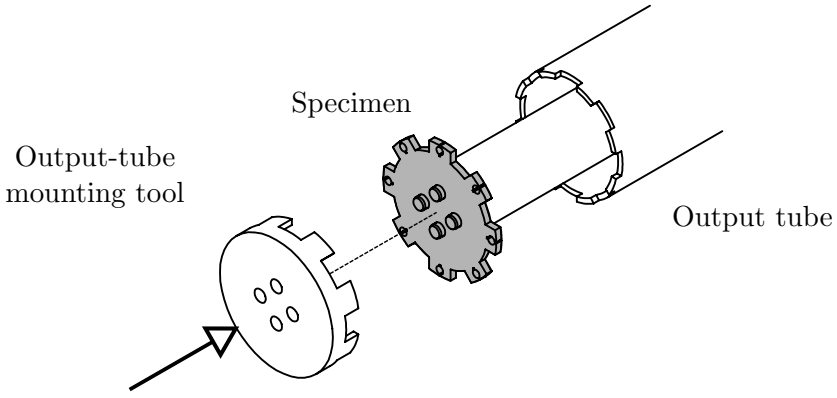

Figure 5.10: Specimen to output-tube mounting technique.

The tool shown in Figure 5.10 is used to assist in mounting the specimen onto the output tube. The input bar is rotated (with the specimen mounted on it) until the castellations of the specimen align with the openings in the castellations of the output tube. The tool is then placed against the reverse face of the specimen and then lightly struck with a soft-blow hammer, resulting in a press fitting of the specimen onto the output tube. Eight self-tapping screws are then used to force the castellation faces of the specimen against the castellation faces of the output tube to prevent relative motion between the two faces.

5.6.3 Specimen dismounting from output tube

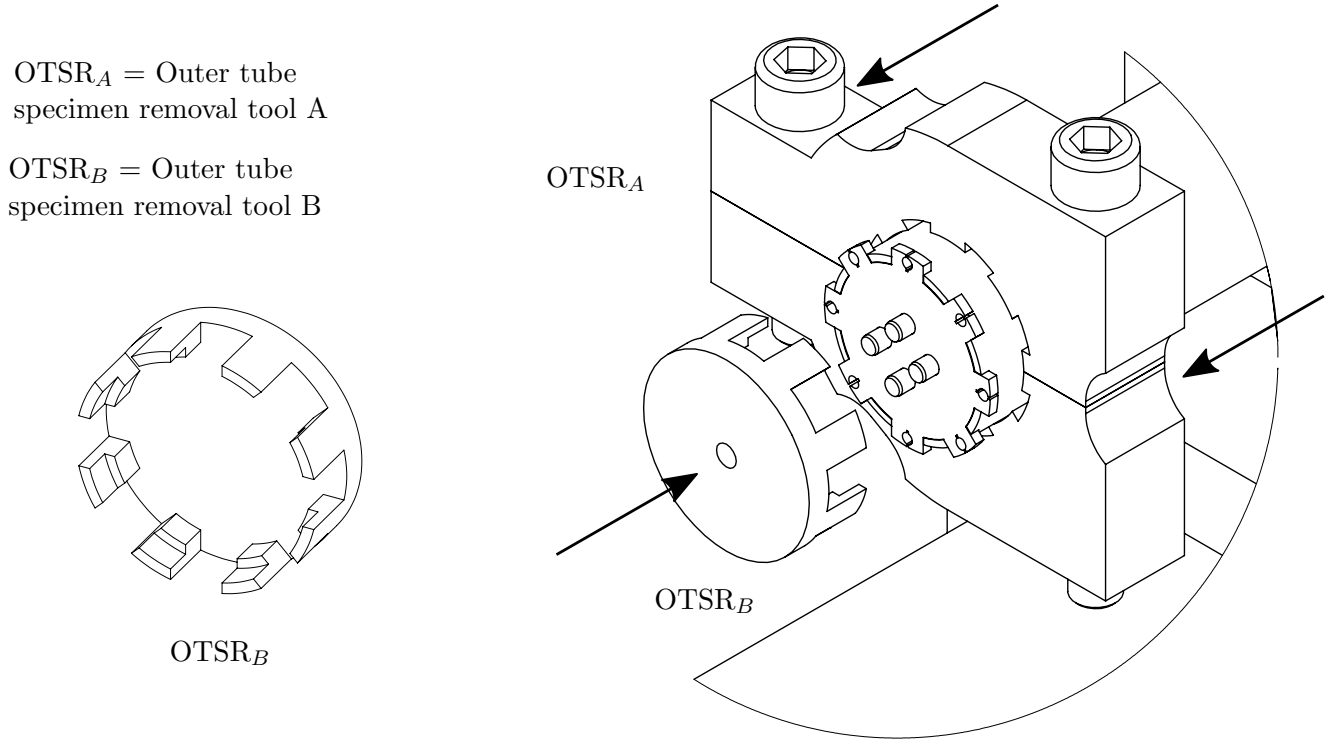

Figure 5.11: Specimen dismounting operation from output tube.

A bearing puller is used together with the tools shown in Figure 5.11 to dismount the specimen from the output tube. Outer tube specimen removal tool A is assembled on the output tube and placed against the obverse face of the specimen. Its castellations match those of the specimen. Tool OTSR$_B$ is then placed against the castellations of the outer tube after which the screw of the bearing puller is screwed against tool OTSR$_B$. The arms of the bearing puller are wrapped around tool OTSR$_A$ after which the screw of the bearing puller is turned. This results in the output tube and the specimen moving in opposite directions, thus dislodging the specimen from the output tube.

5.6.4 Specimen dismounting from input bar

IBSR$_A$ = Input bar specimen removal tool A
IBSR$_B$ = Input bar specimen removal tool B
IBSR$_C$ = Input bar specimen removal tool C

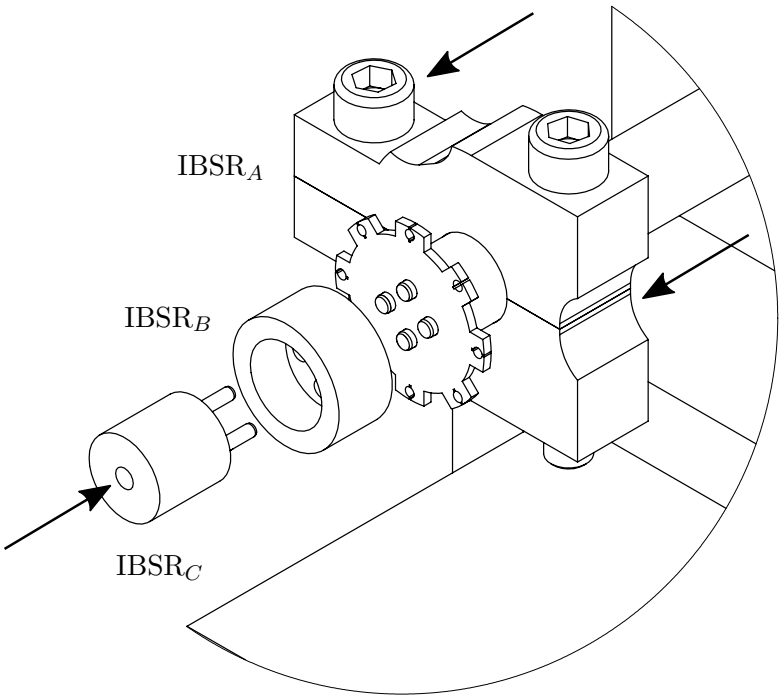

Figure 5.12: Specimen dismounting operation from input bar.

The bearing puller is also used to assist in dismounting the specimen from the input bar. Much in the same way, input bar specimen removal tool A in Figure 5.12 is assembled behind the obverse face of the specimen on input bar. Tools IBSR$_B$ and IBSR$_C$ are then pressed against the four pins on the input bar after which the bearing puller's screw is turned against tool IBSR$_C$. The arms are wrapped around tool IBSR$_A$ after which the screw of the bearing puller is turned. This results in the input bar and the specimen moving in opposite directions, thus dislodging the specimen from the input bar. An image of a fully-mounted annular in-plane torsional specimen is shown in Figure 5.13.

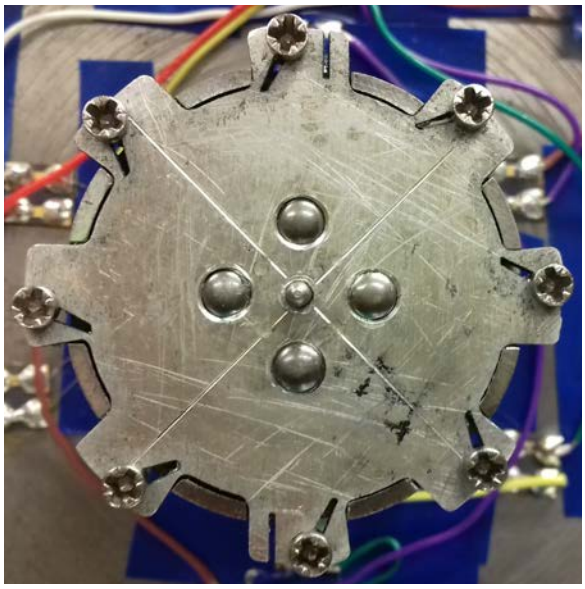

Figure 5.13: An image of a fully-mounted annular in-plane torsional specimen.

Chapter 6

Quasi-static torsional system design

A quasi-static torsional (QST) system, photographs of which are shown at the end of the chapter, was designed and manufactured for the purpose of characterising materials in torsion at low strain rates. The system described in this chapter was specifically built to characterise materials with low flow stresses in specimens manufactured from sheet metal. The QST system apparatus is assembled on a Zwick 1484 universal testing machine (from hereon referred to as Zwick machine). Data from both the Zwick machine and strain gauges on the QST system, is gathered for every experiment.

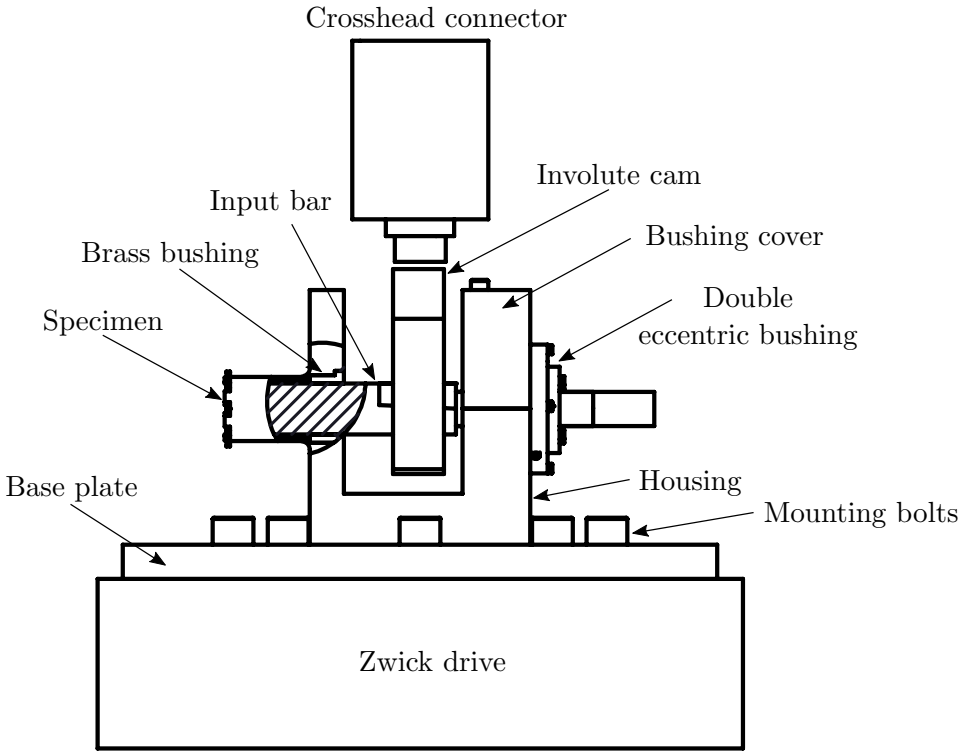

Figure 6.1: Quasi-static torsional system apparatus.

The components of the system, shown in Figure 6.1, consist of an involute cam, input bar, base plate, crosshead connector, brass bushing, housing, bushing cover, double eccentric bushing and specimen and are described in detail in Section 6.1. The instrumentation of the system which consists of the standard Zwick machine data acquisition and strain gauges, all incorporated and captured by the HBM QuantumX MX840B DAQ system, is described in detail in Section 6.2.

6.1 Mechanical components

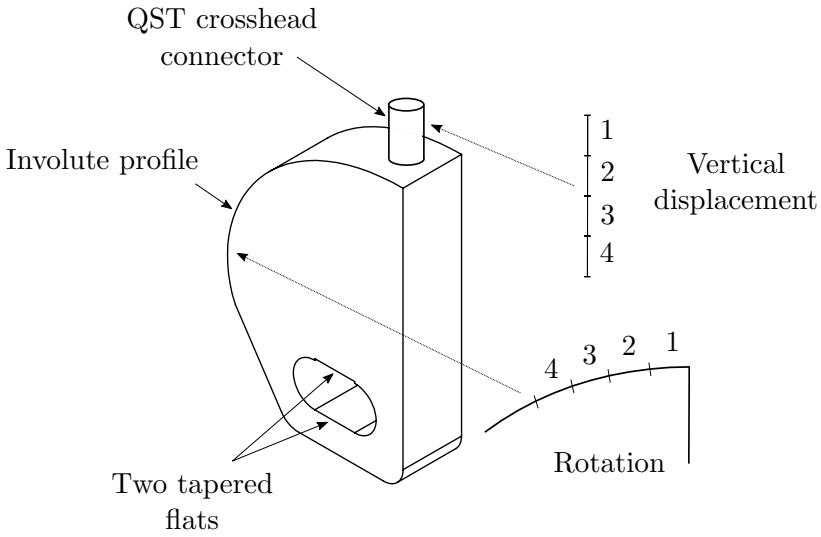

Figure 6.2: QST system involute cam

Involute cam: An involute cam is used to link the vertical displacement of the Zwick machine crosshead to the rotation of the input bar. The involute cam, shown in Figure 6.2, is designed to be rigid and stiff with low inertia. The involute profile chosen allows for a linear relationship between the vertical displacement of the Zwick machine crosshead and the rotation of the input bar. The involute cam is rigidly connected to the input bar by means of two tapered flats machined into the input bar to allow it to be press fitted against the mating flats of the involute cam. This connection is simple and precisely locates the component both concentrically and axially.

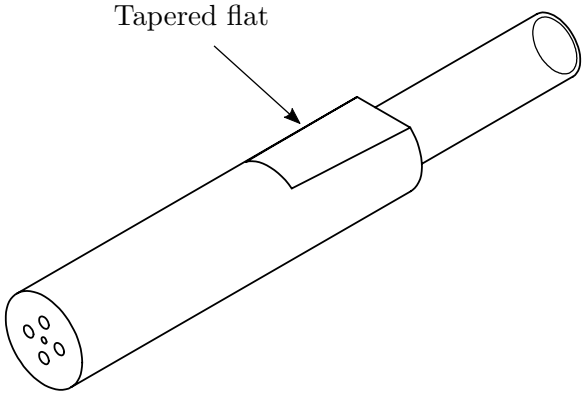

Figure 6.3: QST system Input bar

Input bar: The input bar connects the involute cam to the specimen. This is done with four equi-spaced 4 mm pins, located at a fixed diameter on the face of the input bar. A 2 mm pin is pressed into the centre hole to assist in locating the specimen when mounting. Two tapered flats on the input bar facilitate the connection to the involute cam. The input bar is required to be as rigid and stiff as possible so as to minimize deflection along its length.

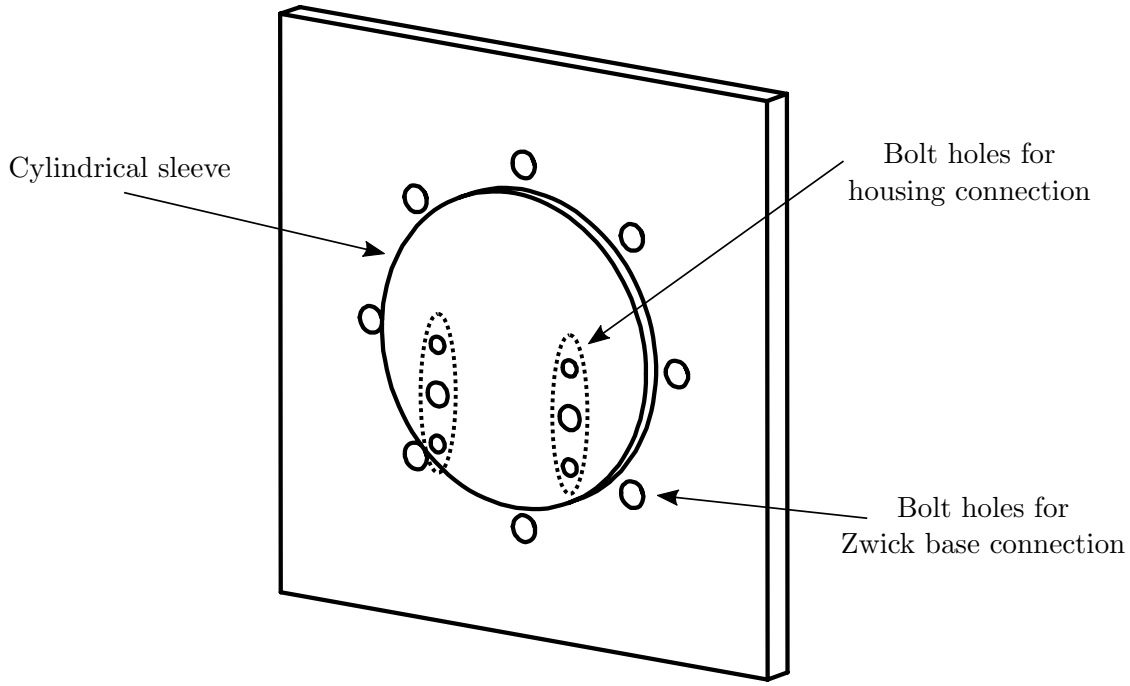

Figure 6.4: QST Base plate

Base plate: A base plate to mount the QST system onto the Zwick machine is required. The base plate, shown in Figure 6.4, is mounted such that when the QST system is connected to the base plate, the involute cam's mid-section is directly in line with the centre mark of the crosshead connector (shown in Figure 6.5).

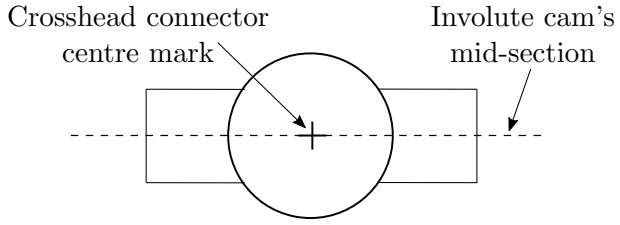

Figure 6.5: Top view of crosshead connector and involute cam alignment.

This is achieved by designing the base plate to include a cylindrical sleeve that slides into the bore hole located in the drive of the Zwick machine. To connect the base plate to the drive of the Zwick machine, eight holes are machined into the base plate to allow eight M16 bolts to be used to connect the two components. The diameter of the cylindrical sleeve is defined by the diameter of the bore hole in the drive of the Zwick machine. The bolt holes located on the cylindrical sleeve are used to connect the rest of the QST system to the base plate.

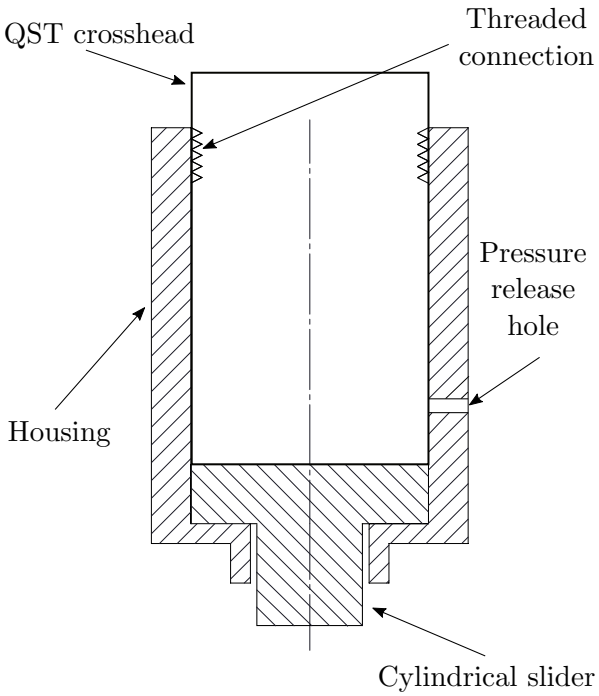

Figure 6.6: QST system crosshead connector

Crosshead connector: A crosshead connector is designed to directly connect to the crosshead of the Zwick machine to minimize the moving parts in the system. The connector, shown in Figure 6.6, consists of two parts designed specifically to reduce the possibility of damage to the crosshead threads in the case of a system failure of a specimen transmitting too much load. The two parts are made up of a housing and a cylindrical slider. An internal thread is machined on the housing that screws directly onto the external thread on the Zwick machine crosshead up until the point where the cylindrical slider contacts the tip of the Zwick machine crosshead. The internal diameter of the housing is defined by the outer diameter of the Zwick machine crosshead.

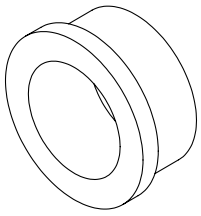

Figure 6.7: QST Brass bushing

Brass bushing: A brass bushing is incorporated into the system to ensure no binding between the input bar and the housing. The bushing is pressed into a shoulder located within the housing while the inner diameter of the bushing is defined by the diameter of the input bar. Bushings are preferred over rotating-element bearings because of their space and weight saving, ability to carry more load and their ability to accommodate small dimensional changes in the housing and shaft.

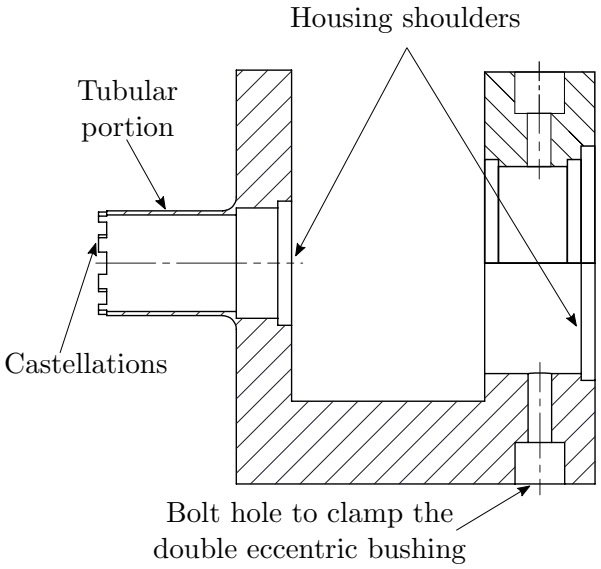

Figure 6.8: QST system housing

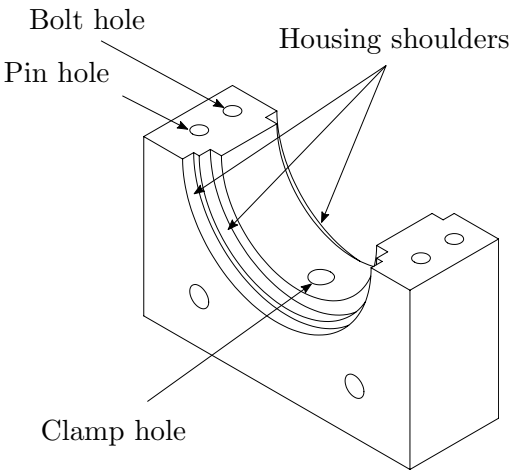

Figure 6.9: QST system bushing cover

Housing: A structure, a portion of which is to mimic the transmission tube in the dynamic system, houses the components of the QST system and fixes the system to the base plate. The structure is shown in Figure 6.8. It also fixes the outer portion of the specimen once it is mounted, thus making the angle of twist of the specimen purely dependant on the rotation of the input bar. This condition is only valid if the amount of twist in the tubular section is negligible relative to the angle of twist in the specimen. Castellations in the tubular portion operate as the mounting mechanism of the specimen to the housing. Housing shoulders fit the brass bushing and the double eccentric bushing described next. To restrict the motion of the double eccentric bushing, a threaded hole for a bolt is located underneath the housing to clamp the double eccentric bushing. Bolts located underneath the housing is used to connect the housing to the base plate.

Bushing cover: A bushing cover to house the double eccentric bushing is shown in Figure 6.9. The cover locates the double eccentric bushing on assembly. A clamp hole is incorporated in the system to allow a threaded bolt to clamp the double eccentric bushing, thus restricting its motion in all directions.

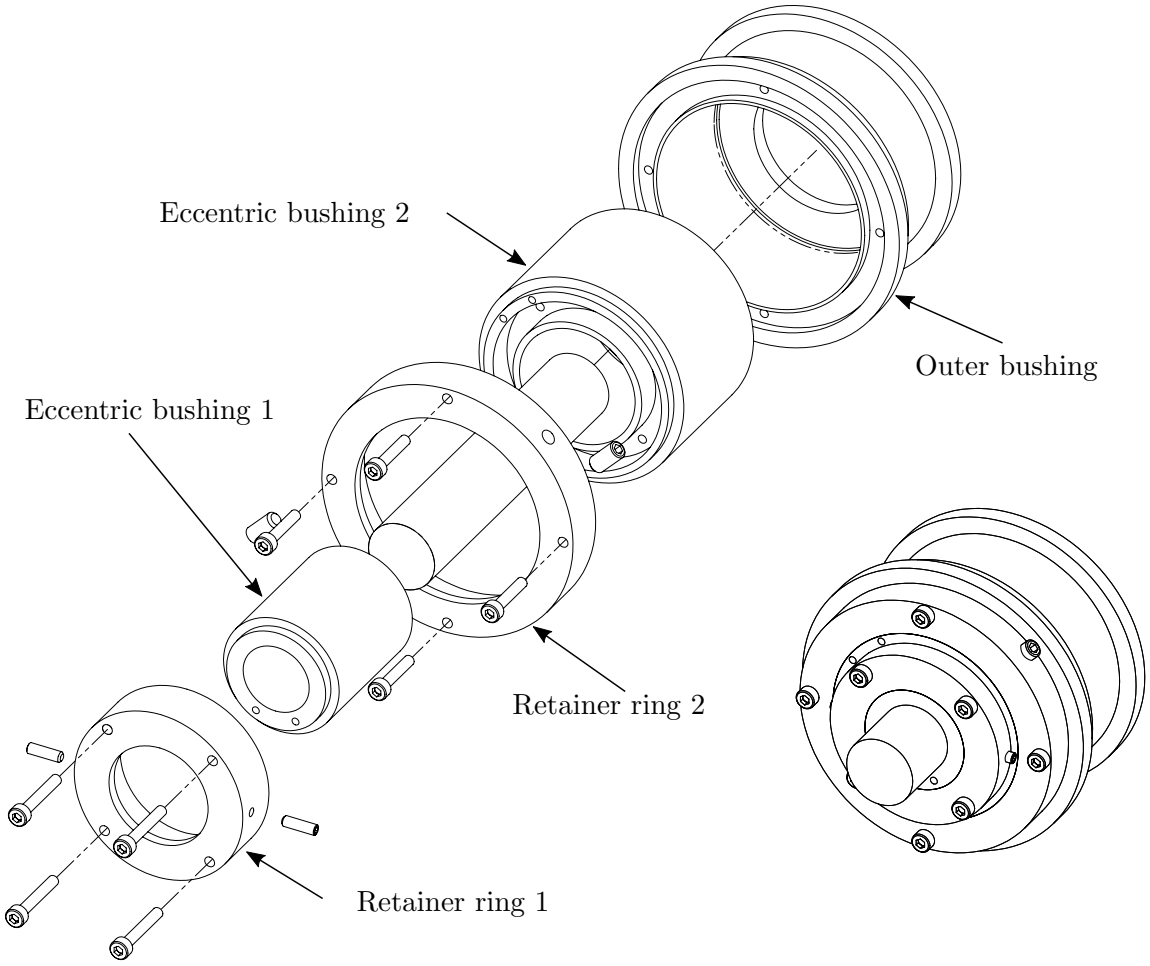

Figure 6.10: QST system double eccentric bushing

Double eccentric bushing: A double eccentric bushing consisting of an outer bushing, two eccentric bushings and retainer rings is shown in Figure 6.10. The design allows for appropriate compensation for misalignment of the input bar which is achieved by the rotation of the two eccentric bushings. Since the inner bore of the bushings is eccentric relative to the outer bushing surface, the adjustment potential is infinitely variable within a given range.

Each adjustable eccentric bushing consists of an outer body with an eccentric bore. By rotating either of the eccentric bushings within the outer bushing, the two eccentric bores may add or cancel changing the effective eccentricity of the inner bushing (Eccentric bushing 1 in Figure 6.10 above) relative to the outer bushing. The eccentricities of the two bushings have the same magnitude. Positioning the inner eccentric bushing 180° relative to the outer eccentric bushing results in a substantial eccentricity between the inner eccentric bushing and the outer bushing. Alternatively, a zero-offset cancels the two eccentricities out. Once locked in place, retainer rings prohibit axial movement of the eccentric bushings with the double eccentric bushing assembled using bolts and pins.

6.2 Instrumentation

Instrumentation for the QST system is required to measure the torque applied to the specimen and the angle of twist of the specimen. This is done by making use of the built-in Zwick machine data acquisition (DAQ) system, which measures the force at the load cell, the displacement of the crosshead, and the vertical velocity of the crosshead. Strain gauges located on the tubular portion of the housing are used to measure the torque transmitted to the specimen and any bending in the tube that may have originated from specimen mounting or specimen deformation.

6.2.1 Strain gauges

Two strain gauge stations are mounted on the surface of the tubular portion of the housing. One strain gauge station, model name KYOWA KFG-5-120-D16-11, is used for torque measurement while the other, model name KYOWA KFG-5-120-D16-11, is used for bending measurement. The gauge station for torque measurment is located 40 mm from the specimen end while the gauge station for bending measurement is located at the same distance but rotated by 90 °.

6.2.2 Strain gauge calibration

The strain gauges are calibrated by applying an appropriate static load and measuring the resultant output. Common methods for calibrating torque measuring strain gauges are by using a torque wrench calibration machine or by applying dead-weight loads to a torque arm. Strain gauges for bending are calibrated by applying dead-weight loads at known distances. The methods employed to calibrate the strain gauges in these experiments are described below.

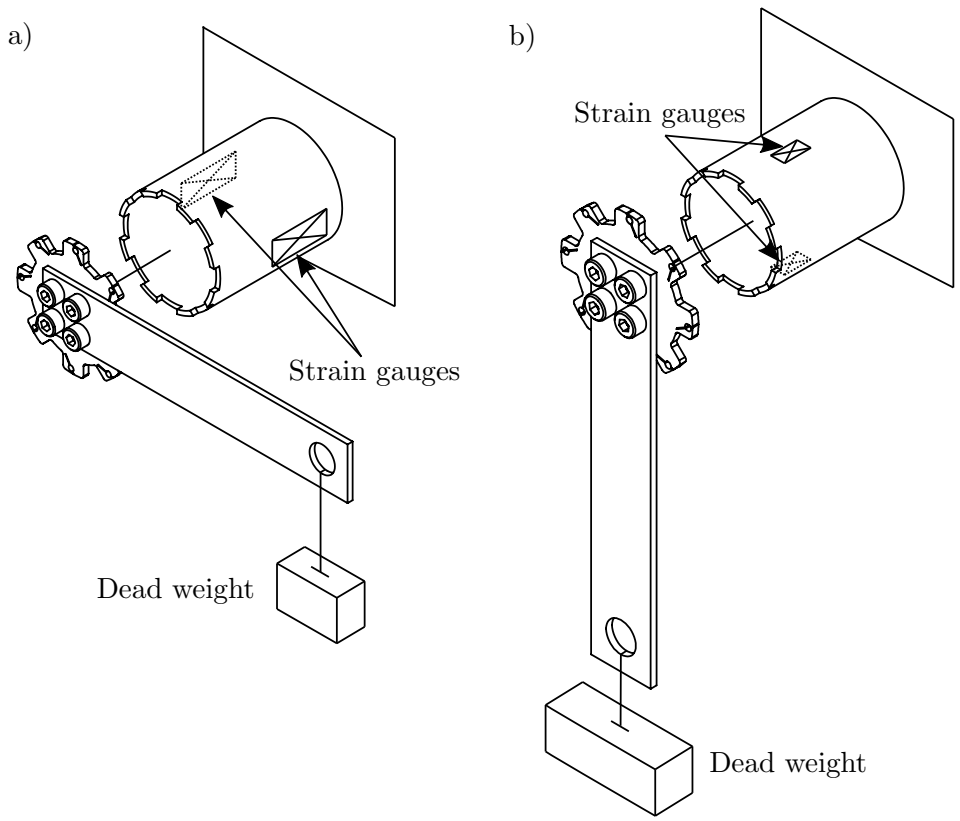

Figure 6.11: Calibration technique for a) torque and b) bending.

A dummy specimen, which is a specimen that has no gauge section, is manufactured with four through holes at its centre portion. A torque arm with the same through hole dimensions on one

of its sides allows for a bolted connection between the dummy specimen and the torque arm. A larger through hole is located on the other side of the torque arm that allows for the connection of the dead weight to the torque arm. The dummy specimen-torque arm assembly, shown in Figure 6.11 (a), is mounted onto the tubular portion of the housing after which a known weight is applied to the torque arm. The resultant output is compared to the applied weight and the experimental gauge factor is calculated. The four-active-arm arrangement having equal and opposite shearing strains of each gauge pair cancels any effects due to axial or bending strains as well as temperature for the strain gauges used to measure torsion.

The same dummy specimen-torque arm connection is used for bending calibration, however the connection is rotated by 90 ° and is shown in Figure 6.11 (b). A known weight is applied, and the experimental gauge factor is calculated using the applied weight and the resultant output. The experimental gauge factor is calculated by

$$\gamma = \frac{2V}{FE} \tag{6.1}$$

where γ is the shear strain at the surface of the bar, V is the output voltage of the bridge, F is the gauge factor of the strain gauges and E is the input DC voltage of the bridge. The strain gauge calibration will be further discussed in Chapter 7.

6.3 Calculations and analysis

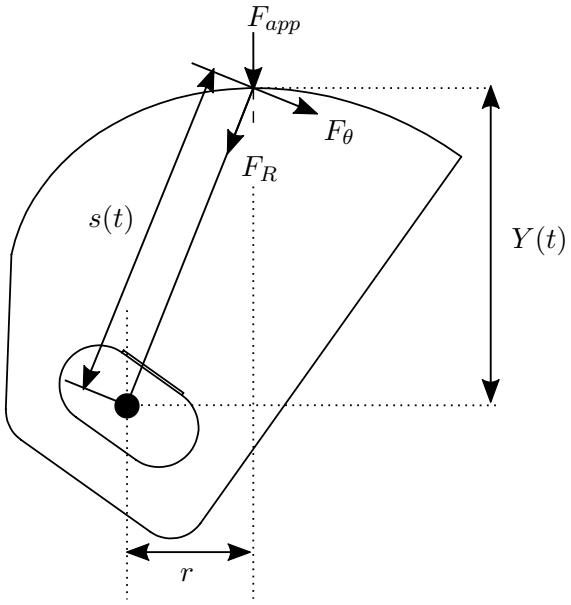

Figure 6.12: Forces on involute cam

Figure 6.12 shows the forces from the Zwick machine crosshead acting on the involute cam. Assuming the case where no friction is accounted for, then the torque can be calulated by

$$\mathrm{T} = F_{app} r \quad . \tag{7.1}$$

For the case where friction is accounted for, the torque is calculated by

$$\mathrm{T} = F_{app} r - \mu F_{app} Y(t) \tag{7.2}$$

where μ is the coefficient of friction between the involute cam and the crosshead connector.

Deflection due to the forces acting on the involute cam could cause unwanted loading at the specimen interface. The detailed analysis is shown in Appendix C. Figure 6.13 shows the expected input bar deflection resulting from the force applied by the Zwick machine. The figure shows that the maximum deflection occurs at the specimen interface with a value of approximately 0.017 mm which should be accounted for when adjusting for the concentricity of the input bar. It is worth noting, however, that the weight of the cam is not accounted for and its effect on the deflection may need to be investigated at a later stage. An image of the QST system is shown in Figure 6.14.

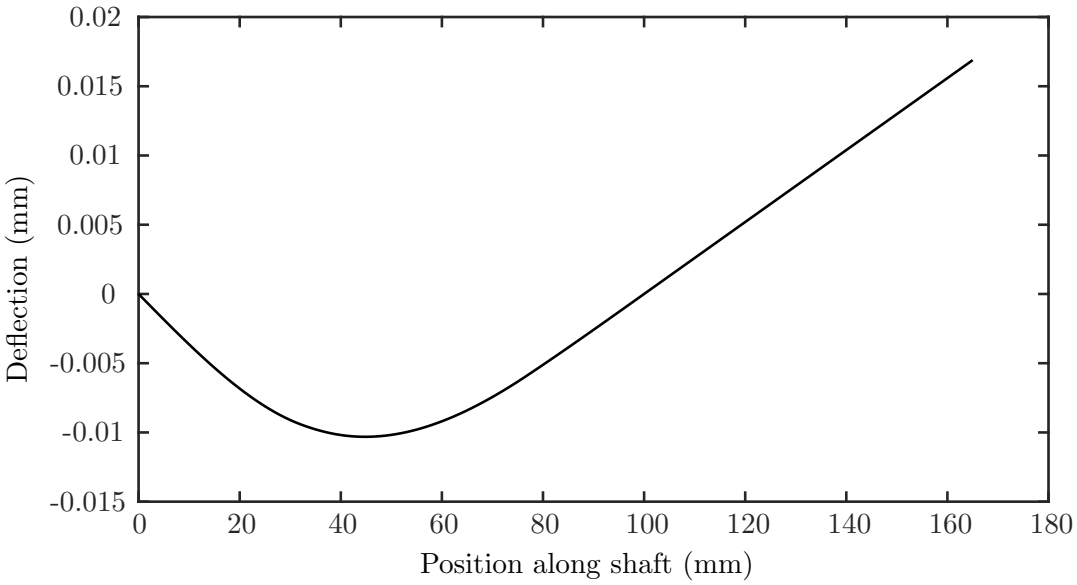

Figure 6.13: Deflection of input bar.

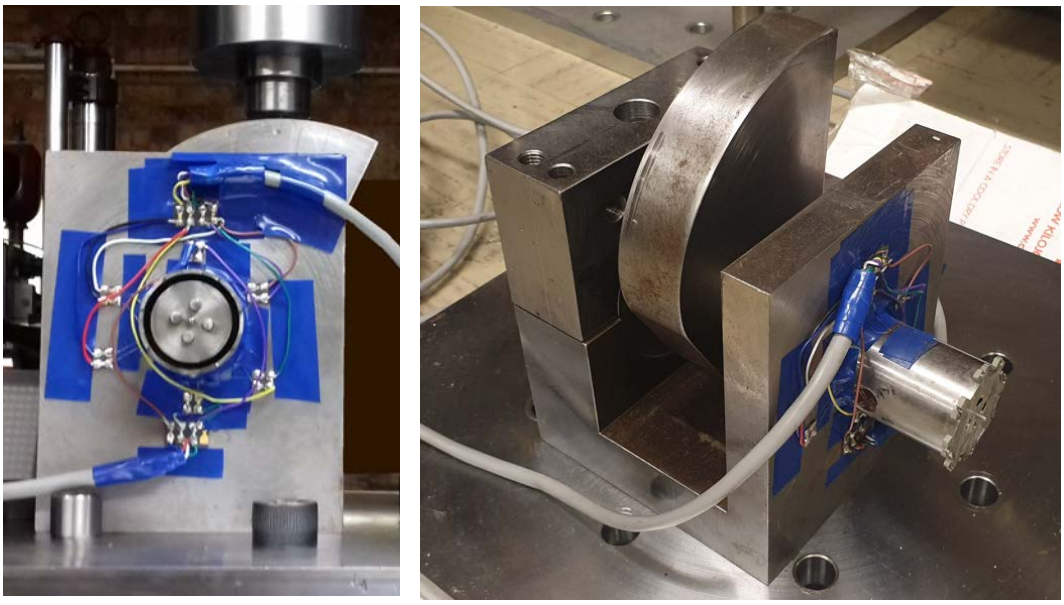

Figure 6.14: Photographs of QST system.

Chapter 7

Torsional split Hopkinson bar design

The torsional split Hopkinson bar (TSHB) is designed and manufactured for the purpose of characterising materials in torsion at high strain rates. The system described in this chapter is specifically built to characterise materials with low flow stresses in specimens manufactured from sheet metal. The TSHB apparatus is assembled on an I-beam and, in combination with picoscope software and strain gauges, data is gathered for every experiment.

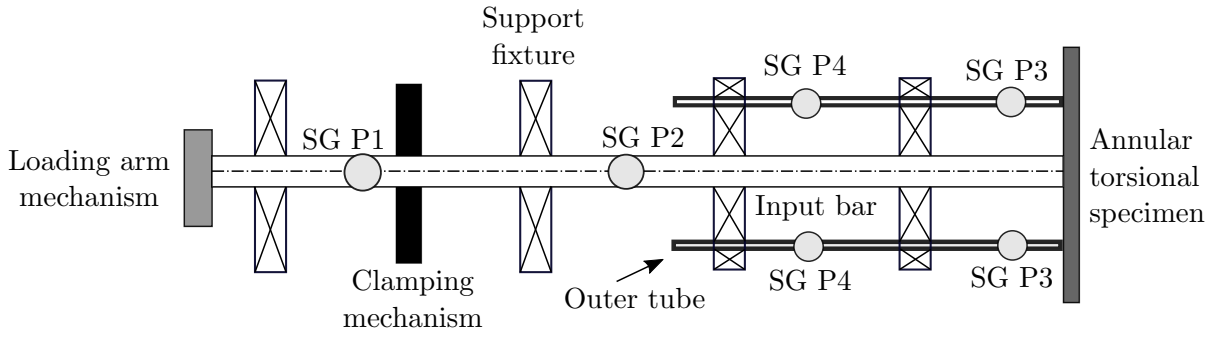

Figure 7.1: Torsional split-Hopkinson bar apparatus.

The components of the system, shown in Figure 7.1, consist of the alignment and bearing fixtures (support fixtures), load-application mechanism, incident (input) bar, transmission (outer) tube, clamping mechanism and the specimen and are described in detail in Section 7.1. The instrumentation of the system, which consists of four strain gauge stations, is captured using picoscope software, and is described in detail in Section 7.2.

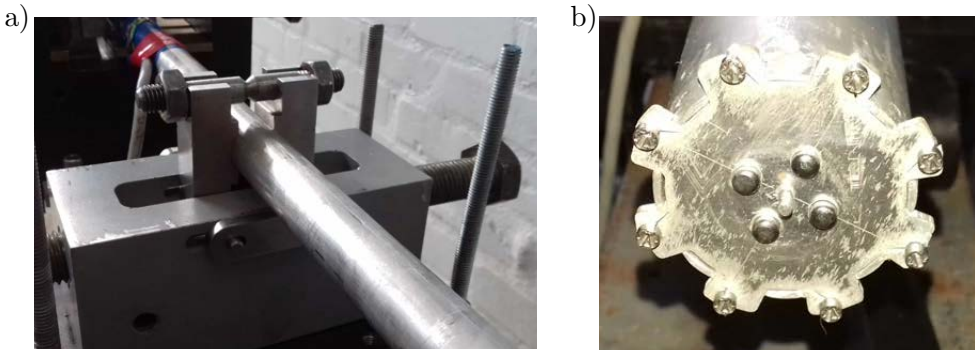

Figure 7.2: Photographs of TSHB components. a) Fracture-pin clamping mechanism and b) Fully mounted specimen.

7.1 Mechanical components

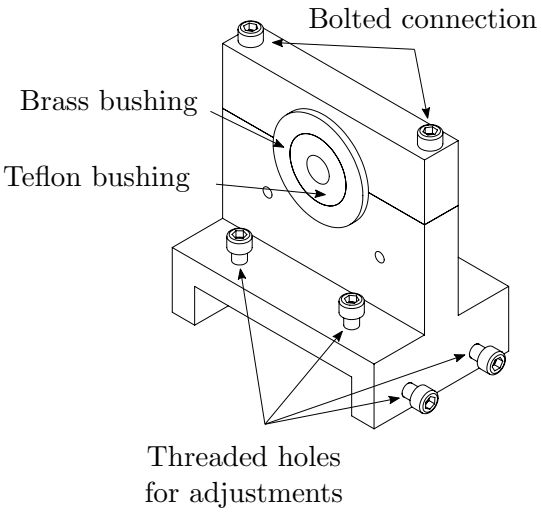

Figure 7.3: Support fixture

Support fixtures: The alignment and bushing fixture, shown in Figure 7.3, is designed to support both bars and allow for adjustment in three dimensions. The Teflon bushing, housed within a brass bushing, is designed to allow minimal friction between the bars and the support fixtures, while the support fixture base is machined to allow the brass bushing to seat and be assembled within the support structure. Threaded holes allow adjustment for height and side-to-side location of the support fixtures. The adjustment is done to ensure all components are co-axially located with the load-application mechanism. The support fixtures are clamped to the I-beam using two threaded rods that connect a specially machined bottom plate and the support fixture.

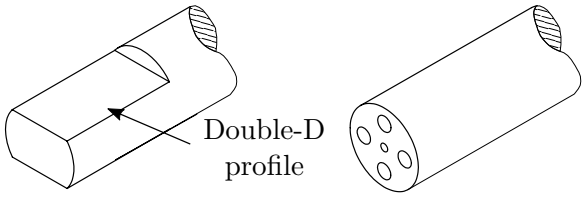

Figure 7.4: Two ends of incident bar

Incident bar: For the specimen to experience large strains, the incident bar should generate a shear stress that is significantly greater than the shear stress in the specimen. However, to be a reusable system, the torque induced in the incident bar should be below the yield strength of the incident bar. Another limitation is that it is necessary to ensure the prescribed shear stress produces an easily measurable shear strain to obtain useful information.

The incident bar, parts of which are shown in Figure 7.4, is fabricated from aluminium 7075 T6 and is specifically chosen for its high strength which allows for the possibility to load the bar with a high torque. To connect the incident bar to the load-application mechanism, two flats (double-D shaped) are machined on one side that are pressed directly into the hub of the load-application mechanism. To connect the incident bar to the specimen, four pin holes, together with a centre pin hole for locating the specimen, are machined on the other side. To match the existing clamping mechanisms, the diameter of the bar is 20 mm while the length is 3 m, which agrees with the requirement of one-dimensional stress wave propagation with the length to diameter ratio of 150:1.

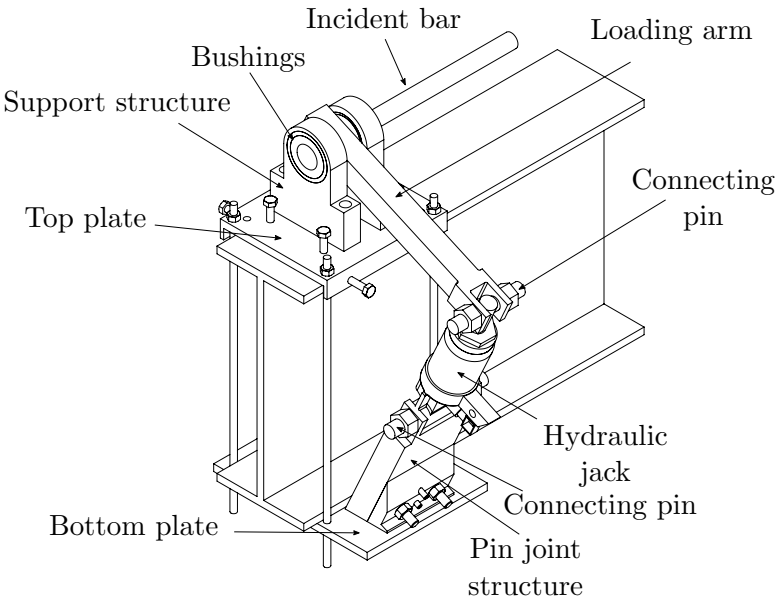

Figure 7.5: Load-application mechanism

Load-application mechanism: The load-application mechanism design used is the one described in Section 4.1.1 (shown in Figure 7.5) and is used together with a hydraulic jack. The mechanism is clamped to the I-beam using four threaded rods that connect a bottom plate and the load-application mechanism.

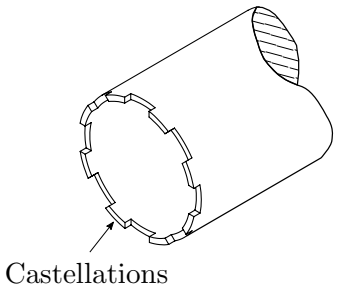

Figure 7.6: Transmission tube

Transmission tube: The transmission tube, shown in Figure 7.6, is fabricated from aluminium 6063 T6 tubing. The choice of this material, with a similar density and elastic stiffness to the incident bar, allows the stress wave to propagate with a similar speed through both bars. The diameter of the tube is influenced by the requirement that the torsional impedance in the two bars be as close as possible to each other (calculation in Section 7.3) as well as the transmission tube having a low input to output ratio to allow for a measurable strain. The length of the tube is 1.4 m with an outer diameter of 38.1 mm and wall thickness of 1.62 mm that results in a length to diameter ratio of approximately 1:36. To facilitate the mounting of the specimen, eight castellations are machined on the one end of the transmission tube with the geometry of the castellations matching the geometry of the QST system castellations.

7.2 Instrumentation

Instrumentation is crucial to obtaining information on the strain waves propagating in both bars. Important variables are the duration of the incident pulse which influences the shear strain obtained, as well as the magnitude of the incident pulse which influences the shear stress applied to the test specimen. These are measured using strain gauges located on both the

incident bar and the transmission tube. Finally, by post-processing the strain gauge signals, the stress vs strain data for the specimen is inferred.

7.2.1 Strain gauges

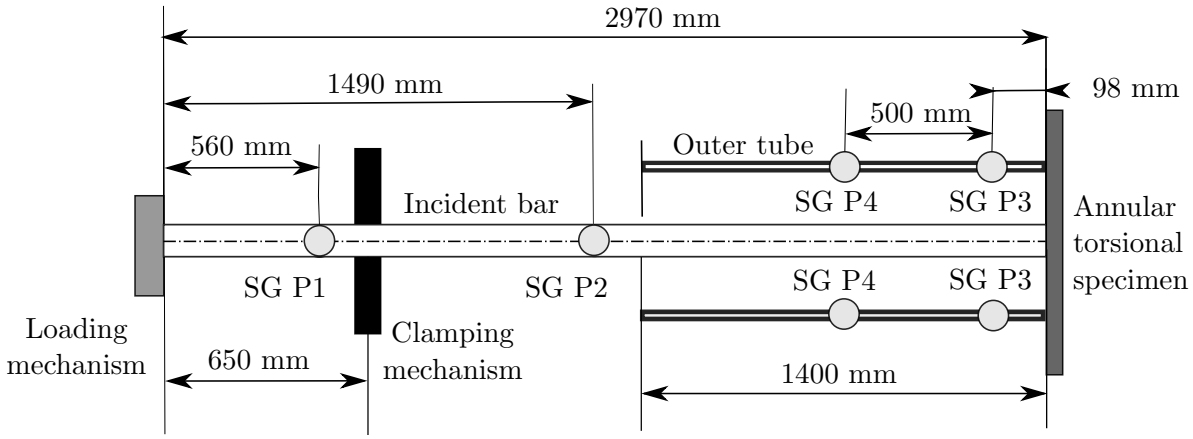

Figure 7.7: TSHB setup

Strain gauges are mounted on the surface of the bars to measure the rise time, amplitude and duration of the incident, reflected and transmitted waves. The properties of the strain gauges used are similar to the ones used for the QST system testing, however model name KFG-5-120-D16-23 was used due to the different bar material. On the incident bar, two strain gauge stations are configured. One station, located 560 mm from the loading end, is used to give a live reading of the torque loaded on the incident bar. The second station, located near the middle of the incident bar, is used as the primary measurement for the incident and the reflected waves. Its location ensures no interference between the reflected wave and the incident wave.

On the transmission (outer) tube, two strain gauge stations are configured as well. One station, located 98 mm from the specimen end, is used as the primary measurement of the transmission wave, while a second station located 598 mm from the specimen is used to get a better understanding of the reflected wave from the free end of the transmission tube. The two measurements are used in post-processing to determine the loading and displacement history of the specimen, as discussed in Chapter 9. Strain gauges are calibrated using the same technique used for the QST system.

The strain gauge signals are amplified by a pair of Texas-Instruments INA110 fast-settling FET-input instrumentation amplifiers with a total gain set at 1000. The amplifiers are housed in an amplifier box and powered by an external DC voltage source. A Picoscope 3424 and associated software is used to record and capture the strain gauge signals and is triggered by a falling edge in the voltage measured from the strain gauge located closest to the loading end of the incident bar.

A table of the information of the Picoscope is found in Table 7.1.

Number of channels	Bandwidth limit	Power source	Vertical resolution
4	10MHz	USB	12 bit

Table 7.1: Properties of Picoscope 3424.

7.2.2 Strain gauge calibration

Calibration is done experimentally using multiple weights for the dead weight physical calibration. A 6 point calibration curve is plotted that displays the shear strain relationship to the V/V output. A best-fit regression line is plotted with the regression equation based on the least squares technique. The regression lines are highly linear with very high coefficients of determination. The calibration factors are determined from the gradient of the fitted regression equations. Figure 7.8 shows the calibration curve for the incident bar while Figure 7.9 shows the calibration curve for the transmission tube.

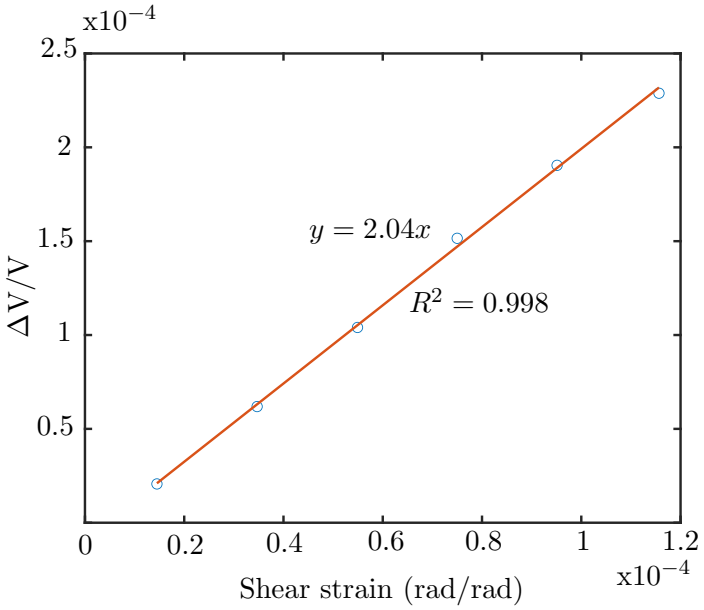

Figure 7.8: Calibration curve for the incident bar.

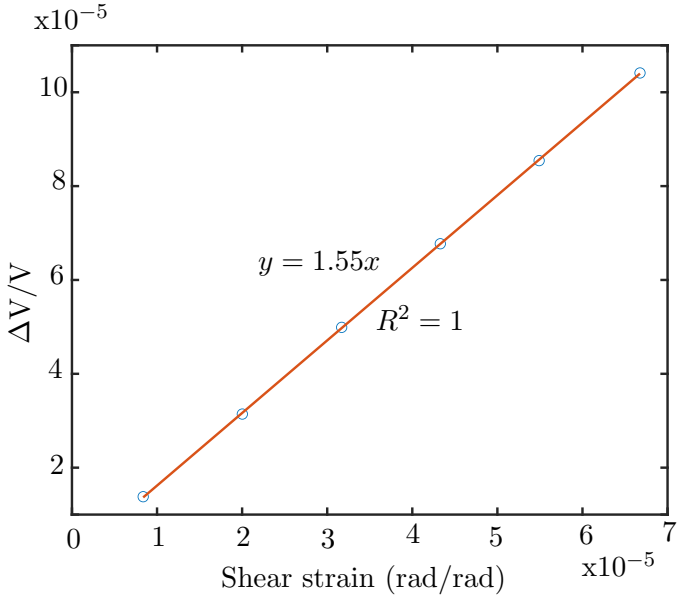

Figure 7.9: Calibration curve for the transmission tube.

7.3 Calculation and analysis

Position	Input bar	Output tube			
Option		1	2	3	4
Material	Al 7075	Al 6061	Al 6061	Al 6061	Al 6061
Shear modulus (GPa)	26,90	26,00	26,00	26,00	26,00
Outer diameter (mm)	20,00	38,10	38,10	35,74	38,10
Wall thickness (mm)	0,00	3,18	1,62	2,00	1,22
Inner diameter (mm)	0,00	31,74	34,86	31,74	35,66
Area (mm^2)	314,16	348,86	185,66	211,99	141,35
Second polar moment of area (mm^4)	15 707,96	107 232,49	61 890,64	60 545,02	48 116,88
Minimum torque (Nm)	10,00	10,00	10,00	10,00	10,00
Shear stress (MPa)	6,37	1,78	3,08	2,95	3,96
Shear strain	2,37E-04	6,83E-05	1,18E-04	1,14E-04	1,52E-04
Absolute strain ($\mu\varepsilon$)	118,33	34,16	59,19	56,76	76,14
Input to output ratio		3,46	2,00	2,08	1,55

Table 7.2: Comparison between transmission tube dimensions and input to output ratio.

Table 7.2 details the comparison between the available aluminium tube sizes and the resultant input to output ratios. Four tube sizes were considered where the ability to accommodate a large range of specimen gauge section widths and the input to output ratio being as low as possible, were the deciding factors. The tube size chosen was option 2 with an outer diameter of 38.1 mm with a wall thickness of 1.62 mm. This is because option 4 is not readily available and option 1 resulted in a larger input to output ratio. The last choice, being option 3, limits the specimen gauge section width potential and is therefore eliminated from consideration.

Chapter 8

Data processing

This chapter presents the data processing techniques adopted to measure the required mechanical properties. These include the technique used to convert rectangular specimen tensile test results to equivalent results for comparison with the annular in-plane torsional test results in the quasi-static regime. The equations used to obtain material properties for the QST and TSHB systems are also included.

8.1 Rectangular specimen equations

Material test data are often supplied as nominal stress and strain values. Therefore, the material test data would need to be converted from nominal stress vs strain values to equivalent stress vs strain values to allow comparison with the annular in-plane torsional specimen. The procedure for this conversion is documented in [41]. The nominal strain is expressed as

$$\varepsilon_{nom} = \frac{\Delta l}{l_0} \tag{8.1}$$

where Δl is the change in length and l_0 is the initial gauge length. The relationship between the true strain and the nominal strain is expressed as

$$\varepsilon_{true} = \ln(1 + \varepsilon_{nom}) \quad . \tag{8.2}$$

The nominal stress is expressed as

$$\sigma_{nom} = \frac{F}{A_0} \tag{8.3}$$

where F is the force data and A_0 is the initial gauge area. The relationship between the true stress and the nominal stress is expressed as

$$\sigma_{true} = \sigma_{nom}(1 + \varepsilon_{nom}) \quad . \tag{8.4}$$

Equations (8.2) and (8.4) are only valid up to the onset of necking, which corresponds to the ultimate tensile stress of the specimen. This is due to the deformation being uniform over the gauge length only up to the onset of necking. Assuming transverse plane-strain conditions (along with the von Mises yield surface which can be adopted since the material is ductile), the corresponding equivalent von Mises stress, $\overline{\sigma}_{eq}$, and equivalent strain, $\overline{\epsilon}_{eq}$, can be calculated from

$$\overline{\sigma}_{eq} = \frac{\sqrt{3}}{2}\sigma_{true} \tag{8.5}$$

and

$$\bar{\epsilon}_{eq} = \frac{2}{\sqrt{3}}\epsilon_{true} \quad . \tag{8.6}$$

The material test data often provides the total strain in the material. The total strain must be decomposed into the elastic and plastic strain components to match the approach taken in most classic metal plasticity models. The relationship for plastic strain is expressed as

$$\varepsilon^{pl}_{true} = \varepsilon^{t}_{true} - \frac{\sigma_{true}}{E} \tag{8.7}$$

where ε^{pl}_{true} is the true plastic strain, ε^{t}_{true} is the true total strain, σ_{true} is the true stress and E is the Young's modulus.

According to Hance [42], cold rolled thin sheet metals are typically anisotropic in nature because of the production processes they are subjected to. Normal anisotropy and planar anisotropy are the two aspects from which anisotropy is usually described. Normal anisotropy is the most frequently used anisotropy parameter which represents the strain ratio in the plane of the sheet metal and along its thickness. The parameter is determined experimentally by measuring the deformations in thickness and width of a rectangular cross-section tensile specimen and accuracy in its measurement is important since it is a crucial anisotropy parameter in software for simulations.

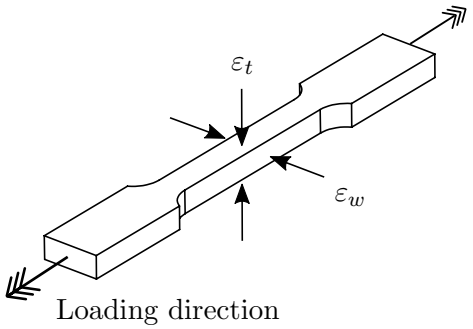

Figure 8.1: Tensile sheet specimen.

Figure 8.1 shows the related parameters for calculating the normal anisotropy value. The ratio of the logarithmic strain in the width and thickness directions of a rectangular cross-section tensile specimen is calculated from

$$R = \frac{\ln \frac{w_o}{w_f}}{\ln \frac{t_o}{t_f}} \tag{8.8}$$

where w_o is the initial width, w_f is the final width, t_o is the initial thickness and t_f is the final thickness. The normal anisotropy parameter, r_n, is defined as

$$r_n = \frac{R_0 + 2R_{45} + R_{90}}{4} \tag{8.9}$$

where R_0, R_{45} and R_{90} are the R-values for $0\,^\circ$, $45\,^\circ$ and $90\,^\circ$ orientations with respect to the sheet's rolling direction respectively.

8.2 Annular in-plane torsional specimen equations

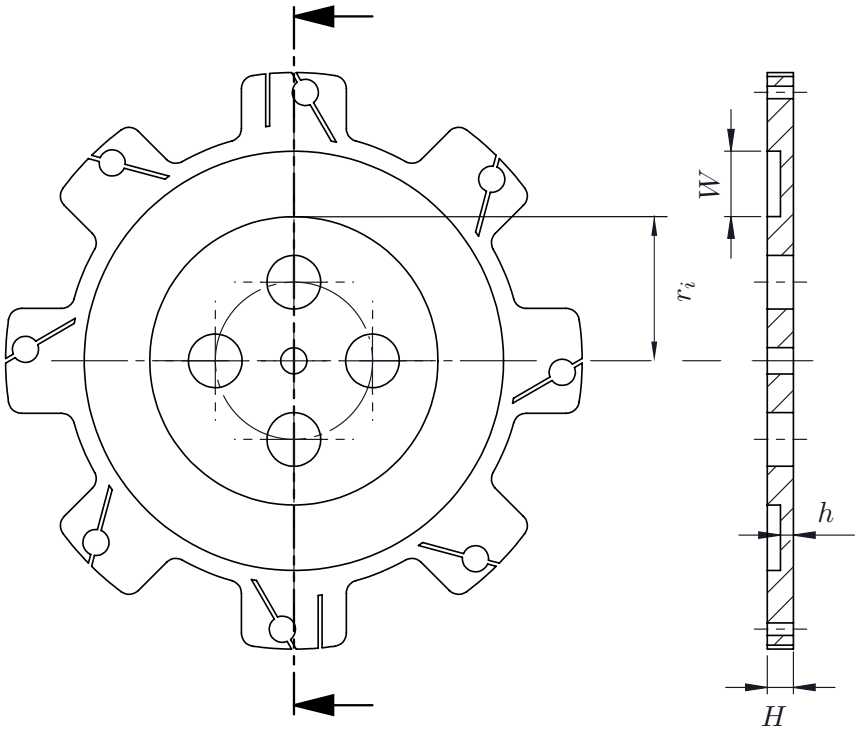

Figure 8.2: Annular in-plane torsional specimen dimension variables.

As in section 5.3, the shear stress, τ, is calculated by

$$\tau = \frac{T}{\pi {r_i}^2 h} \tag{6.15}$$

where T is the torque, h is the local thickness of the gauge section (during deformation and at point of facture), and $r_i = D/2$ is the inner-most radius. The shear strain is calculated by

$$\gamma = \tan\phi = \frac{r_i \theta}{W} \tag{6.16}$$

where θ is the angle of twist, W is the width of the gauge section, and r_i is the inner-most radius. Using the isotropic von Mises flow criterion, the equivalent stress and equivalent strain can be obtained. However, since the orientation of the rolling direction relative to the shear loading direction changes over the circumference, the annular in-plane torsional specimen results in an averaging of the planar anisotropic properties [43]. Using Hill's anisotropic flow criterion, the normal anisotropy can be taken into account [44] with the equivalent stress and the equivalent strain calculated using

$$\sigma_f = \sqrt{3}\tau \sqrt{\frac{2(2r_n + 1)}{3(r_n + 1)}} \tag{8.10}$$

and

$$\epsilon_{eq} = \frac{\gamma}{\sqrt{3}} \sqrt{\frac{3(r_n + 1)}{2(2r_n + 1)}} \quad . \tag{8.11}$$

8.3 QST system processing

A QST system test generates a data set that is imported as a `.mat` file into MATLAB. The file consists of force, linear displacement, bending strain and torsional strain data. The data is processed in a MATLAB script (available in digital format and can be accessed via the UCT DMP library) that determines the shear stress and plastic shear strain data for a given specimen. The following operations are executed by the MATLAB program. Representative results from one data set are also shown.

- The script first requires the user to enter the specific datafile name (corresponding to a specific specimen). This is followed by entering the measured specimen gauge section thickness and specimen gauge section width. The mean dimensions of multiple measurements of the gauge section thickness and gauge section width are used.
- The unprocessed force vs displacement data is plotted as a graph. A representative result is shown in Figure 8.3.

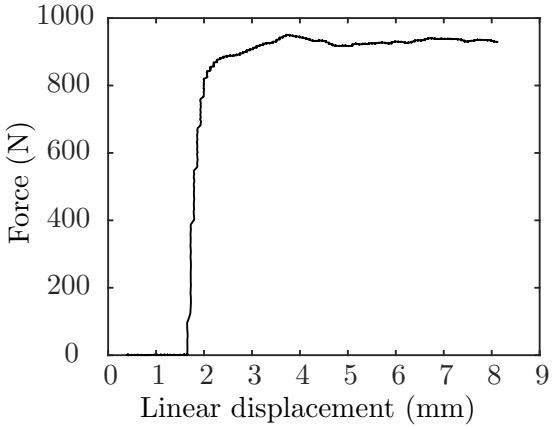

Figure 8.3: Experimentally obtained force vs displacement curve.

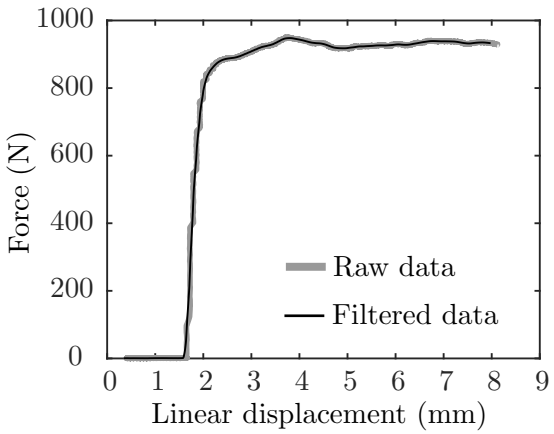

Figure 8.4: Comparison of the zeroed raw data vs filtered data.

- The initial data may be offset slightly due to environmental factors. Correcting of the offset is required and is done by either adding or subtracting an offset force value from the entire force data set. The offset is found by averaging the force data points that are located before the intial pulse commences. Once the measured force begins to drop appreciably, the data is truncated, as this may be associated with the onset of out of plane loading.
- The data is filtered using the built-in moving average filtering technique in MATLAB. The technique smooths the data by replacing each data point with the average of the neighbouring data points defined within the span and is comparable to lowpass filtering [45]. The number of data points used is user-defined with the optimum selection being the filter length that increases the smoothness of the data without significantly blunting the sharp transitions in the data. The zeroed raw data is compared to the filtered data and is shown in Figure 8.4.

- The measured force, F, is converted to an inferred torque, T_i, using

$$T_i = Fr \tag{8.12}$$

where r is the moment arm. The displacement, Y, is converted to an angular rotation of the involute cam, θ_c, using

$$\theta_c = \frac{180Y}{\pi r} \quad . \tag{8.13}$$

The strain gauge data is converted into torque data, T_o, using

$$T_o = \frac{2G_t J_t \varepsilon}{r_t} \tag{8.14}$$

where G_t is the shear modulus of the tubular section, J_t is the second polar moment of inertia of the tubular section, ε is the measured strain, and r_t is the radius of the tubular section. The shear modulus is obtained from the technical data sheet provided by the supplier of the material. The bending moment data, M_B, is calculated from

$$M_B = \varepsilon E Z \tag{8.15}$$

where E is the elastic modulus and Z is the section modulus of the tubular section. Any error in the supplied values is corrected through the use of calibrated conversion factors as described in Section 7.2.

- A representative result is shown in Figure 8.5 that compares the inferred torque for the case where no friction is assumed, T_i, and for the case where a coefficient of friction is applied, T_f. The coefficient of friction, μ, is determined by matching the inferred torque to that measured using the strain gauges, T_o. A friction coefficient of approximately 0.19 was experimentally determined. T_f is calculated from

$$T_f = Fr - \mu FY \quad . \tag{8.16}$$

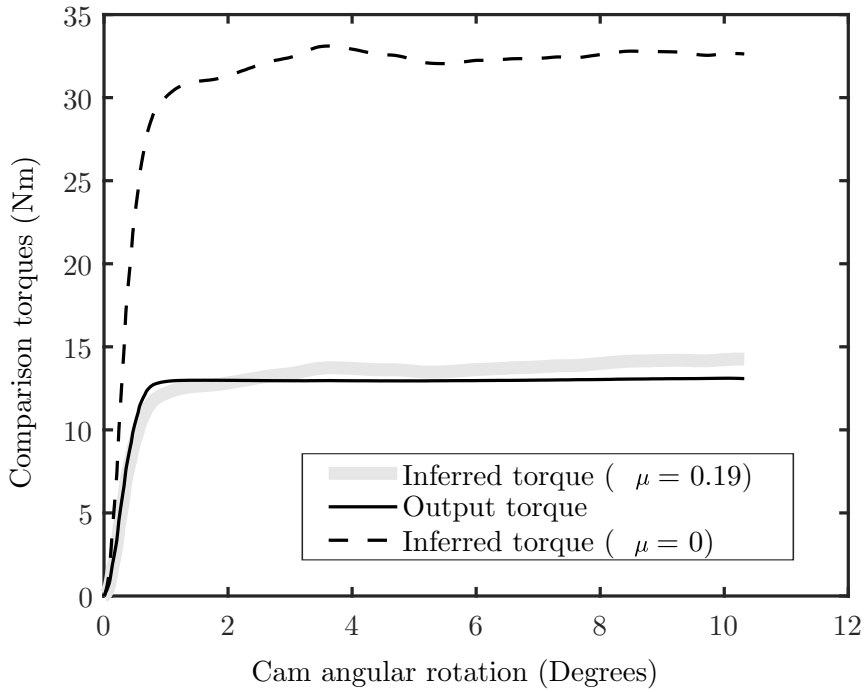

Figure 8.5: Measured torque to inferred torque obtained from the QST system test.

- The shear stress, τ, can be determined from the torque inferred from the strain gauge measurements from

$$\tau = \frac{T_o}{2\pi {r_i}^2 h} \tag{8.17}$$

where r_i is the inner-most diameter of the specimen gauge section and h is the specimen gauge thickness. Assuming the angular deflection of the regions outside the gauge section of the specimen and the machine compliance are small, the average shear strain, γ, is determined from

$$\gamma = \frac{r_i \theta}{W} \tag{8.18}$$

where W is the specimen gauge width. The shear stress at the inner-most diameter of the specimen gauge section vs uncorrected average shear strain is plotted and a representative result is shown in Figure 8.6.

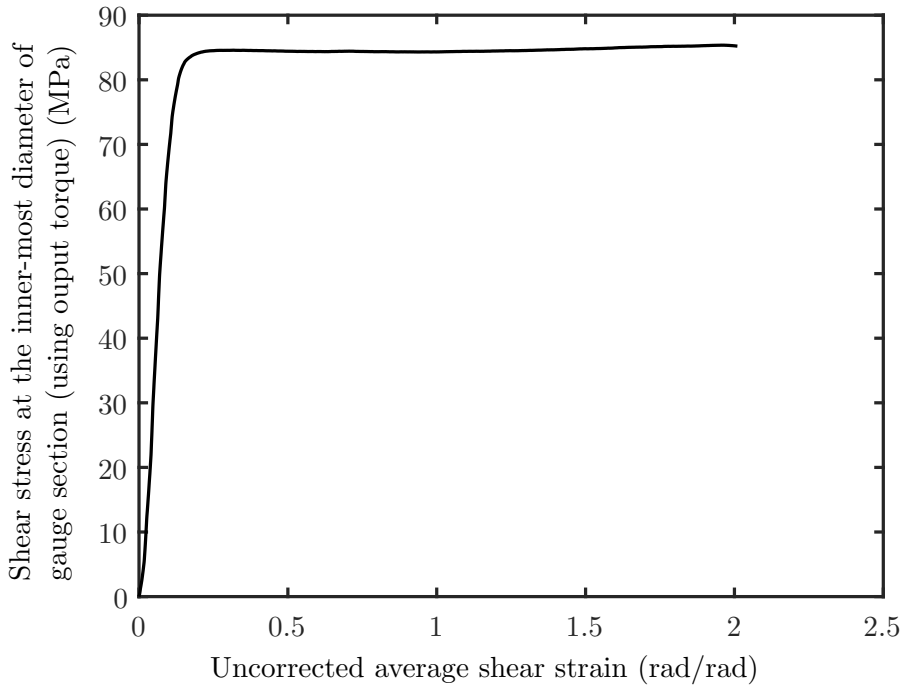

Figure 8.6: QST system shear stress at the inner-most diameter vs uncorrected average shear strain.

8.4 TSHB data processing

The raw data obtained from the strain gauges are processed to determine the shear stress vs shear strain history of the annular in-plane torsional specimen in the dynamic strain rate regime. A typical set of unprocessed data is shown in Figure 8.7. The initial signal in the incident bar typically consists of an incident wave and a reflected wave while the initial signal in the transmission tube consists of a single transmitted wave. For the example shown, one strain gauge on the incident bar was used to give a measure of the torque stored in the clamped portion of the incident bar, V_L. A second strain gauge on the incident bar was used to measure the incident wave, V_i. On the transmission tube, two strain gauges were used to measure the transmitted wave, V_{1t} and V_{2t}. A MATLAB script (available in digital format and can be accessed via the UCT DMP library) was written to do the data processing and it executes the following operations. Representative results from one data set are also shown.

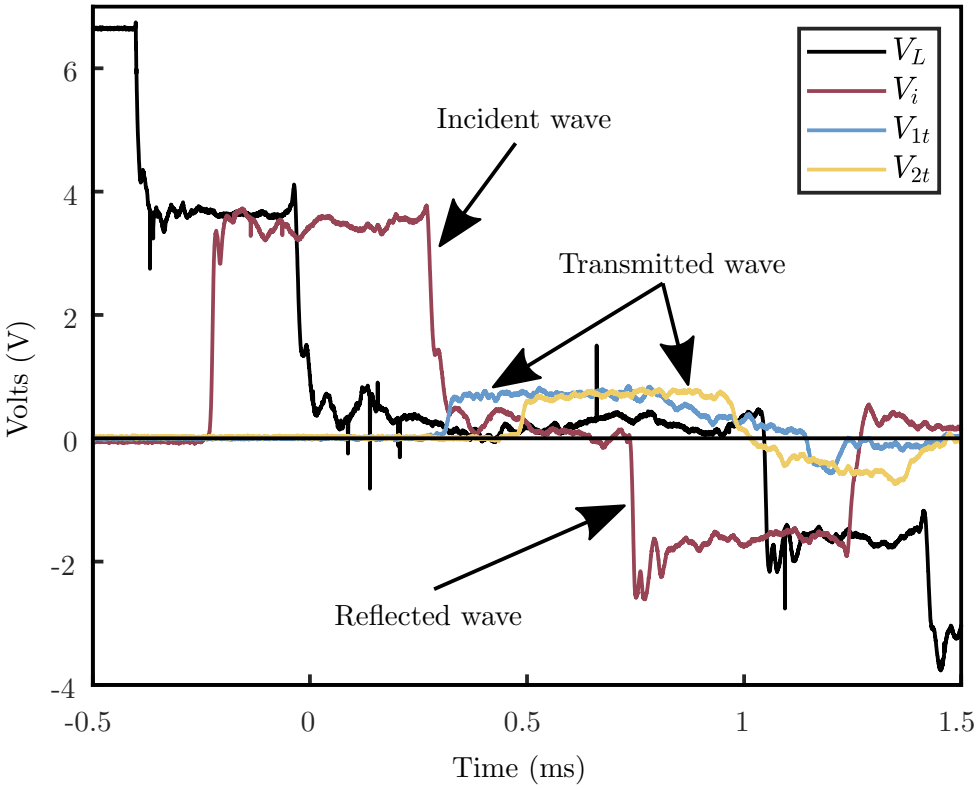

Figure 8.7: Unprocessed experimentally obtained TSHB voltage vs time curves.

- The script first requires the user to enter the specific datafile name (corresponding to a specific specimen). This is followed by entering the specimen gauge thickness and gauge width as well as the excitation voltage used for the specific experiment.
- The voltage measured may not be 0V when no strain is present. This is due to environmental factors (such as room temperature etc). This is adjusted for by adding or subtracting an averaged value from the entire data set of each curve. The averaged value is obtained by selecting the range limits on each curve prior to the initial pulse commencing.
- The data is filtered using the built-in MATLAB filtering function `medfilt2`. A different filtering technique is used for the TSHB testing since there is more high frequency noise present. The filtering function performs median filtering which is a common nonlinear method for noise suppression [46]. A MATLAB figure shows a comparison of each curve's

raw curve against its filtered curve (with offset correction performed on both curves). An example of such a comparison is shown in Figure 8.8.

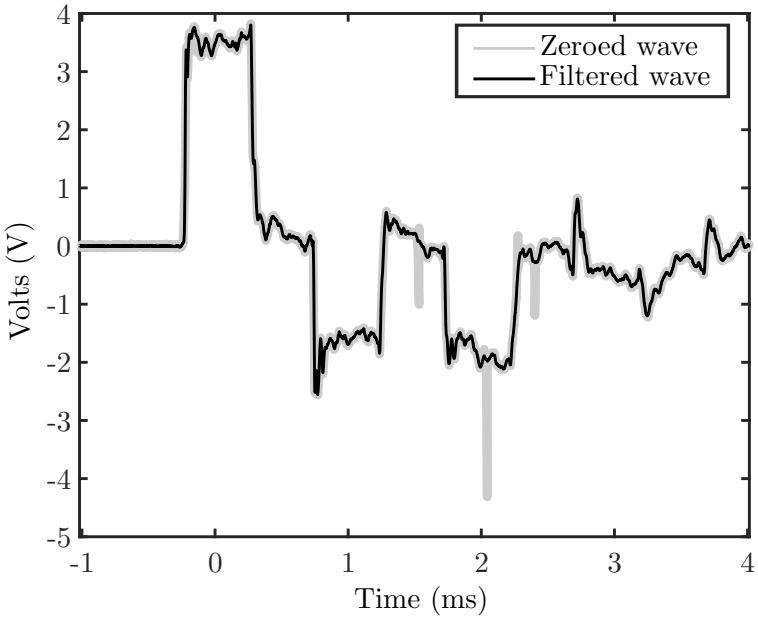

Figure 8.8: Comparison of the raw TSHB data vs filtered TSHB data for one strain gauge.

- The rise time, duration and fall time of the waves are calculated. Firstly, the maximum slope of the initial rising wave's linear region is found. A straight line is then plotted over the linear region using the maximum slope with the x-intercept of the straight line taken as the beginning of the rising wave. Similarly, the maximum slope of the initial falling wave is found after which a straight line is plotted over the linear region with the x-intercept taken as the end of the falling wave. The duration of the initial wave is found by calculating the difference between the two x-intercept values.

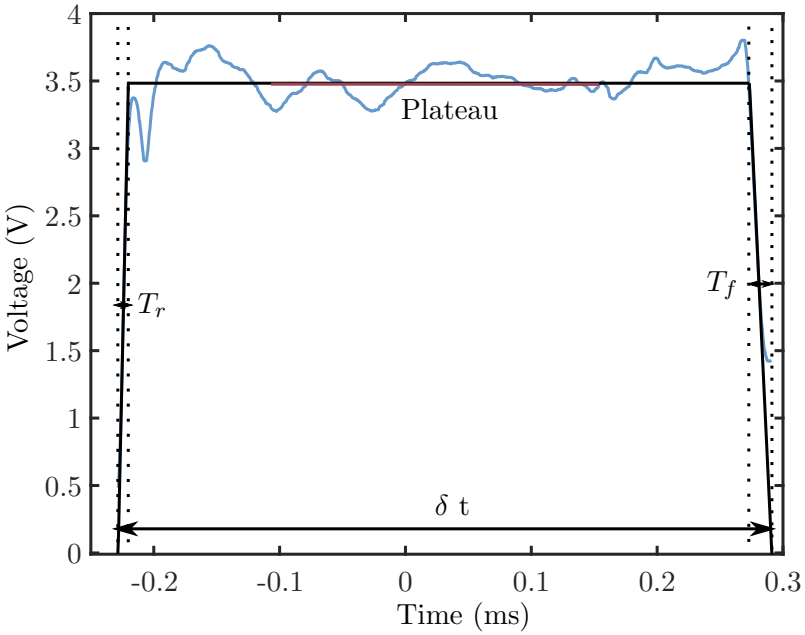

Figure 8.9: The incident wave with a rise time, T_r, duration time δ t and fall time, T_f.

- The plateau of the initial curve is found by firstly locating the mid-point of the duration of the curve. The mean of the region that lies 25 % of the duration on either side of the mid-point is then calculated and taken as the plateau value. This is done to ensure that the rise and the tail of the pulse is not captured when calculating the plateau value and that the data used purely reflects the plateau region of the pulse. The plateau curve is then horizontally extended and the point where the plateau curve intercepts with the rising wave is taken as the end of the rise time. Similarly, the point where the plateau curve intercepts with the falling wave is assumed to be the beginning of the fall time. Figure 8.9 illustrates the result of this process. The approximate constant strain rate value is calculated in the same manner, with the plateau of the curve taken as the approximate constant strain rate value.

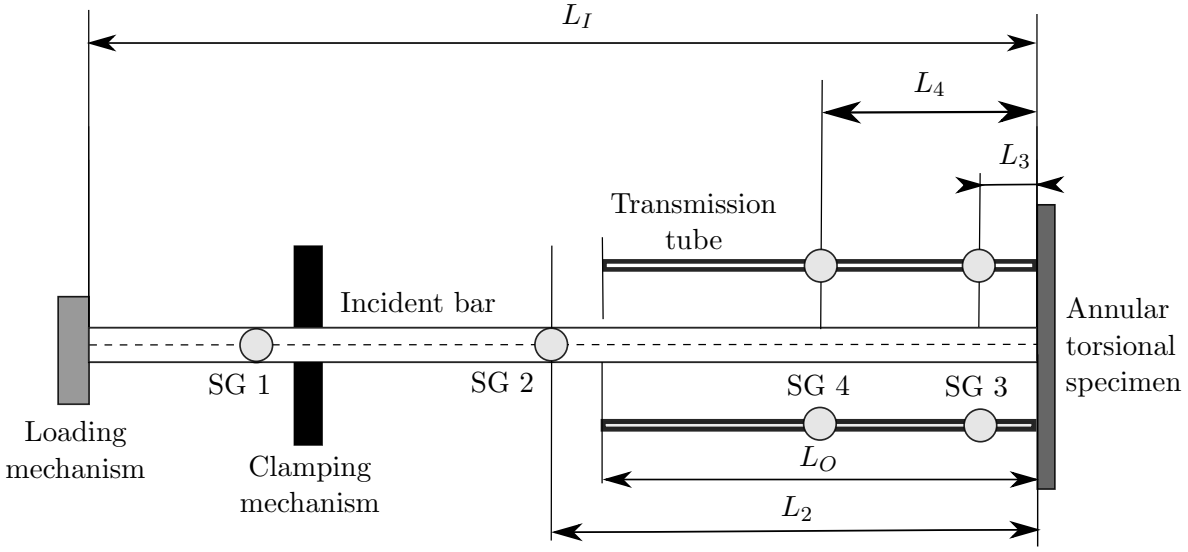

Figure 8.10: Schematic representation of the stored-torque TSHB system.

- A schematic representation of the TSHB experimental setup is shown in Figure 8.10. Using the variables shown in the schematic, the program calculates the experimental shear wave speed and shear modulus of each bar. The method for this calculation is shown in Appendix D. The shear wave speed is then used together with the distances from the strain gauges to the specimen interfaces to temporally shift the curves so they correspond with the specimen interfaces. The physical distances can also be verified at this point using the measured signals. The time shifts are determined from

$$t_2 = \frac{L_2}{c_i} \quad ; t_3 = \frac{L_3}{c_o} \quad ; t_4 = \frac{L_4}{c_o} \tag{8.19}$$

where c_i is the shear wave speed of the incident bar and c_o is the shear wave speed of the transmission tube. Figure 8.11 shows a representative result of the shifted waves at the specimen interface. The wave used for measuring the stored torque is omitted and the reflected wave, V_r, is included.

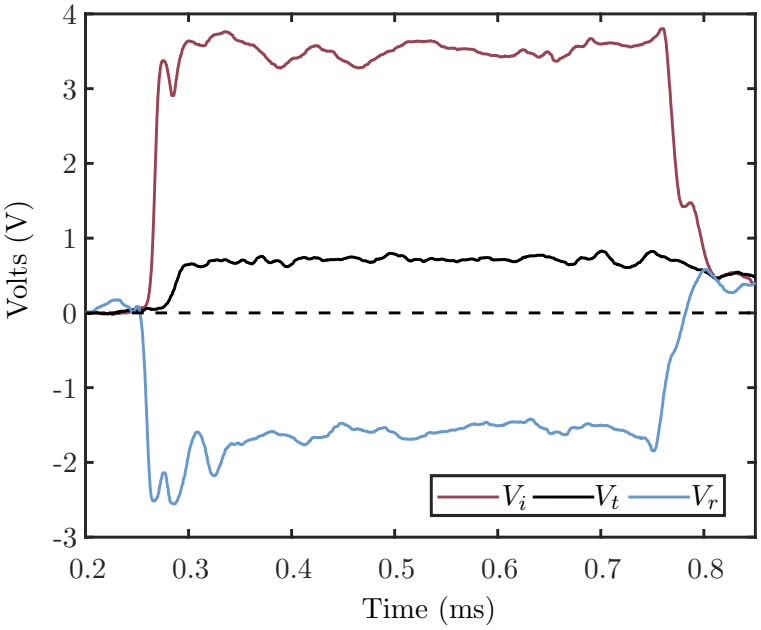

Figure 8.11: Typical wave data shifted to the specimen interface.

- The raw voltage data signals are converted to torque using

$$T = \left(\frac{4GJ}{d}\right)\left(\frac{\varepsilon K}{V_e}\right) \tag{8.20}$$

where T is the torque, G is the measured shear modulus of the bar, J is the second polar moment of inertia of the bar and d is the outer diameter of the bar. ε is the measured strain, K is the calibrated gauge factor and V_e is the excitation voltage.

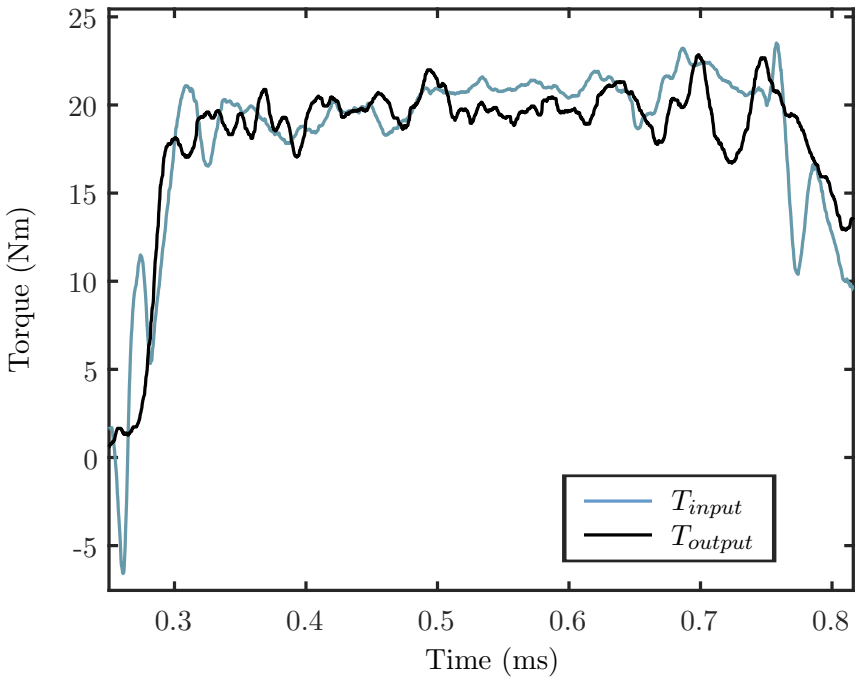

Figure 8.12: Equilibrium across the interfaces of the specimen.

Figure 8.12 shows a comparison between the torque transmitted to the specimen based on the incident wave, T_{input}, and the torque transmitted to the specimen based on the transmitted wave, T_{output}. The figure allows for the evaluation of the specimen equilibrium condition. This is done using

$$T_i + T_r = T_t \quad . \tag{8.21}$$

- Yu et al. [5] details the equations used to obtain the required material properties. The angular velocity of the incident bar, $\dot{\theta}_i$, and the angular velocity of the transmission tube, $\dot{\theta}_t$, are determined using

$$\dot{\theta}_i = \frac{T_i(\tau_i) - T_r(\tau_r)}{(\rho J c)_i} \tag{8.22}$$

and

$$\dot{\theta}_t = \frac{T_t}{(\rho J c)_t}(\tau_t) \tag{8.23}$$

where ρ is the density of the bar, $\tau_i = (t + t_2)$ is the shifted time array for the incident wave, $\tau_r = (t - t_2)$ is the shifted time array for the reflected wave and $\tau_t = (t - t_3)$ is the shifted time array for the transmitted wave. The angular velocities are used to determine the shear strain rate, $\dot{\gamma}$, using

$$\dot{\gamma} = \frac{r_i(\dot{\theta}_i - \dot{\theta}_t)}{W} \tag{8.24}$$

where r_i is the inner-most radius of the gauge section and W is the specimen gauge width. The total shear strain of the specimen, γ, is obtained using

$$\gamma = \int_0^t \dot{\gamma}(t)dt \quad . \tag{8.25}$$

The integration is performed using the built-in MATLAB numerical cumulative trapezoidal integration function `cumtrapz` [47]. Lastly, the stress in the specimen, τ, is determined using

$$\tau = \frac{1}{2\pi {r_i}^2 h} T_t(\tau_t) \tag{8.26}$$

where h is the specimen gauge thickness.

- Figure 8.13 shows a representative result of the shear stress at the inner-most radius of the specimen gauge section vs uncorrected average shear strain.

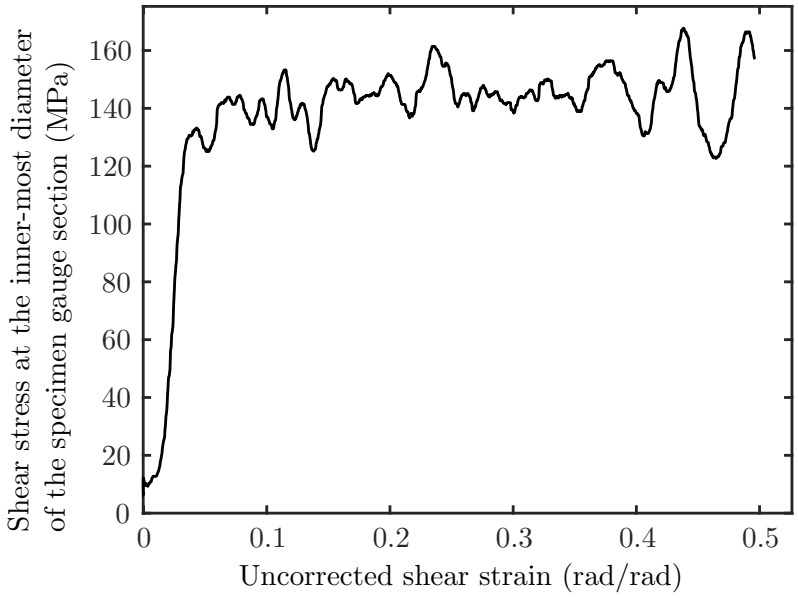

Figure 8.13: TSHB shear stress at the inner-most diameter vs uncorrected average shear strain.

8.5 Technique used to obtain the plastic strain

The maximum slope of the linear region is found using the numerical derivative of the smoothed data. The slope of the linear region represents a combination of the specimen compliance, the elasticity of the specimen and any 'bedding in'. Using the maximum slope, a linear best-fit line is plotted.

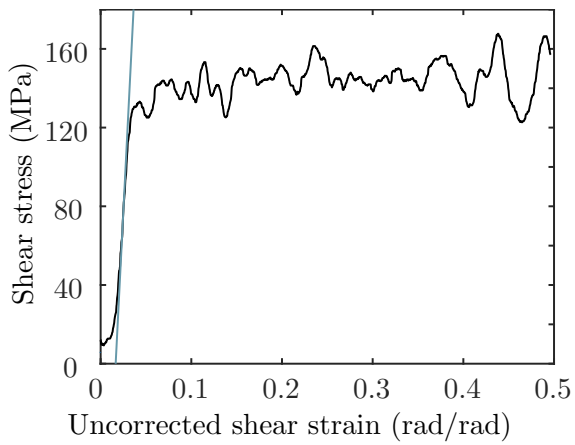

Figure 8.14: TSHB shear stress at the inner-most radius vs uncorrected average shear strain with the linear best-fit line.

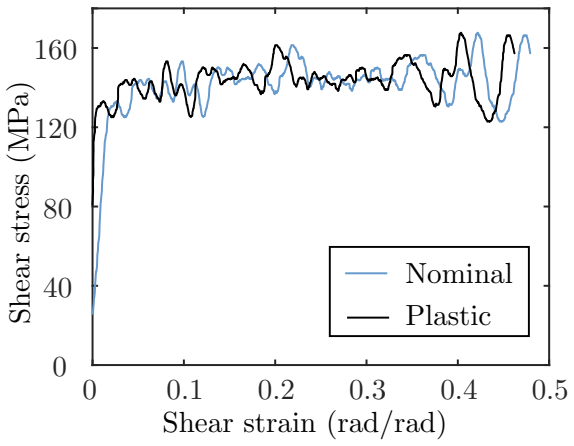

Figure 8.15: TSHB shear stress at the inner radius vs average shear strain for nominal and plastic strain.

The parameters of the linear best-fit line are used to plot a straight line that extends beyond the elastic region, as shown in Figure 8.14. Any non-zero x-intercept is assumed to be due to specimen compliance as well as any 'bedding in' of the specimen in its castellated fixtures. Therefore, to obtain only the elastic and plastic strain components, the x-intercept is removed by subtracting all the strain data points by the x-intercept value. The plastic strain is calculated

using

$$\gamma_p = \gamma_{nom} - \frac{\tau_{nom}}{G_{test}} \tag{8.27}$$

where G_{test} is the elastic slope of the shear stress vs strain curve. A comparison of the nominal and plastic shear strain are shown in Figure 8.15. Figure 8.16 shows a similar comparison to Figure 8.15 for a QST system test.

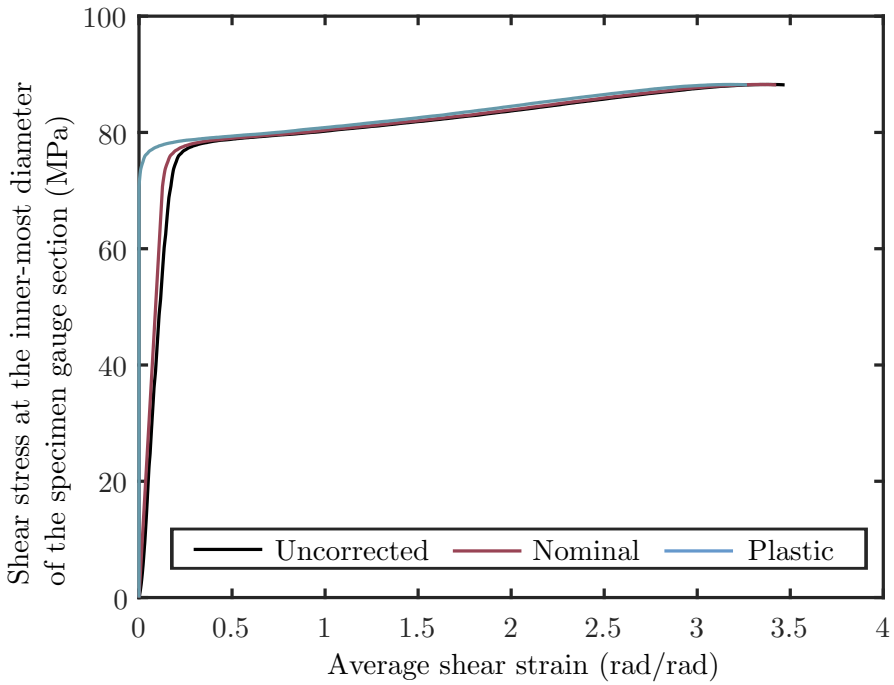

Figure 8.16: Comparison of the various shear strains calculated to obtain the plastic shear strain for a QST system test.

8.6 Regression analysis procedure

The inverse analysis methodology of Oliveira [48] is adopted to enable the determination of the parameters for the assumed constitutive equation. The methodology incorporates a user-defined objective function which optimises the parameters by evaluating the error between the experimental results and the numerical results. Robust numerical models require reliable input data which include specimen geometry and material data, as well as an appropriate material constitutive law and the determination of its parameters at different conditions. The objective function is expressed as

$$\emptyset = \sqrt{\sum_{i=1}^{n} \left(\frac{y_i^{exp} - y_i^{num}}{n} \right)^2} \tag{8.28}$$

where n is the number of experimental data points, y_i^{exp} are the experimentally measured data points and y_i^{num} is the numerically computed strain as a function of the unknown material parameters.

MATLAB's Global Optimization toolbox is used to develop the optimization procedure for the regression analysis. The routine finds the minimum of a function which is expressed as the

sum of squares of nonlinear functions. More experimental tests should be done over a range of specimen geometries and strain rates to validate the optimization procedure. In the current work, due to the testing being done at room temperature and the assumption of negligible adiabatic heat rise, the temperature term and its associated constants are not accounted for in the regression analysis. A good material model exhibits a high R^2 value where the R^2 indicates how well the observed results correspond to those predicted using the specific material model [19]. The R^2 value is expressed as

$$R^2 = 1 - \frac{\sum_i (y_i^{num} - y_i^{exp})^2}{\sum_i (y_i^{num} - \overline{y})^2} \tag{8.29}$$

where $\overline{y}$ is the mean of the observed data and is expressed as

$$\overline{y} = \frac{1}{n} \sum_{i=1}^{n} y_i^{num} \quad . \tag{8.30}$$

Figure 8.17 shows a representative result of the regression curve against the experimetnal data.

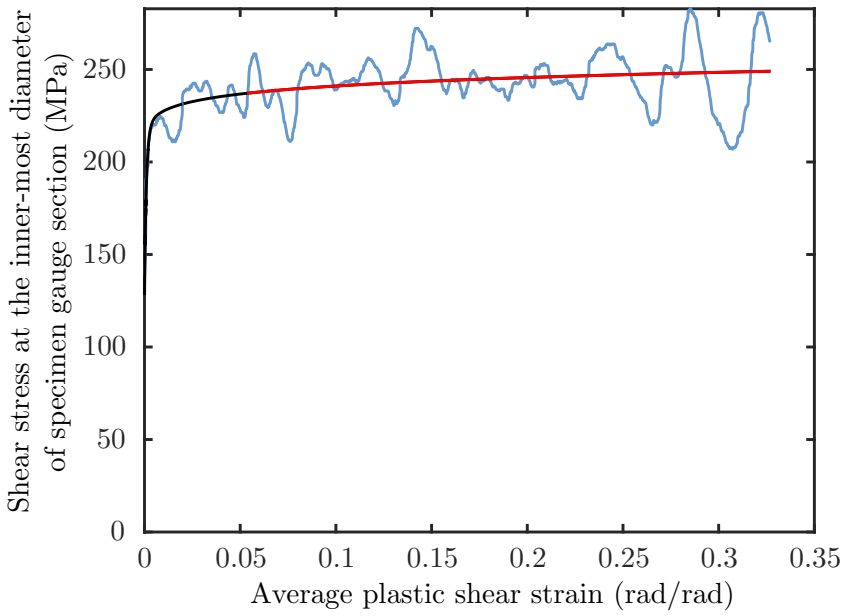

Figure 8.17: Experimental data with regression curve and steady-state flow stress highlighted in red.

Finally, a steady-state flow stress value is found. This is done by firstly calculating the gradient of the regression curve followed by finding the region of the gradient that lies between -0.0001 and 0.0001. The mean of the regression curve that lies within this region is taken as the steady-state flow stress region and is highlighted in red in Figure 8.17.

Chapter 9

Analysis and discussion of experimental results

This chapter discusses the results of the experiments performed during this project. An analysis of the specimen performance is presented. The QST system results are then compared to tensile test results performed on the same material. The TSHB system results are then discussed followed by an analysis of the effect of the specimen gauge section width on the torque equilibrium condition. An analysis of the performance of critical components of the TSHB system is then presented. A strain dependent stress response curve is proposed, and regression of the data from the TSHB tests to this curve are presented. A methodology for determining a steady-state flow stress from each experiment is developed and the strain rate dependence of the material is discussed.

9.1 Specimen analysis

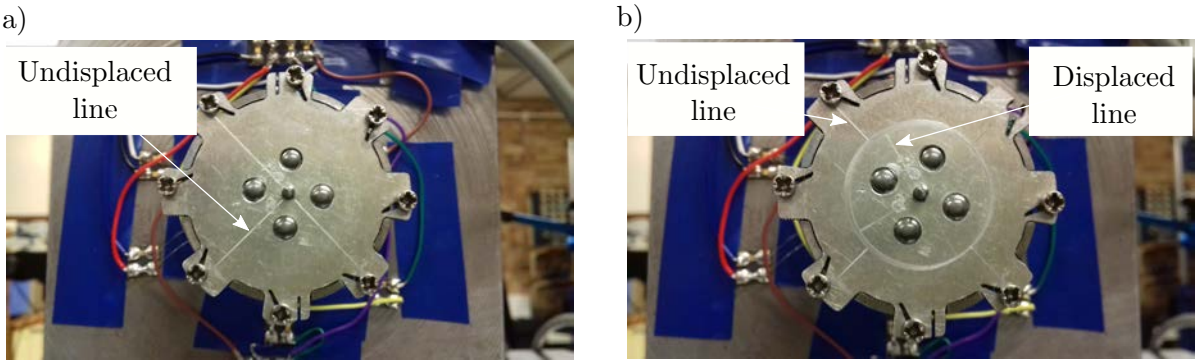

Figure 9.1: Fully mounted specimen for a QST test: (a) undeformed specimen before the test, and (b) deformed specimen after the test.

Figure 9.1 (a) shows a fully mounted specimen for a QST test. The scribed lines and the eight self-tapping screws used to secure the specimen are evident. Figure 9.1 (b) shows a deformed specimen after a QST test. Note the difference between the undisplaced line and the displaced line that clearly indicates deformation in the gauge section of the specimen. Figure 9.2 (a) and 9.2 (b) show the fully mounted specimen and deformed specimen for a TSHB test.

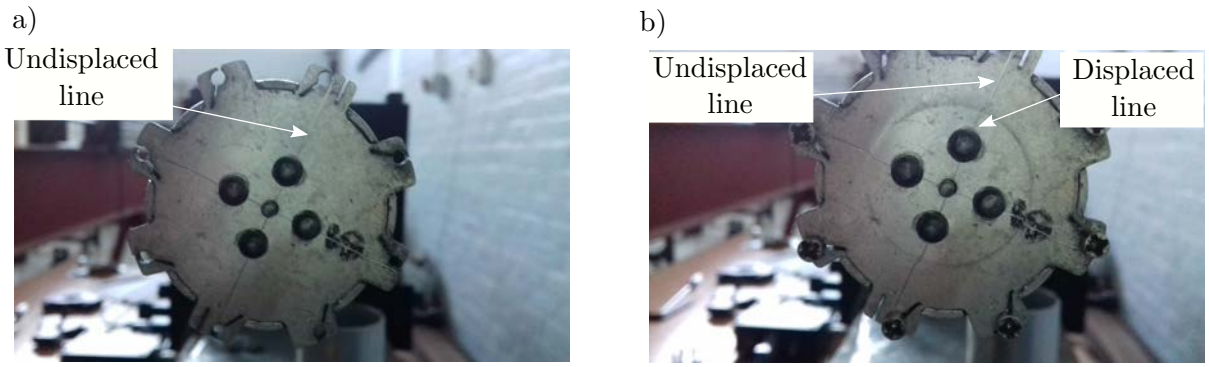

Figure 9.2: Fully mounted specimen for a TSHB test: (a) undeformed specimen before the test, and (b) deformed specimen after the test.

Figure 9.3 shows a portion of two deformed specimens taken with an optical microscope. Figure 9.3 (a) shows a deformed specimen with a near-uniform strain distribution, while Figure 9.3 (b) shows a deformed specimen with a non-uniform strain distribution. It was observed that the smaller the specimen gauge section width, the more uniform the strain distribution across the gauge section was. The usage of average shear strain in the analysis presented in Chapter 8 is most appropriate when the strain distribution across the gauge width is near-contant, thus results from specimens with a narrow gauge width are more precise.

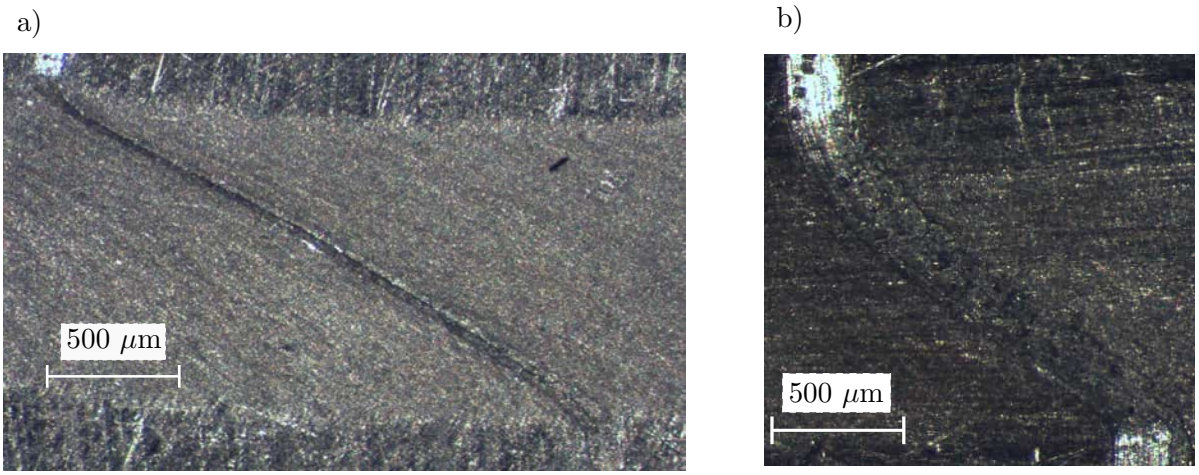

Figure 9.3: Deformed specimen for a QST system test: (a) with a near uniform strain distribution, and (b) with a non-uniform strain distribution.

9.2 Quasi-static tests

In this section, the QST system results are discussed and compared to tensile test results performed on the same material.

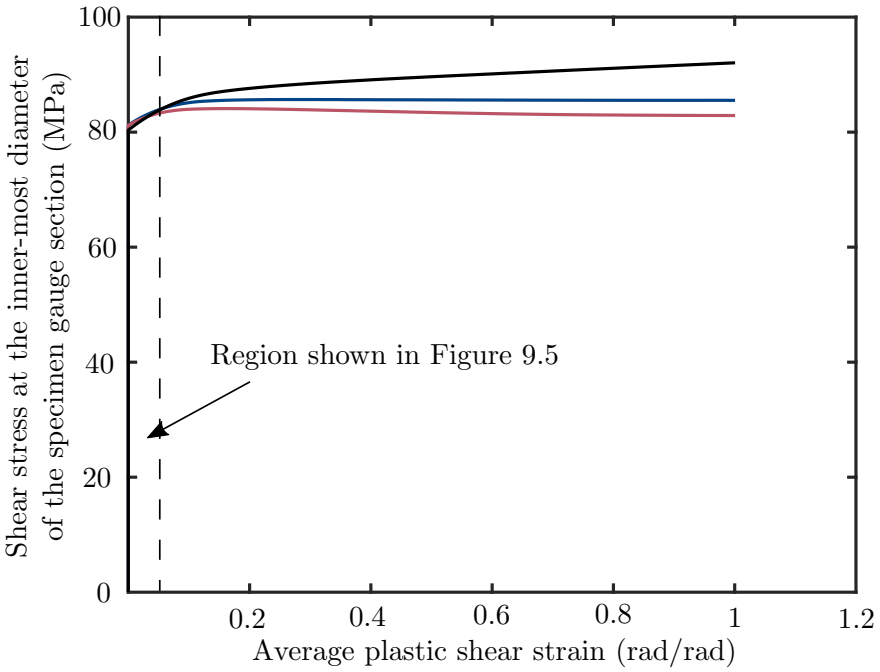

Figure 9.4: Flow curves of three in-plane torsion tests having the same specimen geometry and run at 40 mm/min crosshead speed.

Figure 9.4 shows the results of three in-plane torsion tests where the crosshead speed and dimensions of the specimens were the same. Shear yield stresses were approximately 80 MPa with the plastic strain limited by manual termination of the experiments. For comparison, tensile tests were conducted on rectangular cross-section tensile specimens manufactured from the same material. The tensile specimens were machined at 0 ° and 90 ° relative to the rolling direction of the sheet. The comparison was only possible after converting the shear stress and shear strain to von Mises stress and equivalent average plastic strain. Figure 9.5 shows the comparison and demonstrates the much larger maximum strain possible with the QST test compared to traditional tensile tests which are subject to necking of the gauge section.

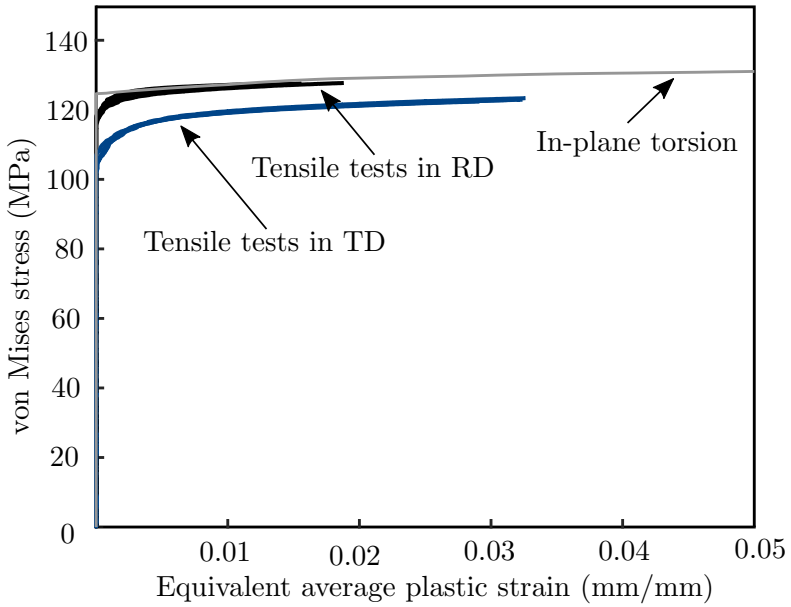

Figure 9.5: Five tensile tests in the rolling direction (RD) and four in the transverse direction (TD) against a single in-plane torsion test to limited strain.

Material anisotropy is clearly visible in the tensile test data. The material behaved in a more ductile manner when loaded in the transverse direction and had a higher strength when loaded in the rolling direction, as indicated in Figure 9.5. The variation in the flow stress corresponding to the loading direction agrees with research done by Allazadeh [49] on the same material. The in-plane torsional test results correspond closely with those of the tensile tests performed in the as-rolled direction of the sheet material, but with much larger total strains achieved. For the conversion of shear stress and shear strain to von Mises stress and equivalent plastic strain, an r_n value of 0.73 for Al 1050 H14 was adopted [50].

9.3 TSHB testing

In this section, the results of the experiments that demonstrated the fastest rise time from the fracture-pin and highest strain rate from the wedge-release clamping mechanisms are compared and discussed.

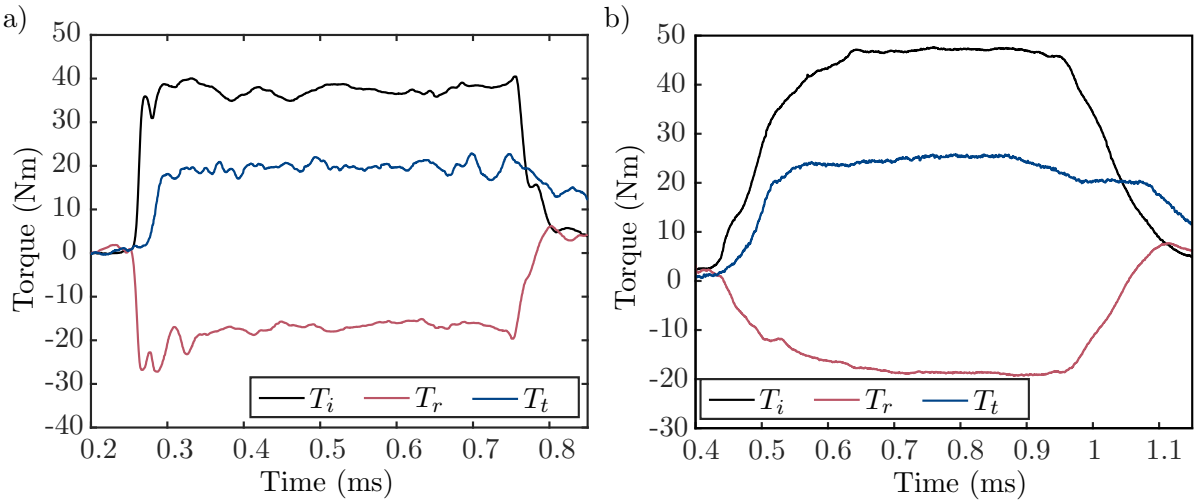

Figure 9.6: Typical incident, reflected and transmitted waves in TSHB testing for: (a) fracture-pin clamping mechanism, and (b) wedge-release clamping mechanism.

In Figure 9.6 the incident, reflected, and transmitted signals for both clamp types are transformed to torque and shifted in time such that they represent the loading at the specimen interfaces. These signals are used to calculate the desired material properties as well as the torque at the two specimen interfaces.

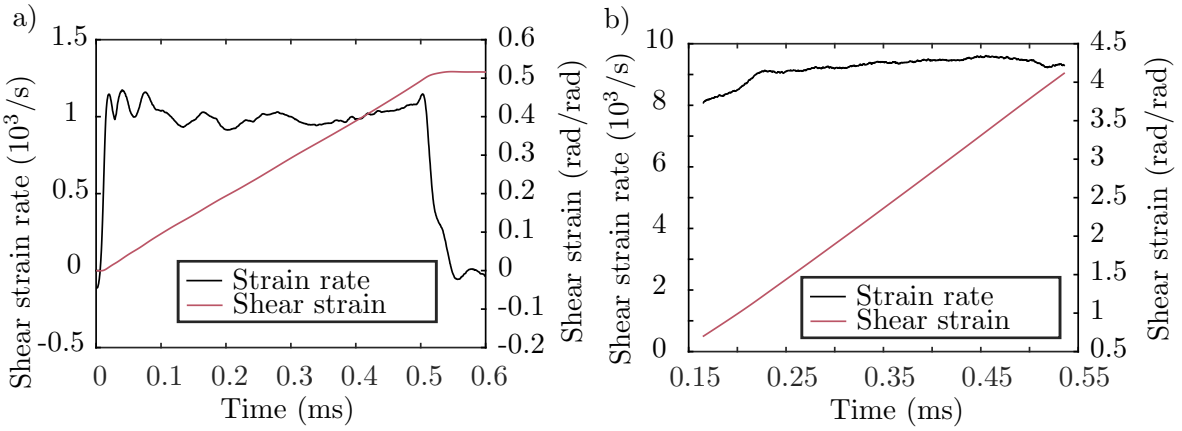

Figure 9.7: Typical shear strain and shear strain rate achieved, as a function of time, for: (a) the fracture-pin clamping mechanism, and (b) the wedge-release clamping mechanism.

The strain rate and strain achieved, as a function of time, are shown in Figure 9.7. The nominal shear strain obtained in Figure 9.7 (a) was approximately 0.52 for an average shear strain rate of 1000 rad/s. The maximum nominal shear strain obtained for an average nominal shear strain rate of 9000 rad/s was approximately 4, as shown in Figure 9.7 (b). Generally, the strain rate over each experiment's duration was constant. The maximum shear strain rate was limited by the clamping force provided by the clamping mechanisms. When increased loading was attempted, slipping of the bar within the clamps was experienced. The limiting torque based on the material strength of the incident bar is approximately 300 Nm, indicating an increase in load is possible if slipping at the clamps was delayed.

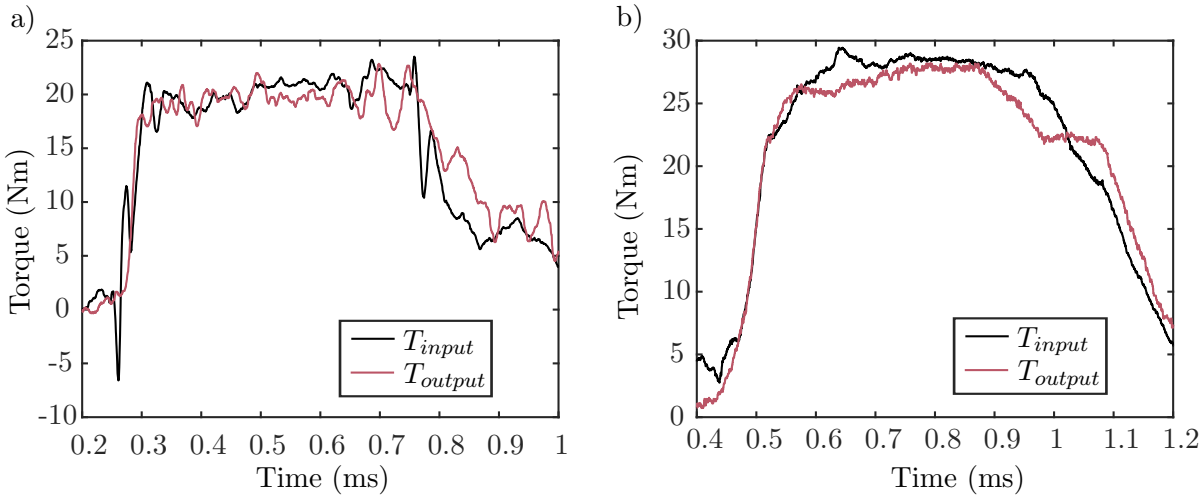

Figure 9.8: Typical torque equilibrium profile at the specimen interface for: (a) fracture-pin clamping mechanism, and (b) wedge-release clamping mechanism.

The elementary equations used in the TSHB experiments assume that torque equilibrium is established in the specimen. When low impedance materials are used, as is the case in this dissertation, it may take several stress wave reflections within the specimen for the stress wave to "ring-up" to a state of torque equilibrium. This is attributed to the slow wave speeds in the material where the wave has to travel back and forth several times in the specimen. Figure 9.8 shows a comparison of the torque at the specimen interfaces. Comparison of the input and output torque acting on the specimen shows that the specimen achieves quasi-equilibrium for both clamp types.

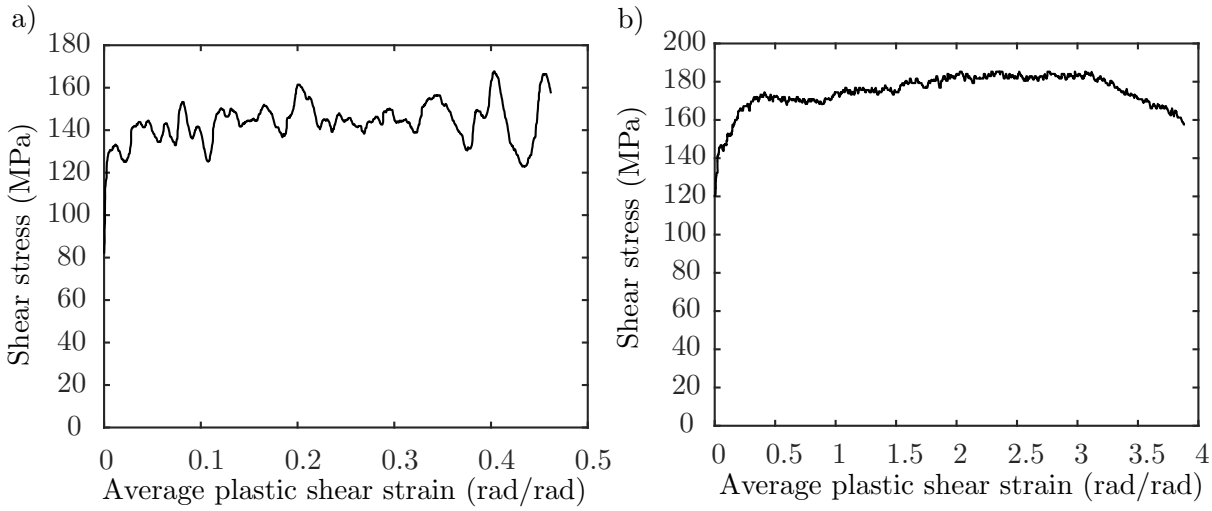

Figure 9.9: Shear stress vs average plastic shear strain at the inner-most diameter of the specimen gauge section for: (a) the fracture-pin clamping mechanism, and (b) the wedge-release clamping mechanism.

The shear stress against average plastic shear strain at the inner-most radius of the specimen gauge section is shown in Figure 9.9 . Steady-state flow stresses were approximately 180 MPa at the higher dynamic strain rates, as shown in Figure 9.9 (b), and 140 MPa at the lower dynamic strain rates, as shown in Figure 9.9 (a). Strain rate dependance is further discussed later in this chapter.

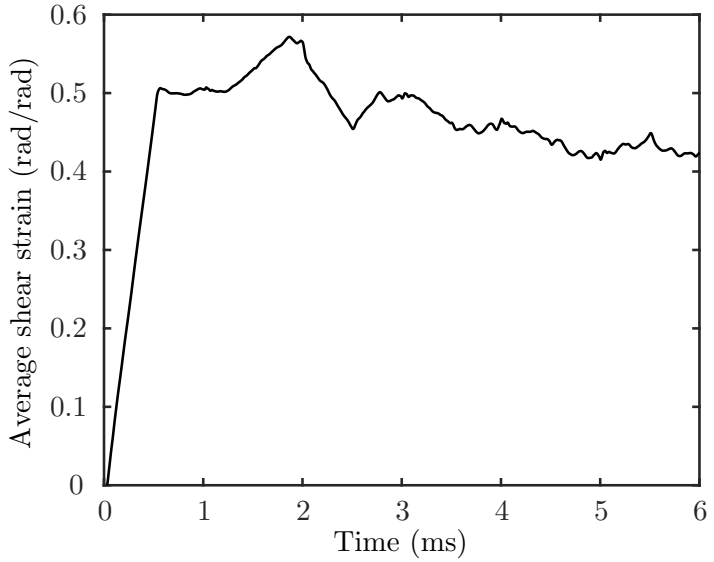

Figure 9.10: Typical reconstructed strain profile against time.

A wave separation technique was adopted to investigate the average strain across the gauge section during TSHB tests. The technique is discussed in detail in Appendix F. The reconstructed time history of the strain is shown in Figure 9.10. It can be observed that there is some strain reversal in the specimen after its initial loading.

9.4 Effect of gauge width on torque equilibrium

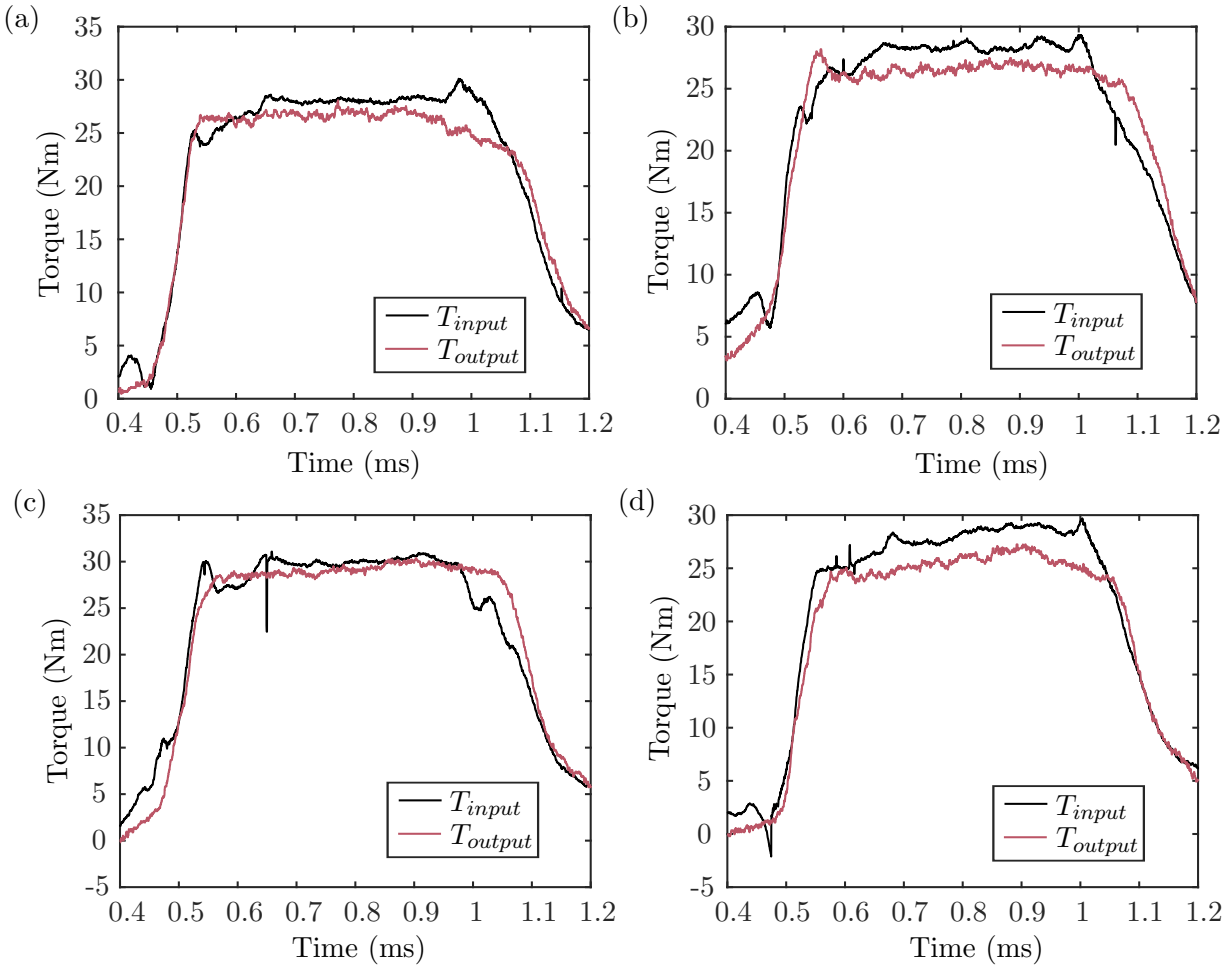

Figure 9.11: Torque equilibrium at the specimen interface: (a) 2 mm, (b) 1 mm, (c) 0.8 mm, and (d) 0.5 mm.

The effect of the specimen gauge section width on the torque equilibrium condition is examined in Figure 9.11. The specimen gauge section widths were 2 mm, 1 mm, 0.8 mm, and 0.5 mm and correspond to (a) to (d) in Figure 9.11. Design calculations indicate that quasi-equilibrium should be obtained for specimen gauge widths less than 6 mm. The figures indicate similar results for the various gauge section widths, therefore the design has been successful in achieving torque equilibrium.

9.5 Load-application mechanism performance

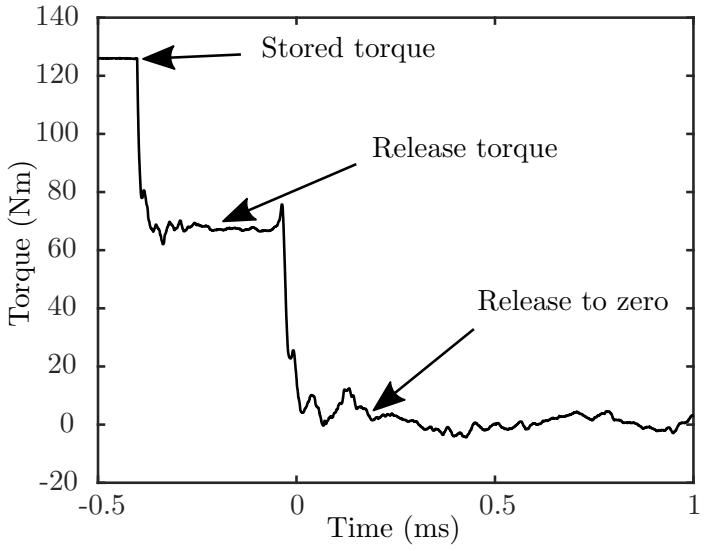

Figure 9.12: Strain gauge measured wave used to analyse loaded torque in the stored torque TSHB test.

The signal used to analyse the performance of the load-application mechanism used in the TSHB tests is shown in Figure 9.12. For the example shown, a loading torque of approximately 130 Nm was stored in the incident bar. Upon release of the clamping mechanism, the torque value drops down to approximately 65 Nm due to the release wave. Once the reflected wave returns to the strain gauge, the torque releases to zero. This is indicated on the curve where the measured torque drops to approximately 0 Nm. The load-application mechanism does not offer a true constant-displacement boundary condition since small loadings of the loading end may be possible and could account for the disturbances seen in the signal. The measured response matches that predicted by the Lagrangian diagram presented in Figure 3.3 in Chapter 3.

9.6 Clamping mechanism performance

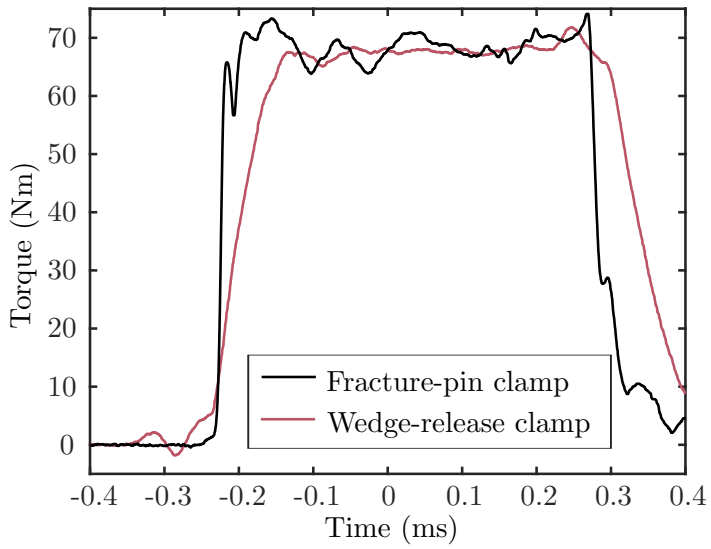

Figure 9.13: Comparison of the incident waves generated by the two clamping mechanisms used for TSHB tests.

A comparison of incident waves generated by the two clamping mechanisms is shown in Figure 9.13. The fracture-pin clamp has consistent rise times of approximately 20 μs and a consistent release. However, the incident wave oscillates significantly (approximately 20% of the overall wave) and care must thus be taken in interpreting the results. The wedge-release clamping mechanism has consistent rise times of approximately 60 μs. The longer rise time results in shorter constant-torque durations and therefore smaller strains being achieved.

The incident waves generated by both clamping mechanisms are useful for material characterisation. For testing where there is a requirement to reach a constant strain rate as soon as possible (having a low rise time), for example in the investigation of adiabatic shear bands, the fracture-pin clamping mechanism can be used. Where a more gradual rise is required along with a constant strain rate region with no high frequency oscillations, for example when testing low impedance materials, then the wedge-release clamping mechanism can be used.

9.7 Manufacturing method

The manufacturing process for machining of the specimen gauge section may significantly influence the fracture strain. Figure 9.14 shows a number of microscope images illustrating the machined surfaces of the specimen gauge section. Milling traces are evident in the radial direction. A number of defects are also observed which may be caused by the feed speed and chip removal of the milling tool. Defects across the specimen gauge section may initiate shear localization at high strain rates. Despite these imperfections, the repeatability of the results indicates their effect was small. However, a more detailed analysis across a large sample size may be warranted in the future. For example, control of depth may be particularly significant as small errors in the value for specimen gauge section thickness results in errors in the shear stress calculation.

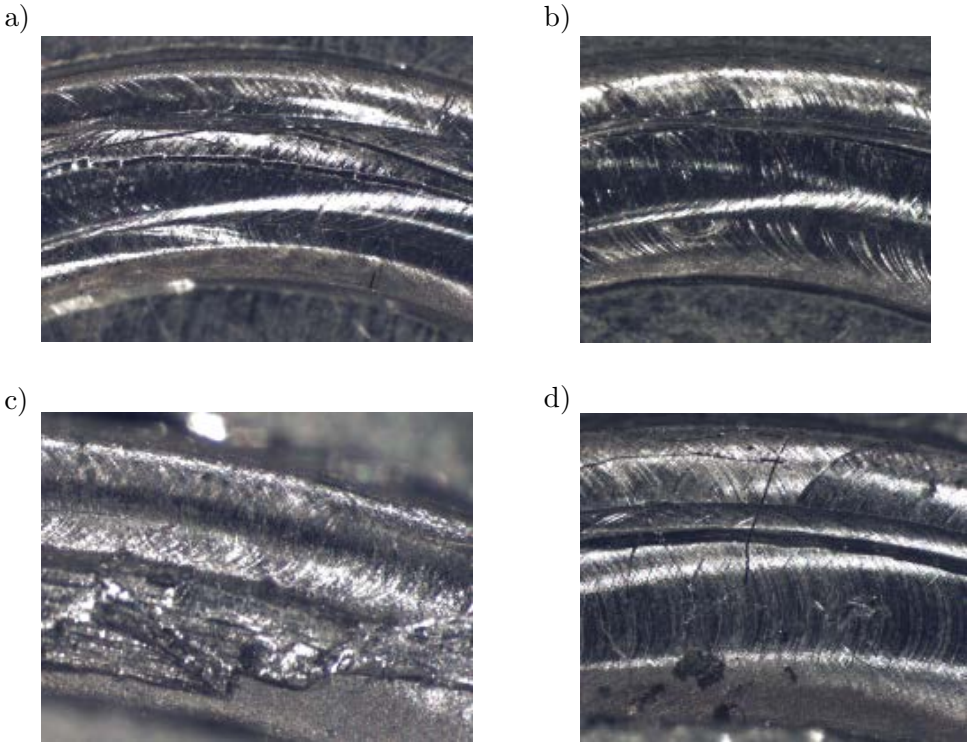

Figure 9.14: Examples of machining surfaces of gauge section for the annular in-plane torsional specimen.

9.8 Strain measurement

For small gauge section widths the strain appears uniform across the width and computing the average width using the dimensions of the gauge section is appropriate. For larger widths there is radial variation in the strain. This is especially notable in high strain rate tests with wide gauge sections, where the deformation appears to have localised near the inner portion of the gauge. Figure 9.15 shows microscope images of deformed specimens for various machined gauge section widths. It can be observed that the difference between the measured gauge section width and the apparent gauge section width becomes more prominent with increasing gauge section width. The apparent gauge section width has its inner edge at the inner-most diameter and its outer edge at the diameter where the strain field visually ends (based on the displaced line and the undisplaced line in the microscope image). Thus, the challenge of exact strain measurement increases with an increase in gauge section width.

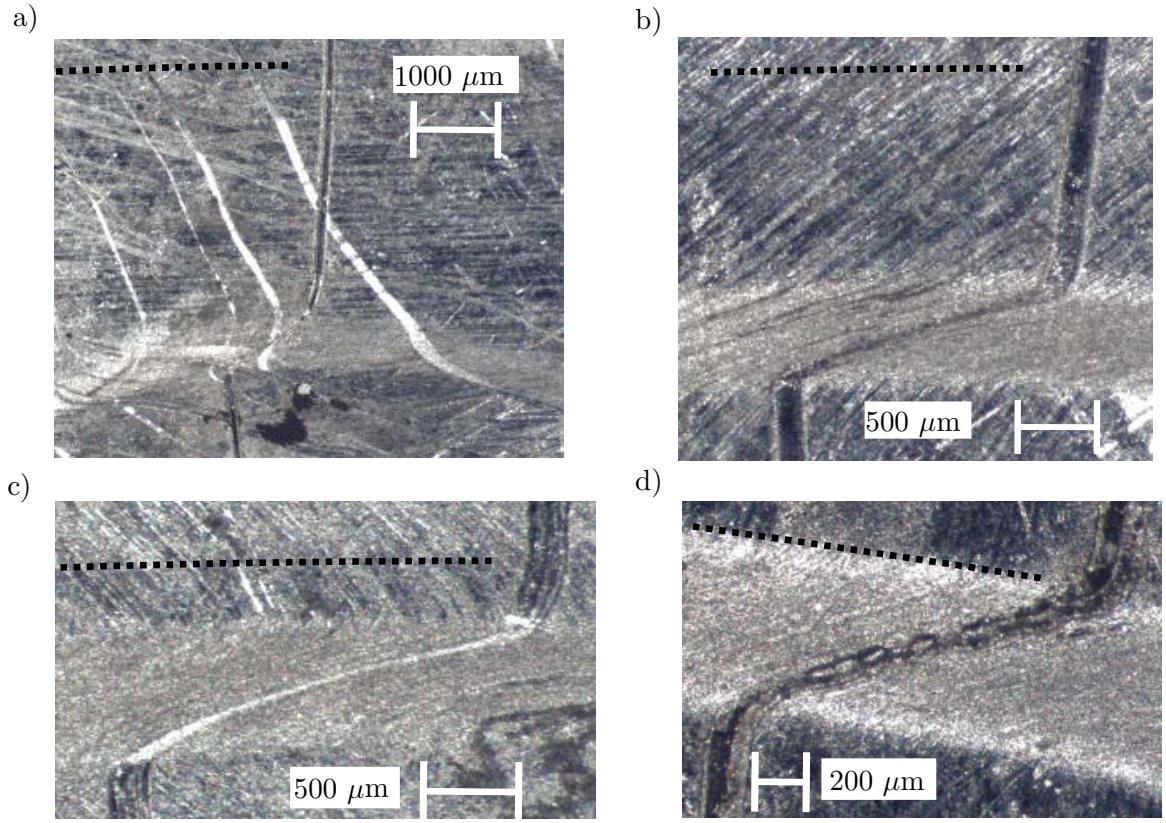

Figure 9.15: Microscope images of deformed specimen gauge section for TSHB tests: (a) 4 mm, (b) 2 mm, (c) 0.8 mm, and (d) 0.5 mm. The approximate outer edge of the measured gauge section width is highlighted by the dotted line on each image.

Where uniform strain fields are required it is clear that a narrow gauge width should be used. However, wider width gauge sections may be useful in the investigation of shear localisation, with the radius of apparent shear strain being a possible metric with which to evaluate the accuracy of numerical simulations.

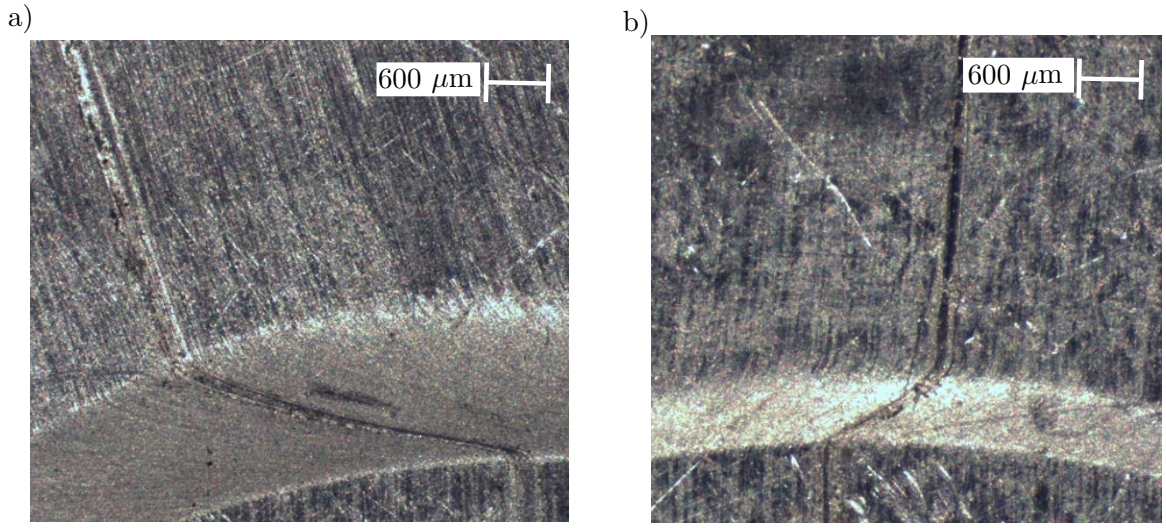

Figure 9.16: Microscope images of a deformed specimen having a measured gauge section width of 4 mm for: (a) QST test, and (b) TSHB test.

Figure 9.16 shows a comparison of a deformed specimen having a gauge section width of 4 mm for a QST and TSHB test. The deformation in the TSHB test appears to have occured over a smaller gauge width than that in the QST test. In the TSHB test, the apparent gague section width was taken as 0.6 while for the QST test, the apparent gauge section width was taken as 1.2.

The in-plane torsion test achieves true strains beyond 1 for sheet metals. However, the primary method adopted for measuring these large strains may require further investigation as to its effectiveness. The method adopted is an indirect determination of shear strain from the measured torque and the angle of rotation of the input bar. The primary method is confirmed using the secondary method, shown in Figure 9.17, which is a direct strain measurement determined locally as a function of the radius. The secondary method makes use of the marked lines on the specimen to directly measure the final shear angle for shear strain calculation. The determination can, however, only be done at the end of the in-plane torsion test.

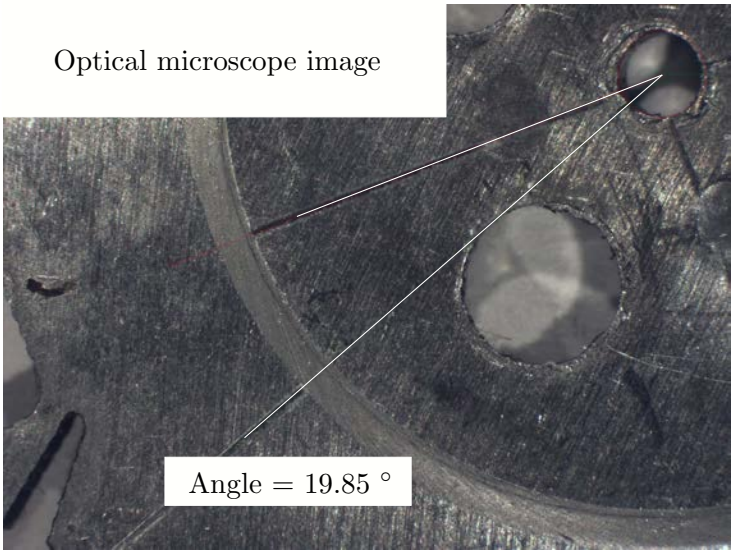

Figure 9.17: Secondary (direct) method for examination of the angle of rotation.

The challenge of exact strain measurement increases with an increase in strain. Adopting DIC for measuring these large strains may not be a suitable alternative either. DIC requires multiple reapplications of the DIC pattern on the specimen due to the large strains. This leads to an extending of the required time for experimentation. The facet size of the DIC may also have to be considered due to the narrow gauge sections. It may be possible to write custom machine vision software (for instance with coloured lines on the specimens) thus producing a customised DIC solution that can be synchronised with the other data captured.

9.9 Regression curve

The equation

$$\sigma = A + B(1 - e^{n\varepsilon}) + C(1 - e^{D\varepsilon}) \tag{9.1}$$

is proposed as a relationship between strain and von Mises stress. The first exponential term accounts for the early yield behaviour and the second exponential term accounts for the more gradual increase of the von Mises stress which asymptotes to a constant value. The equation has been proposed as the experimental results show early behaviour followed by more gradual kinematic hardening behaviour. The first term in the equation captures the approximate yield

stress value. A steady-state flow stress was identified in each test and used to compare all the experimental data. This can be done since TSHB tests allow for an extended strain history and consequenty an extended plateau region which conventional SHPB tests do not achieve due to necking of the gauge section. Examples of the fitted curves are shown in Figure 9.18 and 9.19. Strain rate effects are apparent in these figures. Further examples are shown in Appendix F.

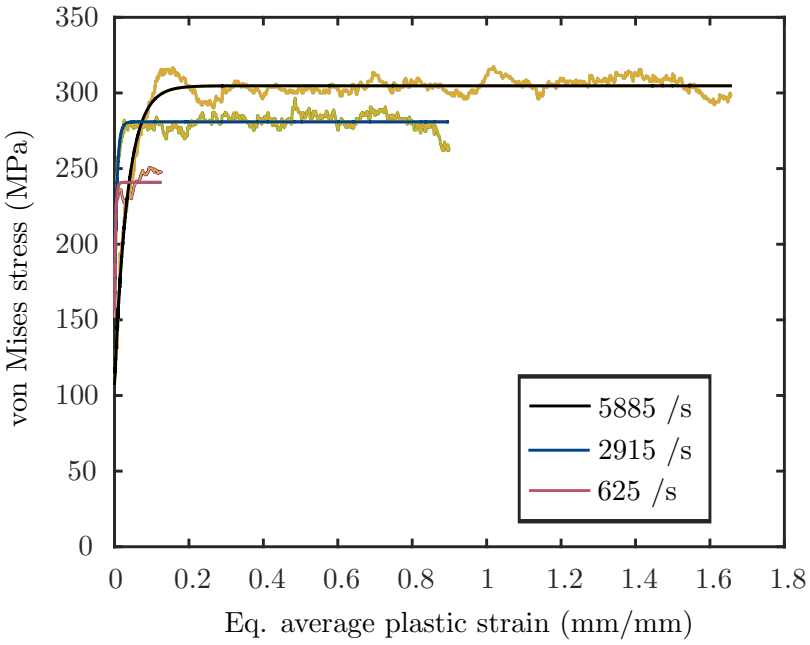

Figure 9.18: Three examples of the comparison of the experimental data and the regression curve.

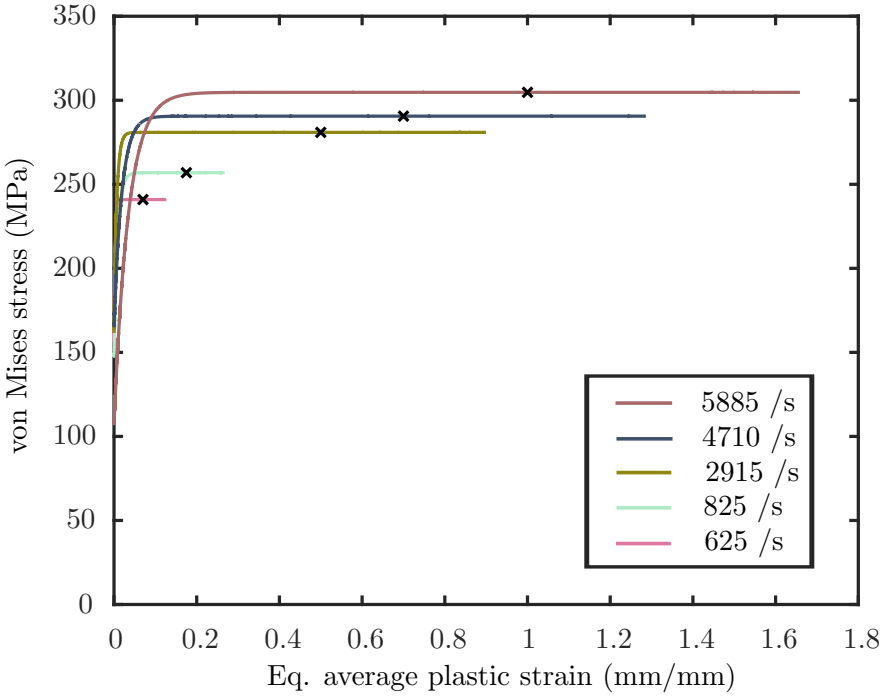

Figure 9.19: Five regression curves with the steady-state flow stress value marked with an x.

9.10 Steady-state flow stress

Using all the torsional experimental data, a relationship between steady-state flow stress and strain rate is proposed. The relationship can be described by a logarithmic term and a power law term. The function used to describe this relationship is

$$\sigma_{pl} = \overline{\sigma}_{pl} + A.\ln(\dot{\varepsilon}) + B\dot{\varepsilon}^{k} \quad . \tag{9.2}$$

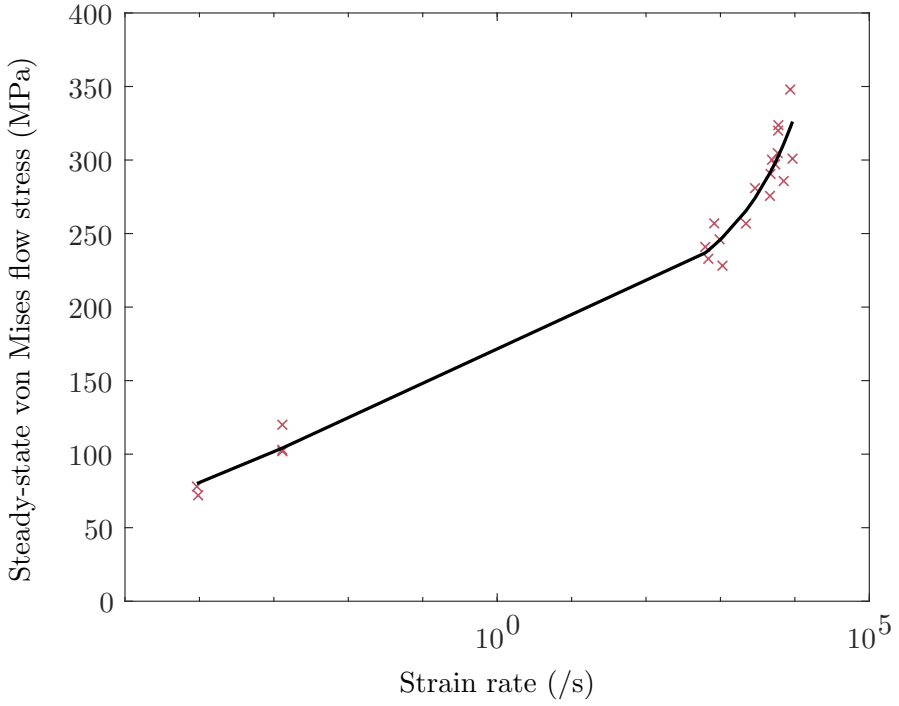

Figure 9.20: The effect of strain rate on steady-state flow stress where the measured gauge section width is used for strain rate calculation.

Figure 9.20 shows the steady-state flow stress taken from the experimental data plotted against the logarithmic strain rate where the strain rate is calculated using the measured gauge section width. Figure 9.21 shows the steady-state flow stress taken from the experimental data plotted against the logarithmic strain rate where the strain rate is calculated using the apparent gauge section width. Both figures show that the effect of strain rate on the steady-state flow stress is greater as the strain rate increases in the dynamic regime. When using the strain rate based on the apparent gauge width, a steeper exponential curve is observed.

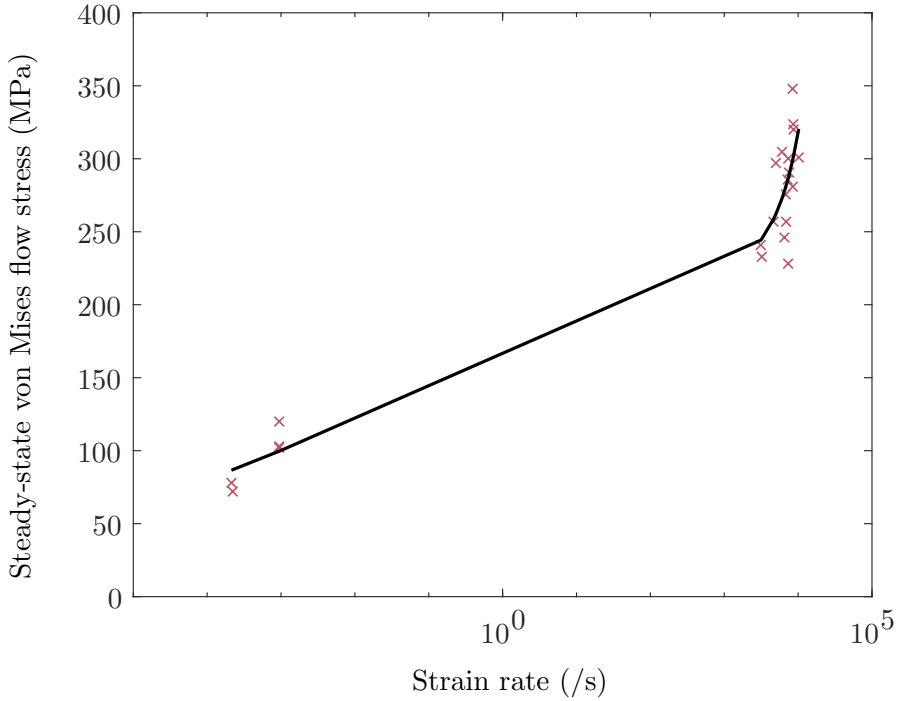

Figure 9.21: The effect of strain rate on steady-state flow stress where the apparent gauge section width is used for strain rate calculation.

The final values for the constants are given in Table 9.1. Based on Figure 9.20, the results indicate a steady-state flow stress of approximately 70 MPa in the 10^{-4} /s range that increases to approximately 100 MPa in the 10^{-3} /s range. In the dynamic range, the steady-state flow stress is approximately 250 MPa in the 10^{3} /s range and increases to approximately 350 MPa in the 10^{4} /s range. The comparison makes evident the strain rate sensitivity of Al 1050 H14.

Table 9.1: The constants used for the rate dependency function and the goodness of fit measure R^2.

Figure	$\overline{\sigma}_{pl}$	A	B	k	R^2
3	164.75	9.12	0.20	0.65	0.97
4	160.52	8.74	7.46×10^{-5}	1.50	0.92

Due to the lack of experimental data in intermediate strain rate regime along with inaccuracies in the acquired experimental data, the results are tentative but promising. More experimental data is therefore required to build a more accurate representation of the material behavior.

Chapter 10

Conclusions and Recommendations

10.1 Conclusions

The design, fabrication, calibration and testing of the modified in-plane torsion specimen and the two novel testing techniques was successfully completed. During the design phase, detailed design specifications were written and design drawings developed. Final designs were selected followed by the fabrication process and the assembly of the two systems. The systems were carefully calibrated and comprehensively tested. The techniques were developed to test materials over a large range of strain rates. The results show good repeatability and are consistent with existing results published in literature.

The novel quasi-static torsional system produced accurate repeatable results and has a strain rate capability from 10^{-5} /s to 10^{-2} /s while the novel torsional split Hopkinson bar (TSHB) system was used to produce accurate repeatable results for dynamic strain rates and has a strain rate capability from 10^{2} /s and 10^{4} /s. The TSHB system utilised a long incident bar and shorter transmission tube with the tube selected to enhance the transmission signal. Prior to the analysis of the TSHB test data, the assumption of stress equilibrium was checked and regarded as valid. Additionally, the TSHB tests were found to achieve a near-constant strain rate for each test with very lengthy "plateau regions" observed for most tests. The load-application mechanism was successful in generating the desired torsional wave in the incident bar. A wave separation technique was adopted which allowed for the measurement of large strains without the need for impractical long bars. A regression analysis was performed to extract the parameters for the adopted constitutive equation which was found to best describe the experimental data obtained from a TSHB test. Careful measurement of the geometry of the specimen dimensions was required to minimise errors in the obtained material properties.

The quasi-static and dynamic shear properties of Al 1050 H14 were investigated. An experimentally determined relationship between strain rate and steady state flow stress was found. The relationship could be best described by a combination of a logarithmic and a power law, with steady-state flow stress increasing with strain rate. Furthermore, uniaxial tensile test results indicated more ductile behaviour in the transverse direction and higher strength in the rolling direction, thus verifying the anisotropic material properties of the material. The in-plane torsional test results correspond closely with those of the tensile tests performed in the as-rolled direction of the sheet material, but with much larger total strains achieved.

10.2 Recommendations

Though the aims of the dissertation were met and the effect of strain rate on the material was identified and characterised, there are several aspects which could warrant further work. The following recommendations are proposed in order to produce more reliable results:

- The wave velocity of the bars should be accurately determined in order to produce more reliable results. More emphasis needs to be placed on finding the starting point of the actual experimental signals. This procedure is particularly important in the determination of torque equilibrium.
- A strain gauge for bending measurement may assist in determining how well aligned the system is.
- The current QST system has test capabilities in the range from 10^{-5}/s to 10^{-2}/s while the TSHB system has capabilities in the range from 10^{2}/s to 10^{4}/s. To develop a material model valid over the full strain rate range, a system that can test in the intermediate strain rate regime (10^{-}/s to 10^{2}/s) should be developed.
- Strain rate sensitive and insensitive materials should be tested. Characteristics of the systems that may be obscured when testing rate sensitive materials might become apparent when testing rate insensitive materials.
- A large number of characterization tests done on many materials at differing strain rates will allow for nuanced understanding of the testing systems. For instance, it may be possible to develop a set of criteria for distinguishing effects intrinsic to the material being tested from those caused by the machines.
- Numerical simulation of material behaviour, for instance with finite element analysis, can be used to investigate differing material models and their effects on the radial strain distributions achieved.

The potential for future material characterisation is large. It is anticipated that the systems developed will form a core part of the equipment used for material characterisation at BISRU.

Bibliography

[1] ASM International. Handbook Committee. *ASM handbook: mechanical testing and evaluation*, volume 8. ASM International, 2000.

[2] T Nicholas. Strain-rate and strain-rate-history effects in several metals in torsion. *Experimental Mechanics*, 11(5):370–374, 1971.

[3] RJ Caspar. Experimental and numerical study of shear localization as an initiation mechanism in energetic solids. Master's thesis, University of Notre Dame Graduate School, 1996.

[4] Q Yin, C Soyarslan, K Isik, and AE Tekkaya. A grooved in-plane torsion test for the investigation of shear fracture in sheet materials. *International Journal of Solids and Structures*, 66:121–132, 2015.

[5] X Yu, L Chen, Q Fang, X Jiang, and Y Zhou. A review of the torsional split hopkinson bar. *Advances in Civil Engineering*, 2018, 2018.

[6] K Miyauchi. A proposal for a planar simple shear test in sheet metals. *Sci. Pap. Inst. Phys. Chem. Res.(Jpn).*, 78(3):27–40, 1984.

[7] YG An, H Vegter, and J Heijne. Development of simple shear test for the measurement of work hardening. *Journal of Materials Processing Technology*, 209(9):4248–4254, 2009.

[8] Q Yin, B Zillmann, S Suttner, G Gerstein, M Biasutti, AE Tekkaya, MF-X Wagner, M Merklein, M Schaper, T Halle, et al. An experimental and numerical investigation of different shear test configurations for sheet metal characterization. *International Journal of Solids and Structures*, 51(5):1066–1074, 2014.

[9] AE Tekkaya, K Pöhlandt, and K Lange. Determining stress-strain curves of sheet metal in the plane torsion test. *CIRP Annals*, 31(1):171–174, 1982.

[10] A Brosius, Q Yin, A Güner, and AE Tekkaya. A new shear test for sheet metal characterization. *Steel Research International*, 82(4):323–328, 2011.

[11] WE Baker and CH Yew. Strain-rate effects in the propagation of torsional plastic waves. 1966.

[12] RS Culver. Torsional-impact apparatus. *Experimental Mechanics*, 12(9):398–405, 1972.

[13] M Peroni and G Solomos. Advanced experimental data processing for the identification of thermal and strain-rate sensitivity of a nuclear steel. *Journal of Dynamic Behavior of Materials*, 5(3):251–265, 2019.

[14] BG Prusty and A Banerjee. Structure–property correlation and constitutive description of structural steels during hot working and strain rate deformation. *Materials*, 13(3):556, 2020.

[15] M Jutras. Improvement of the characterisation method of the johnson-cook model. 2008.

[16] W Lee and C Liu. The effects of temperature and strain rate on the dynamic flow behaviour of different steels. *Materials Science and Engineering: A*, 426(1-2):101–113, 2006.

[17] GH Majzoobi, F Freshteh-Saniee, SFZ Khosroshahi, and HB Mohammadloo. Determination of materials parameters under dynamic loading. part i: Experiments and simulations. *Computational Materials Science*, 49(2):192–200, 2010.

[18] R Song and Q Dai. Dynamic deformation behavior of dual phase ferritic-martensitic steel at strain rates from 10^-4 to 2000 s^{-1}. *Journal of Iron and Steel Research International*, 20(8):48–53, 2013.

[19] H Noh, W An, H Park, B Kang, and J Kim. Verification of dynamic flow stress obtained using split hopkinson pressure test bar with high-speed forming process. *The International Journal of Advanced Manufacturing Technology*, 91(1-4):629–640, 2017.

[20] CH Guo, XH Shen, FC Jiang, and GP Zou. Effect of stress wave dispersion on hopkinson pressure bar loaded fracture test. In *Key Engineering Materials*, volume 577, pages 569–572. Trans Tech Publ, 2014.

[21] WN Sharpe. *Springer handbook of experimental solid mechanics*. Springer Science & Business Media, 2008.

[22] SS Rao. *Vibration of continuous systems*. John Wiley & Sons, 2019.

[23] TD Rossing and DA Russell. Laboratory observation of elastic waves in solids. *American Journal of Physics*, 58(12):1153–1162, 1990.

[24] DJ Parry, PR Dixon, S Hodson, and N Al-Maliky. Stress equilibrium effects within hopkinson bar specimens. *Le Journal de Physique IV*, 4(C8):C8–107, 1994.

[25] G NICOLAESCU, G Stefan, C Enache, and MV Cârmaci. Torsional testing at high strain rates using a kolsky bar. *Land Forces Academy Review*, 20(2):233, 2015.

[26] G Owolabi, D Odoh, A Peterson, A Odeshi, and H Whitworth. Measurement of the deformation of aluminum alloys under high strain rates using high speed digital cameras. *World Journal of Mechanics*, 3(02):112, 2013.

[27] JL Lewis and JD Campbell. The development and use of a torsional hopkinson-bar apparatus. *Experimental Mechanics*, 12(11):520–524, 1972.

[28] GH Staab and A Gilat. A direct-tension split hopkinson bar for high strain-rate testing. *Experimental mechanics*, 31(3):232–235, 1991.

[29] J Duffy, JD Campbell, and RH Hawley. On the use of a torsional split hopkinson bar to study rate effects in 1100-0 aluminum. *Journal of Applied Mechanics*, 38(1):83–91, 1971.

[30] X Nie, R Prabhu, WW Chen, JM Caruthers, and T Weerasooriya. A kolsky torsion bar technique for characterization of dynamic shear response of soft materials. *Experimental mechanics*, 51(9):1527–1534, 2011.

[31] BJ Claus, X Nie, BE Martin, and W Chen. A side-impact torsion kolsky bar. *Experimental Mechanics*, 55(7):1367–1374, 2015.

[32] X Jiang, Y Xiao, L Chen, Qin Fang, and Y Zhou. An electromagnetic driven torsional split hopkinson bar. In *Proceedings of 2nd International Conference on Impact Loading of Structures and Materials*, pages 103–105.

[33] M Osman. Analysis and characterisation of existent quick release mechanism for torsional split-hopkinson bar testing, 2017 (BSc dissertation (UCT)).

[34] L Nake. Design,manufacture and characterisation of a quick release mechanism, 2011 (BSc dissertation (UCT)).

[35] M Purnell. Design,manufacture and characterisation of a fracture pin quick release mechanism, 2013 (BSc dissertation (UCT)).

[36] A Gilat and YH Pao. High-rate decremental-strain-rate test. *Experimental mechanics*, 28(3):322–325, 1988.

[37] KA Gardner. *Experimental techniques for shear testing of thin sheet metals and compression testing at intermediate strain rates*. PhD thesis, The Ohio State University, 2013.

[38] Technifast. *Standard Dowel Pins: Solid and extractable dowel pins in metric and imperial sizes*, 2020 Accessed: 2020-01-20.

[39] The Engineering ToolBox. *Factors of Safety - FOS - are important in engineering designs.*, 2022 Accessed: 2022-01-23.

[40] Aalco. *Aluminium Alloy-Commercial Alloy-1050A H14 Sheet*, 2020 Accessed: 2020-01-20.

[41] MIT. *Defining plasticity in Abaqus*, 2021 Accessed: 2021-02-02.

[42] BM Hance. Influence of discontinuous yielding on normal anisotropy (r-value) measurements. *Journal of materials engineering and performance*, 14(5):616–622, 2005.

[43] H Traphöner, S Heibel, T Clausmeyer, and AE Tekkaya. Influence of manufacturing processes on material characterization with the grooved in-plane torsion test. *International Journal of Mechanical Sciences*, 146:544–555, 2018.

[44] Q Yin, AE Tekkaya, and H Traphöner. Determining cyclic flow curves using the in-plane torsion test. *CIRP Annals*, 64(1):261–264, 2015.

[45] MATLAB and Simulink MathWorks. *Filtering and Smoothing Data*, 2020 Accessed: 2021-05-20.

[46] MATLAB and Simulink MathWorks. *medfilt2*, 2021 Accessed: 2021-08-12.

[47] MATLAB and Simulink MathWorks. *cumtrapz*, 2021 Accessed: 2021-08-12.

[48] I Oliveira, P Teixeira, F Ferreira, and A Reis. Inverse characterization of material constitutive parameters for dynamic applications. *Procedia Engineering*, 114:784–791, 2015.

[49] M Allazadeh. Analysing the effect of strain rate and temperature on the flow stress in aa1050 sheet using e-2448 standard. *Journal of Multidisciplinary Engineering Science and Technology*, 5(11):9009–9015, 2018.

[50] S Sharma, RP Singh, and S Kumar. Mechanical anisotropy of aluminium aa1050 and aluminium alloy aa6016 produced by accumulative roll bonding. *Int. J. Innov. Eng. Technol.*, 7:350–356, 2016.

[51] CD Wilson and MW Renfro. Shaft deflection—a very, very long example. 2013.

[52] SW Park and M Zhou. Separation of elastic waves in split hopkinson bars using one-point strain measurements. *Experimental Mechanics*, 39(4):287–294, 1999.

Appendices

Appendix A

Specimen dimension variables

This appendix documents the equations used to calculate the critical specimen variables.

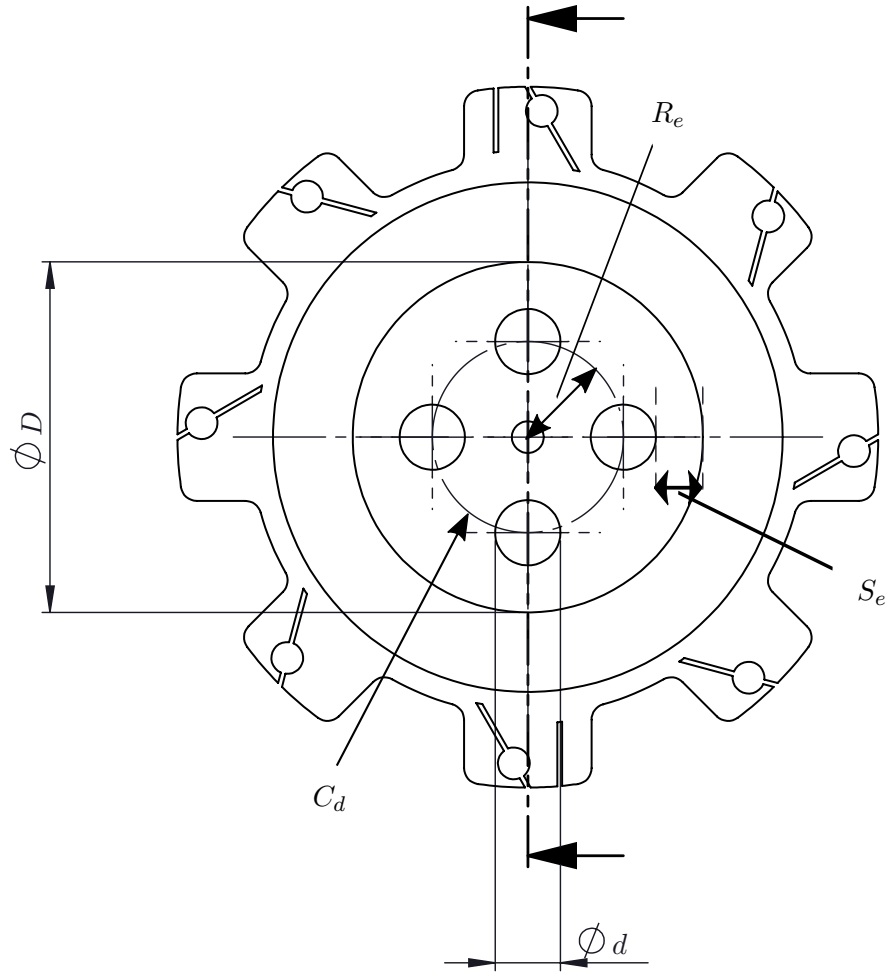

Figure A.1: Specimen dimension variables.

Figure A.1 shows some important specimen dimension variables. The effective radius, R_e, can be calculated using

$$R_e = \frac{D_i}{2} - S_e - \frac{d}{2} \tag{A.1}$$

where D_i is the diameter of the input bar, S_e is the edge spacing and d is the diameter of the

pin hole. The effective force, F_e can be calculated using

$$F_e = T_d/R_e \tag{A.2}$$

where T_d is the design torque. The effective circumference, C_d can be calculated using

$$C_d = 2\pi R_e \quad . \tag{A.3}$$

The effective force per pin F_p can be calculated using

$$F_p = F_e/N \tag{A.4}$$

where N is the number of pin holes. Lastly, the pin spacing, S_p can be calculated using

$$S_p = (C_d - dN)/N \quad . \tag{A.5}$$

Appendix B

Specimen width calculation

This appendix documents the technique adopted for the measurement of the specimen gauge section width. The process of measuring the specimen gauge section width is more challenging than the measurement of the specimen gauge section thickness thus requires further elaboration.

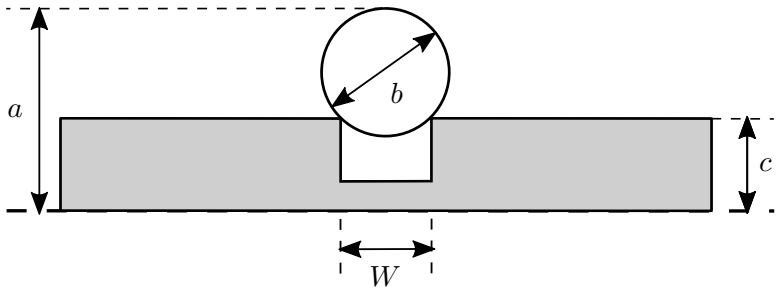

Figure B.1: Bearing ball measuring technique variables for specimen gauge section width.

Figure B.1 shows the three measurements required to infer the specimen gauge section width. The reverse face of the specimen should be placed on a metrology table. a is the vertical distance between the top of the bearing ball and the bottom of the specimen, b is the ball bearing diameter and c is the overall thickness of the specimen. The equations used to infer the specimen gauge section width are shown below. When the bearing ball is positioned as shown in Figure B.1, the height difference between the top of the specimen and the bottom of the bearing ball, d, can be calculated using

$$b - (a - c) = d \quad . \tag{B.1}$$

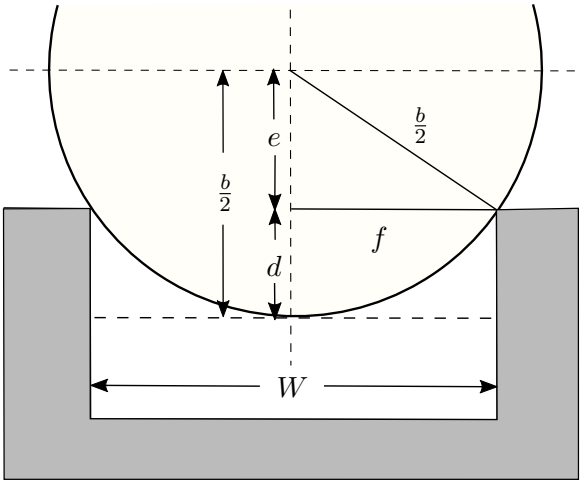

Figure B.2: Bearing ball geometry.

Using the circle geometry shown in Figure B.2, the following calculations can be performed. The height difference between the centre of the bearing ball and the top of the specimen, e, can be calculated using

$$e = \frac{b}{2} - d \quad . \tag{B.2}$$

Using Pythagoras' theorem, the horizontal distance between the centre of the bearing ball and the edge of the specimen gauge section, f, can be calculated using

$$f = \sqrt{\left(\frac{b}{2}\right)^2 - e^2} \quad . \tag{B.3}$$

Lastly, the specimen gauge section width, W, can be calculated using

$$W = 2f \quad . \tag{B.4}$$

Appendix C

Calculation of QST system input bar deflection

This appendix documents the approach for the calculation of the deflection of the QST system input bar. The closed-from successive integration method from Wilson et al. [51] is used and MATLAB is used in the solution process. The input bar is modelled as a simply-supported beam with a point load and an overhanging end. The overhang on the side of the eccentric bushing is neglected to simplify the calculation. The changes in diameter need to be incorporated in the area moment of inertia as it affects the final solution.

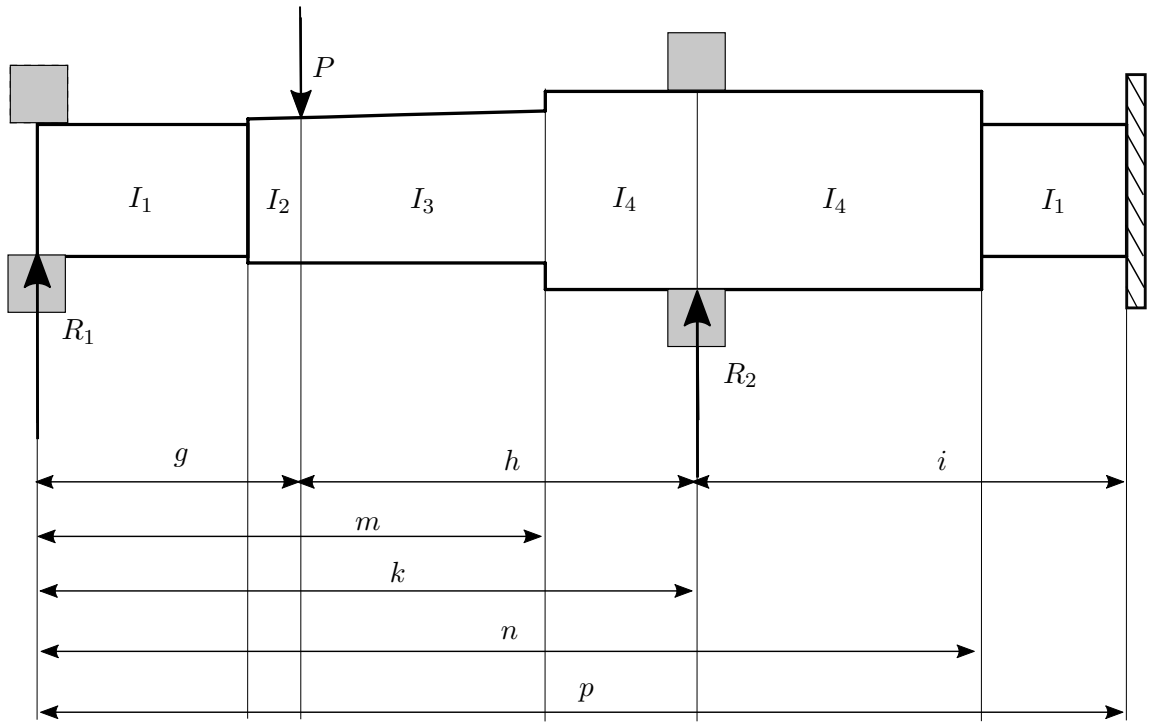

Figure C.1: Schematic representation of QST system input bar variables used for the calculation of bar deflection with shear forces and dimensions included.

Figure C.1 gives a schematic representation of the input bar. The boundary conditions are given by two bushings. The force equilibrium equation is given by

$$\sum F_y = R_1 - P + R_2 \quad . \tag{C.1}$$

The solutions for the reactions are given by

$$R_1 = \frac{Ph}{k} \tag{C.2}$$

and

$$R_2 = \frac{Pg}{k} \quad . \tag{C.3}$$

The moment equations are developed for each cross-section and each force added in the moment equation. Information of interest in the solution is the Young's modulus, E, taken as 200 GPa and the area moment of inertia. The method adopted requires moment equations for six intervals. Each interval will produce two constants of integration thus 12 constants of integration are to be found. The boundary conditions for the input bar are $y(0) = 0$ and $y(k) = 0$ which will provide two equations. The rest of the equations will be obtained from the compatibility conditions at the intersections of the six intervals. The moments are integrated to obtain the slope, $\frac{\partial y}{\partial x}$ and deflection, y equations. The integration results are summarized below.

For $0 < x < a$

$$M_1(x) = R_1 x \tag{C.4}$$

$$\int_0^a M_1(x)\,dx = EI_1\,\frac{\partial y_1}{\partial x} = R_1\frac{x^2}{2} + A \tag{C.5}$$

$$\int_0^a \int_0^a M_1(x)\,dx = EI_1\,y_1 = R_1\frac{x^3}{6} + Ax + B \tag{C.6}$$

For $a < x < g$

$$M_2(x) = R_1 x \tag{C.7}$$

$$\int_a^g M_2(x)\,dx = EI_2\,\frac{\partial y_2}{\partial x} = R_1\frac{x^2}{2} + C \tag{C.8}$$

$$\int_a^g \int_a^g M_2(x)\,dx = EI_2\,y_2 = R_1\frac{x^3}{6} + Cx + D \tag{C.9}$$

For $g < x < m$

$$M_3(x) = R_1 x - P(x-g) \tag{C.10}$$

$$\int_g^m M_3(x)\,dx = EI_3\,\frac{\partial y_3}{\partial x} = R_1\frac{x^2}{2} - \frac{P}{2}(x-g)^2 + E \tag{C.11}$$

$$\int_g^m \int_g^m M_3(x)\,dx = EI_3\,y_3 = R_1\frac{x^3}{6} - \frac{P}{6}(x-g)^3 + Ex + F \tag{C.12}$$

For $m < x < k$

$$M_4(x) = R_1 x - P(x-g) \tag{C.13}$$

$$\int_m^k M_4(x)\,dx = EI_4\,\frac{\partial y_4}{\partial x} = R_1\frac{x^2}{2} - \frac{P}{2}(x-g)^2 + G \tag{C.14}$$

$$\int_m^k \int_m^k M_4(x)\,dx = EI_4\,y_4 = R_1\frac{x^3}{6} - \frac{P}{6}(x-g)^3 + Gx + H \tag{C.15}$$

For $k < x < n$

$$M_5(x) = R_1 x - P(x-g) + R_2(x-k) \tag{C.16}$$

$$\int_k^n M_5(x)\,dx = EI_4\,\frac{\partial y_5}{\partial x} = R_1\frac{x^2}{2} - \frac{P}{2}(x-g)^2 + \frac{R_2}{2}(x-k)^2 + I \tag{C.17}$$

$$\int_k^n \int_k^n M_5(x)\,dx = EI_4\,y_5 = R_1\frac{x^3}{6} - \frac{P}{6}(x-g)^3 + \frac{R_2}{6}(x-k)^3 + Ix + J \tag{C.18}$$

For $n < x < l$

$$M_6(x) = R_1 x - P(x-g) + R_2(x-k) \tag{C.19}$$

$$\int_n^l M_6(x)\,dx = EI_1\,\frac{\partial y_6}{\partial x} = R_1\frac{x^2}{2} - \frac{P}{2}(x-g)^2 + \frac{R_2}{2}(x-k)^2 + K \tag{C.20}$$

$$\int_n^l \int_n^l M_6(x)\,dx = EI_1\,y_6 = R_1\frac{x^3}{6} - \frac{P}{6}(x-g)^3 + \frac{R_2}{6}(x-k)^3 + Kx + L \tag{C.21}$$

Substituting $x = 0$ yields $C_2 = 0$. The other conditions can be written in matrix form as

$$\begin{bmatrix} 1 & -\alpha_1 & 0 & 0 & 0 & 0 & 0 \\ a & -a(\alpha_1) & -\alpha_1 & 0 & 0 & 0 & 0 \\ 0 & 1 & 0 & -\alpha_2 & 0 & 0 & 0 \\ 0 & m & 1 & -m(\alpha_2) & -\alpha_2 & 0 & 0 \\ 0 & 0 & 0 & 1 & 0 & -\alpha_3 & 0 \\ 0 & 0 & 0 & n & 1 & -n(\alpha_3) & -\alpha_3 \\ 0 & 0 & 0 & k & 1 & 0 & 0 \end{bmatrix} \begin{Bmatrix} C_1 \\ C_2 \\ C_3 \\ C_4 \\ C_5 \\ C_6 \\ C_7 \end{Bmatrix}$$

$$= \begin{Bmatrix} \frac{R_1}{2}a^2(\alpha_1 - 1) \\ \frac{R_1}{6}a^3(\alpha_1 - 1) \\ \frac{R_1}{2}m^2(\alpha_2 - 1) + \frac{P(m-g)^2}{2}(1-\alpha_2) \\ \frac{R_1}{6}m^3(\alpha_2 - 1) + \frac{P(m-g)^3}{6}(1-\alpha_2) \\ \frac{R_1}{2}n^2(\alpha_3 - 1) + \frac{P(n-g)^2}{2}(1-\alpha_3) + \frac{R_2}{2}(n-k)^2(\alpha_3 - 1) \\ \frac{R_1}{6}n^3(\alpha_3 - 1) + \frac{P(n-g)^3}{6}(1-\alpha_3) + \frac{R_2}{6}(n-k)^3(\alpha_3 - 1) \\ -\frac{R_1}{6}k^3 + \frac{P}{6}(k-g)^3 \end{Bmatrix}$$

where $\alpha_1 = \frac{I_1}{I_2}$, $\alpha_2 = \frac{I_2}{I_3}$,$\alpha_3 = \frac{I_3}{I_1}$ and $I_2 = I_3$. Young's modulus is omitted since it cancels out of the equations. On four occurrences, two constants are equal and thus cancels out and results in only eight constants needing to be determined. The resultant deflection curve is shown in Figure C.2.

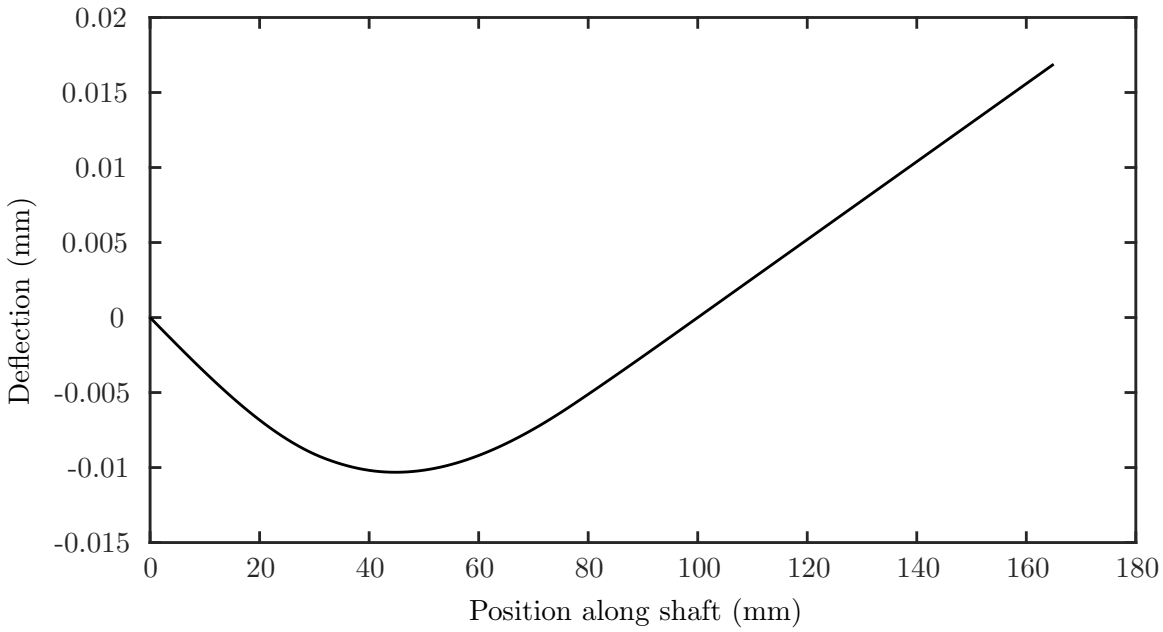

Figure C.2: Deflection of input bar.

Appendix D

Shear wave speed and shear modulus calculations

This appendix documents the calculation of the experimental shear wave speed and experimental shear modulus of each bar/tube. The experimental shear wave speed and shear modulus values are fundamental to ensuring the accuracy of the obtained shear stress vs shear strain data. The density is calculated using the measured dimensions of the bar as well as the measured mass (using an electronic digital scale) by

$$\rho = \frac{M}{\pi L({D_o}^2 - {D_i}^2)/4} \tag{D.1}$$

where ρ is the density of the bar, M is the mass of the bar, L is the length of the bar, D_o is the outer diameter and D_i is the inner diameter.

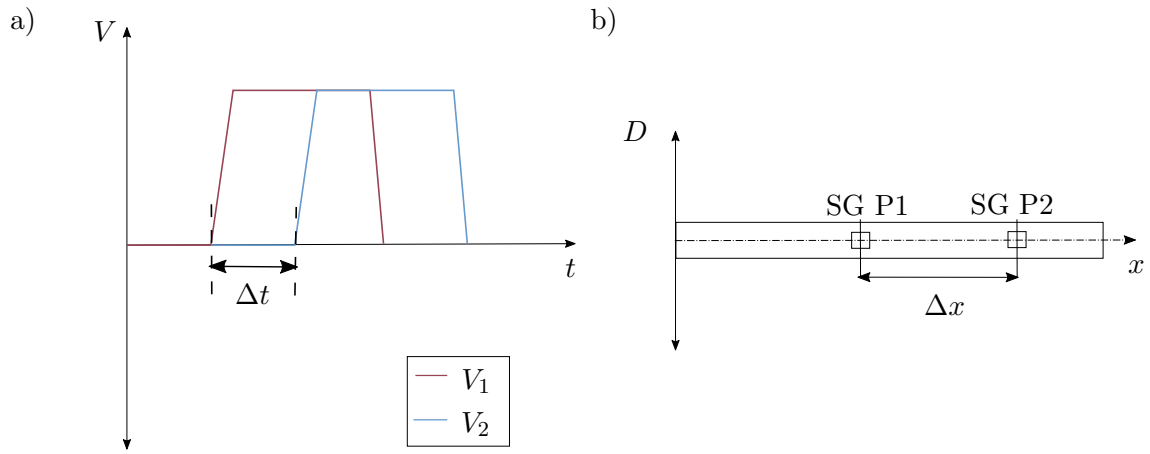

Figure D.1: Idealised TSHB data when using two strain gauges on bar where (a) voltage vs time data and (b) schematic representation of the TSHB apparatus.

The shear wave speed is calculated using the measured wave signals as well as the location of the strain gauges on both bars as shown in Figure D.1. Using the measured signals, the time required for the signal to travel from the first strain gauge to the second strain gauge is calculated. The shear wave speed is then

$$c = \frac{\Delta x}{\Delta t} \tag{D.2}$$

where Δx is the physical distance between the two strain gauges and Δt is the time required for the wave to travel between the two strain gauges. An alternative method to measuring the

shear wave speed when only one strain gauge is available is to measure the physical distance between the strain gauge and the free end as well as the time required for the signal to travel to the free end and back. Lastly, the experimental shear modulus is calculated by

$$G = c^2 \rho \tag{D.3}$$

where G is the experimental shear modulus.

Appendix E

Experimental procedures

This appendix documents the assembly of the QST system as well as the experimental procedure for both the QST and the TSHB systems.

E.1 QST system assembly and set-up of mechanical components

a) b)

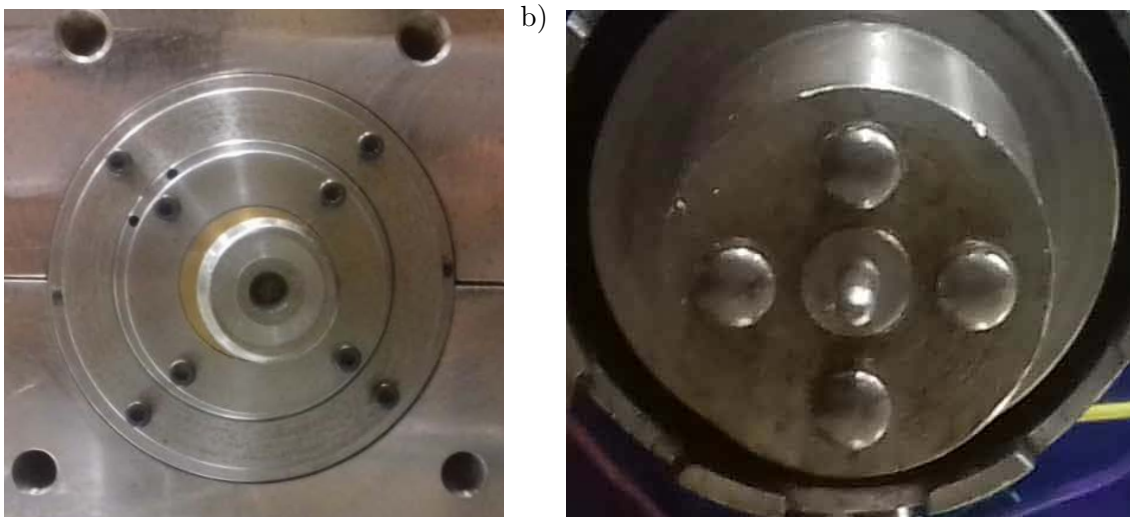

Figure E.1: Assembled components. a) Double eccentric bushing and b) Input bar with dowel pins.

1. Assemble the double eccentric bushing using bolts as shown in Figure E.1 (a).
2. Press the five dowel pins into the five pin holes located on the input bar as shown in Figure E.1 (b).
3. Press the involute cam onto the input bar at the tapered interface. Check that the involute cam is perpendicular to the input bar. The assembled involute cam-input bar connection is shown in Figure E.2 (a)
4. Press the brass bushing into the housing as shown in Figure E.2 (b).

a) b)

Figure E.2: Assembled components. a) Involute cam-input bar connection and b) Brass bushing into housing.

5. Connect the base plate and the housing via the dowel pins and bolts as shown in Figure E.3 (a).

6. Slide the input-involute cam connection through the brass bushing ensuring that the pin side of the connection is on the same side as the castellations on the housing as shown in Figure E.3 (b).

a) b)

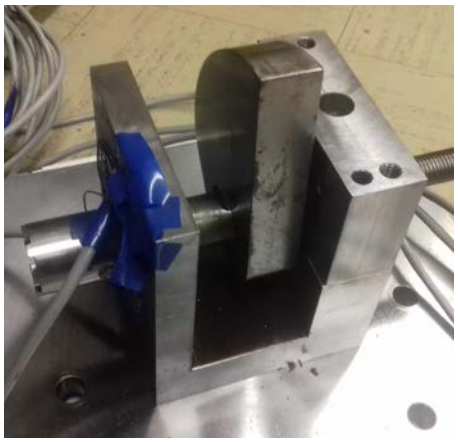

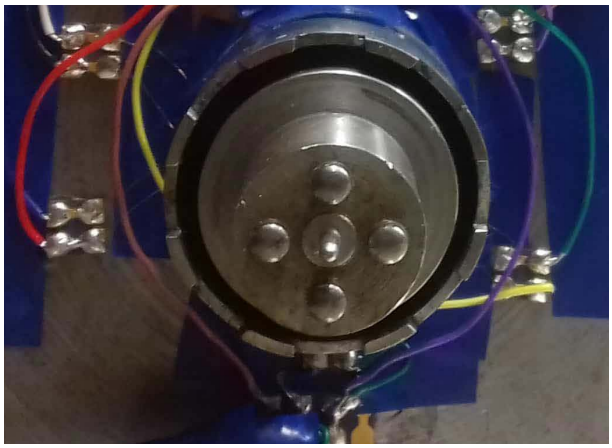

Figure E.3: Assembled components. a) Housing connection to base plate and b) Specimen end of QST system.

7. Slide the double eccentric bushing around the input bar and locate it on the housing ensuring the bolted side of the double eccentric bushing faces away from the involute cam as shown in Figure E.4 (a).

8. Bolt the bushing cover to the housing and clamp the double eccentric bushing using the threaded bolts.

a) b)

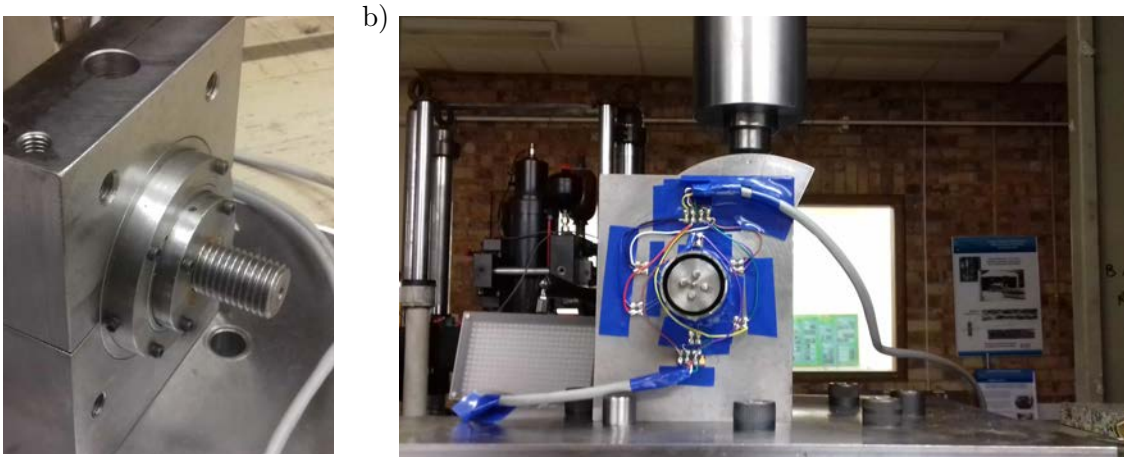

Figure E.4: Assembled components. a) Double eccentric bushing end of QST system and b) Fully assembled QST system.

9. Secure the base plate to the Zwick machine base.
10. Turn the crosshead connector onto the crosshead of the Zwick machine. The fully assembled QST system is shown in Figure E.4 (b).

E.2 QST system Experimental procedure

A series of steps need to be carried out when conducting a test using the QST system apparatus.

1. Set-up the DAQ system ensuring that all the wiring is correct and turn it on once ready.
2. Ensure that all bolts are turned tightly.
3. Ensure that the input bar is concentrically positioned by adjusting the double eccentric bushing.
4. Check that the bar and tube is concentrically aligned using the specially designed tool shown in Figure E.5.

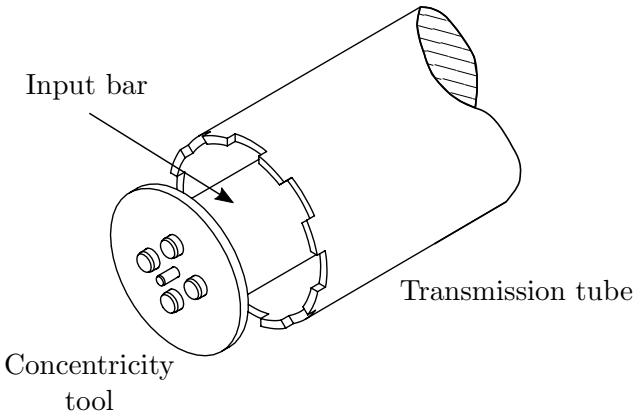

Figure E.5: Procedure to check for concentricity.

5. Mount the specimen onto the input bar ensuring that no bending of the specimen occurs and the specimen is fully inserted.

6. Rotate the input bar to ensure that the castellations of the specimen presses perfectly into the castellations of the tubular portion. Ensure that the involute cam is placed in the correct position to allow for the crosshead connector to contact the involute cam.

7. Insert the eight self-tapping screws into the specimen.

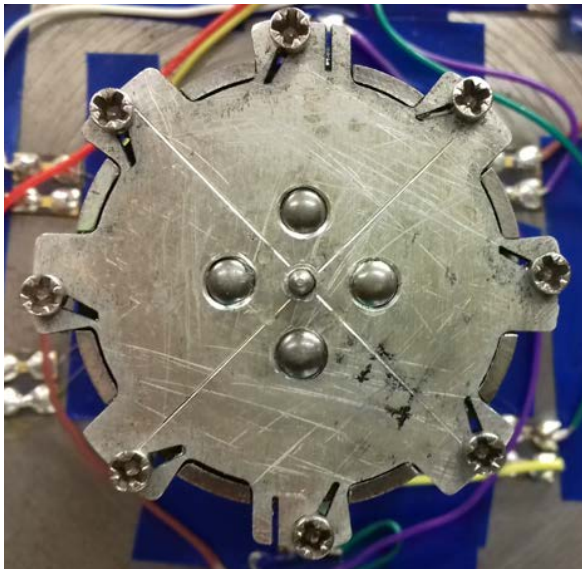

Figure E.6: Fully mounted specimen

8. Lubricate the surface of the involute cam with oil.

The following steps should be taken in order to conduct a QST system test:

1. Zero the force on the Zwick machine software as well as the HBM Quantum X.

2. Start the test.

3. Once the test is complete, dismount the specimen off both the incident bar and the transmission tube using the procedure described in Section 5.6 and ensure no damage is done to the specimen.

E.3 TSHB Experimental procedure

A series of steps need to be carried out when conducting a test using the TSHB apparatus. Caution must be taken when operating the bottle jack to ensure the apparatus is operated safely. The following steps should be taken before carrying out a test:

1. Set-up the DAQ system ensuring that all wiring is correct and turn it on once it is ready.

2. Verify that all the valves on the bottle jack are closed and no oil is leaking from the bottle jack shown in Figure E.7 (a).

a) b)

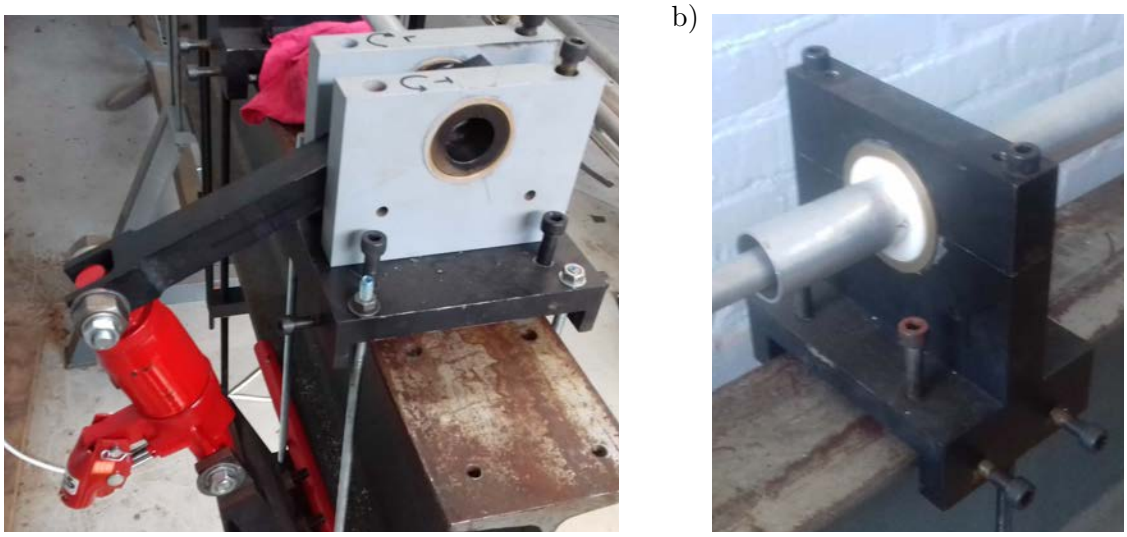

Figure E.7: TSHB components. a) Loading-application mechanism and b) Bearing stands.

3. Ensure that all support fixtures, shown in Figure E.7 (b) are aligned as required and all bolts are adjusted to restrict the movement of the support fixtures and all other components on the I-beam.

4. Check that the load-application mechanism is mounted correctly to the incident bar. The mounting is shown in Figure E.8 (a)

a) b)

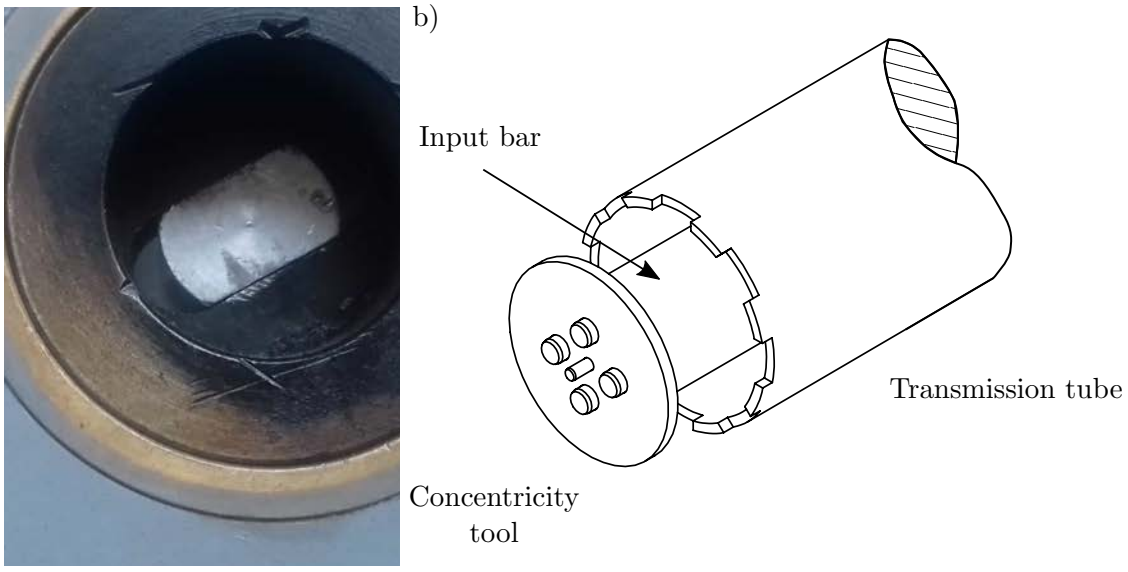

Figure E.8: TSHB components. a) Load-application mechanism and incident bar connection and b) Concentricity tool.

5. Check that the bar and tube is concentrically aligned using the specially designed tool shown in Figure E.8 (b).

6. Clamp the incident bar using one of the clamping mechanisms, shown in Figure E.9(a), and ensure no bending of the incident bar occurs.

a) b)

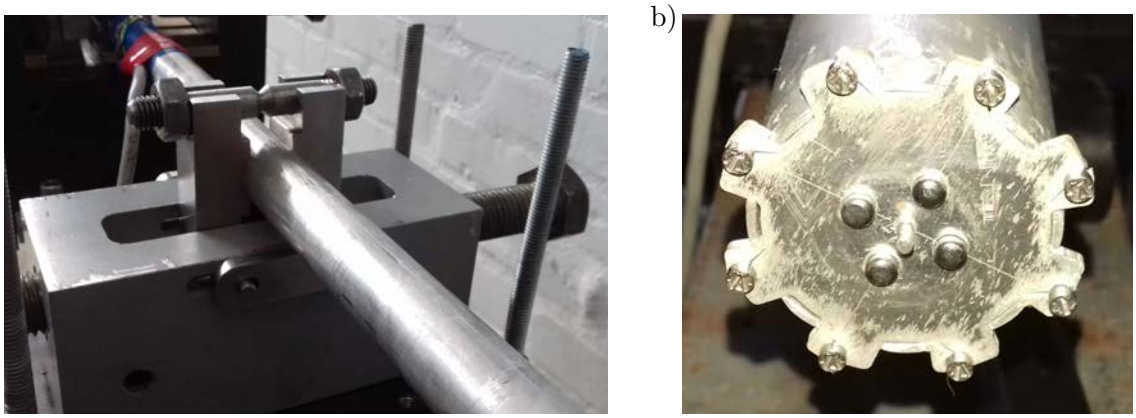

Figure E.9: TSHB components. a) Fracture-pin clamping mechanism and b) Fully mounted specimen.

7. Mount the specimen onto the incident bar ensuring that no bending occurs and the specimen is fully inserted.

8. Rotate the transmission tube to ensure that its castellations presses perfectly into the castellations of the specimen. Once again, the mounting should result in no bending of the specimen as well as ensuring the specimen is fully mounted. Insert the eight self-tapping screws to ensure all eight castellations of the specimen are in contact with the matching castellations on the transmission tube. A fully mounted specimen is shown in Figure E.9 (b).

9. On the DAQ system, open the picoscope software and ensure all parameters are set for the TSHB apparatus.

The following steps should be taken in order to conduct a TSHB test:

1. The picoscope program should be started to give a live reading of the loading pulse.

2. Use the bottle jack handle and jack up the bottle jack to the required level. To ensure the correct amount of torque is applied to the incident bar, work out beforehand the maximum voltage that can be measured and ensure the Picoscope never goes over that range.

3. Once sufficient torque is applied, release the bar by deactivating the clamping mechanism resulting in the required stress wave.

4. Once the test is completed, dismount the specimen off both the incident bar and the transmission tube using the procedure described in Section 5.6 and ensure no damage is done to the specimen during dismounting.

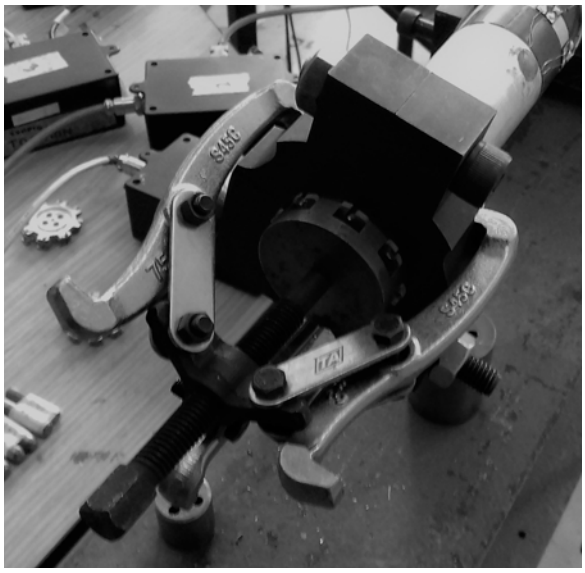

Figure E.10: Dismounting of specimen off the transmission tube.

5. Save the DAQ file.

Appendix F

Wave seperation

This appendix documents the adopted wave seperation technique.

In order to fully understand the motion of the travelling torsional waves in the bars, a simple, efficient wave separation technique proposed by Park et al. [52] was adopted. The technique allows for the separation of component waves travelling in opposite directions in the bars. This permits the analysis of the elastic waves for an extended time duration and is achieved using the strain measurement at one point and a known end condition. The desire for the extended time duration arises from the limitation in standard SHPB experiments which makes direct interpretation of waves possible for a maximum duration of one round-trip wave reflection in the bar. The limitation of the direct interpretation is influenced by the positioning of the strain gauges and the length of the bars.

Complications result from the superposition of waves travelling in opposite directions which hinders the direct inference of the individual waves. The motivation for extended time histories come about from applications that match the extended occurrences. Specimen damage often accumulates over time due to repeated loadings of the incident bar which mimics certain applications where multiple loadings exist. The technique is based on the theory of one-dimensional wave propagation and involves the solving of time domain difference equations. This assumption is especially relevant in TSHB work, as torsional waves are not subject to wave dispersion. The technique results in the determination of two unknown functions for transient pulses travelling in opposite directions.

F.1 Transmission tube

The d'Alembert travelling wave solution is

$$\varepsilon(x,t) = \varepsilon_1\left(t - \frac{x}{c}\right) + \varepsilon_2\left(t + \frac{x}{c}\right) \tag{F.1}$$

where ε_1 is the right-going wave and ε_2 is the left-going wave. Incorporating the above equation into the analysis of the TSHB waves yields

$$\varepsilon_A(t) = \varepsilon_1(t - t_a) + \varepsilon_2(t + t_a) \tag{F.2}$$

where $\varepsilon_A(t) = \varepsilon(a,t)$ at SG_3 and $t_a = \frac{a}{c}$, where c is the shear wave speed.

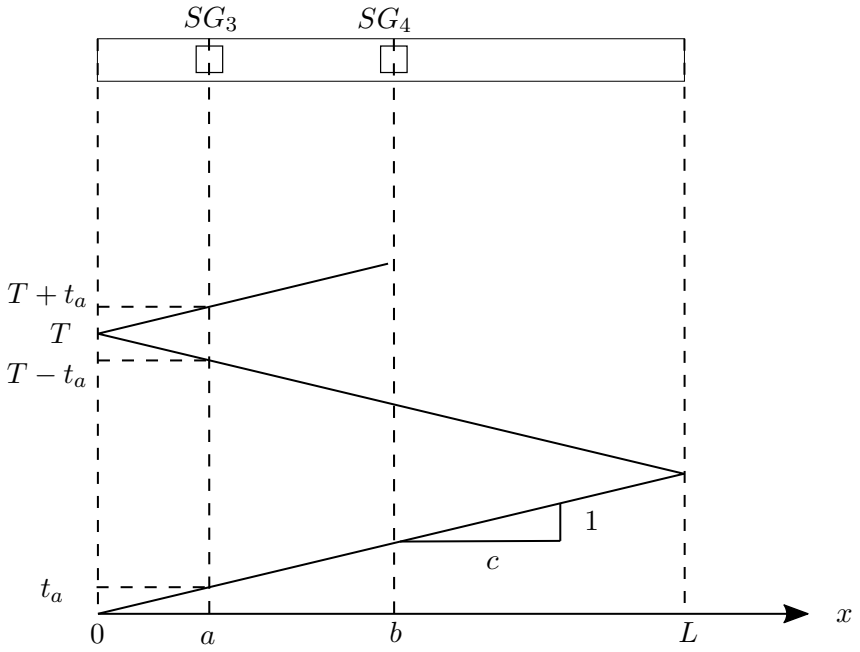

Figure F.1: Lagrangian (or time-distance) diagram for the torsional waves in the transmission tube

In Figure F.1, $t = 0$ corresponds to the time the initial signal of the transmitted wave transmits through to the transmission tube and $T = 2L/c$, where L is the length of the tube. The initial signal travels to distance $x = a$ at time $t = t_a$, at which point the right-going wave is detected by SG_3. The wave then proceeds to the free end of the tube where it reflects and propagates back towards the specimen interface. At time $t = T - t_a$, the left-going wave is detected at distance $x = a$ by SG_3.

From equation (F.1), it is apparent that the complete solution depends entirely on the two wave functions ε_1 and ε_2. The method adopted incorporates the known free end condition at the right end of the tube where the stress should always be equal to zero. This known end condition effectively replaces the need for two strain measurements on the transmission tube. The time domain equations are shown below.

For $t < T - t_a$
No reflected wave passes through the strain gauge at $x = a$, thus

$$\varepsilon_2(t + t_a) = 0 \tag{F.3}$$

From (F.2) and (F.3):

$$\varepsilon_A(t) = \varepsilon_1(t - t_a) \tag{F.4}$$

For $t > T - t_a$
Both $\varepsilon_1(t - t_a)$ and $\varepsilon_2(t + t_a)$ are nonzero in general. However, invoking the free-end boundary condition at $x = L$ via (F.1):

$$\varepsilon_1\left(t - \frac{L}{c}\right) + \varepsilon_2\left(t + \frac{L}{c}\right) = 0 \tag{F.5}$$

This, along with (F.2), gives

$$\varepsilon_A(t) = \varepsilon_1(t - t_a) - \varepsilon_1(t - T + t_a) \tag{F.6}$$

The combination of (F.3)-(F.6) yields functions ε_1 and ε_2 in terms of the measured strain ε_A as

$$\begin{aligned} \varepsilon_1(t) &= \varepsilon_A(t + t_a) && \text{for } t < T - t_a \\ \varepsilon_1(t) &= \varepsilon_1(t - T + 2t_a) + \varepsilon_A(t + t_a) && \text{for } t > T - t_a \end{aligned}$$

$$\begin{aligned} \varepsilon_2(t) &= 0 && \text{for } t < T - t_a \\ \varepsilon_2(t) &= -\varepsilon_1(t - T) && \text{for } t > T - t_a \end{aligned}$$

Based off the functions obtained for ε_1 and ε_2, the strain histories at various positions on the tube can be obtained by substituting the distance into Equation (F.1).

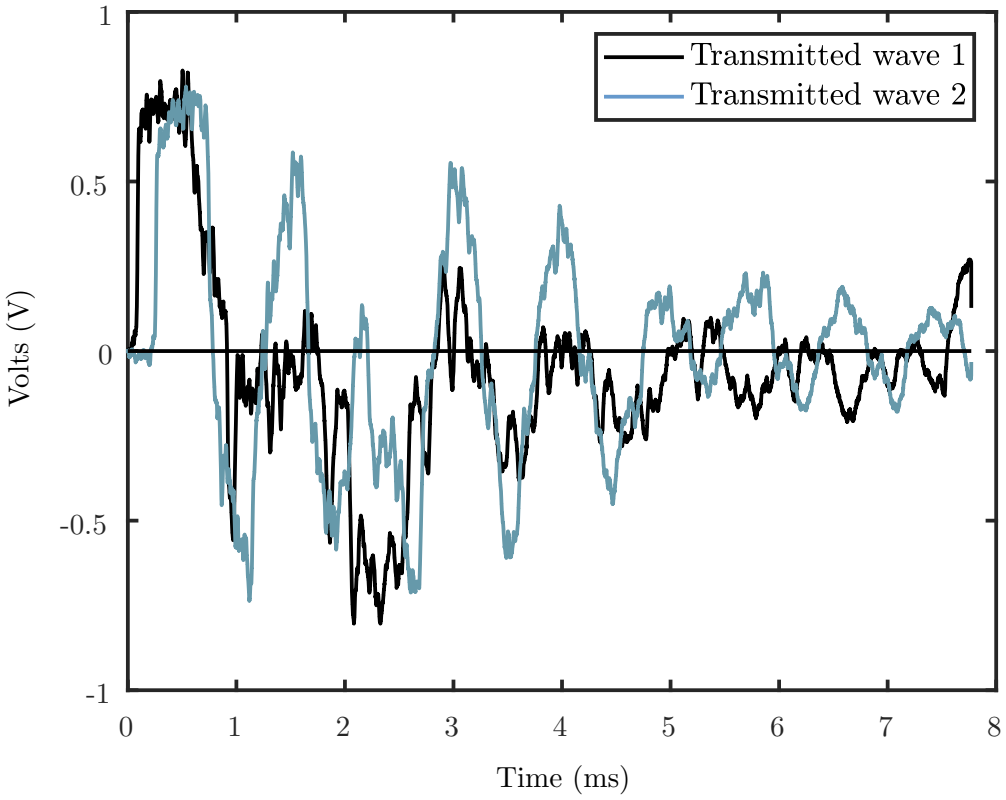

Figure F.2: Two recordings of the transmitted wave from a TSHB test.

Figure F.2 shows an example of the two recordings of the transmitted wave from a TSHB test. Note how similar the initial signal of the two recordings are. However, due to the wave reflection off the free end and the location of the strain gauges on the tube, the rest of the signals differ.

To investigate the validity of the wave seperation technique, it is important to determine whether the limit conditions used are recovered when building the waves at those locations, particularly the stress at the free end which should be equal to zero at all times. A comparison of the calculated profiles and the measured profiles are done to verify the accuracy of the technique. A further verification is done by using wave functions ε_1 and ε_2 to reconstruct the wave at a second position of strain measurement on the transmission tube. It becomes apparent when doing this comparison that an accumulation of system errors results due to the iterative process.

At the strain gauge 3 position:

$$\varepsilon(a,t) = \varepsilon_1\left(t - \frac{a}{c}\right) + \varepsilon_2\left(t + \frac{a}{c}\right) = \varepsilon_1(t - t_a) + \varepsilon_2(t + t_a) \tag{F.7}$$

At the free end position:

$$\varepsilon(L,t) = \varepsilon_1\left(t - \frac{L}{c}\right) + \varepsilon_2\left(t + \frac{L}{c}\right) = \varepsilon_1(t - T/2) + \varepsilon_2(t + T/2) \tag{F.8}$$

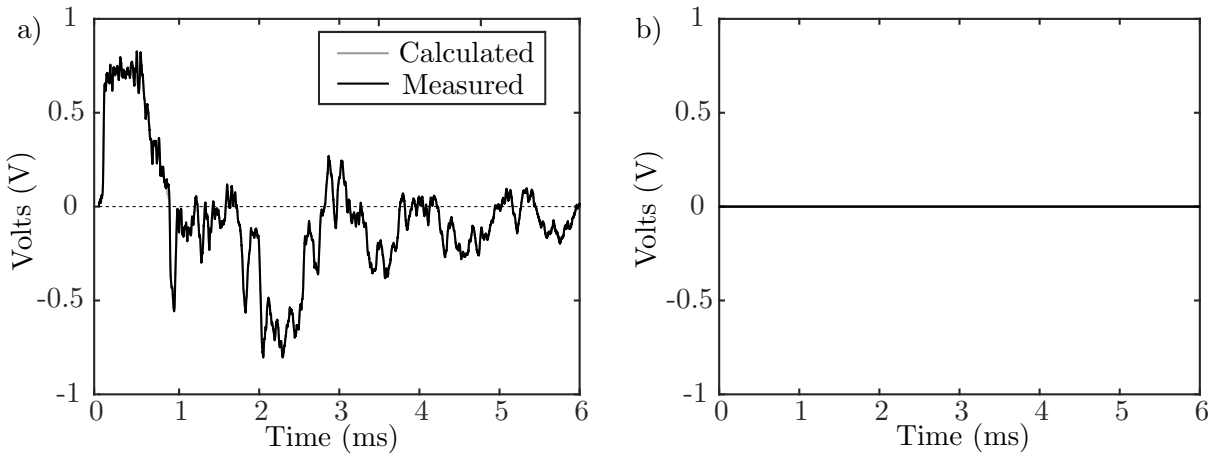

Figure F.3: A comparison of the measured and calculated profiles (a) at the location of strain gauge 3, (b) at the location of the free end.

A comparison of the measured profiles and the calculated profiles are shown in Figure F.3. It can be observed that there is good agreement between the two profiles at the location of the strain gauge and free end. The small local differences can be attributed to the effects of signal noise and incorrect calibration of the strain gauges.

At the strain gauge 4 position:

$$\varepsilon(b,t) = \varepsilon_1\left(t - \frac{b}{c}\right) + \varepsilon_2\left(t + \frac{b}{c}\right) = \varepsilon_1(t - t_b) + \varepsilon_2(t + t_b) \tag{F.9}$$

At the specimen interface ($x = 0$):

$$\varepsilon(0,t) = \varepsilon_1\left(t - \frac{0}{c}\right) + \varepsilon_2\left(t + \frac{0}{c}\right) = \varepsilon_1(t) + \varepsilon_2(t) \tag{F.10}$$

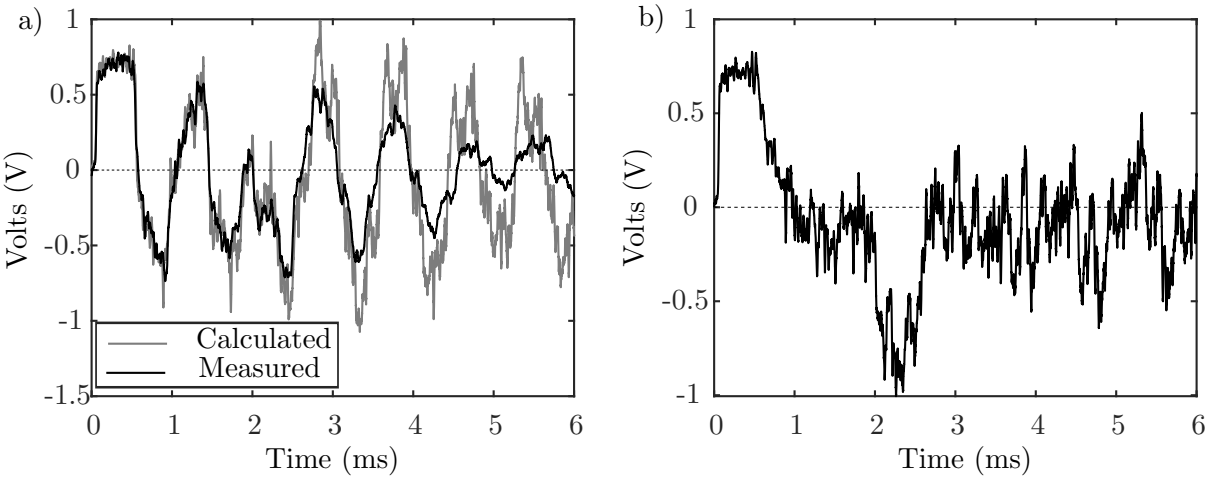

Figure F.4: A comparison of the measured and calcaulted profiles (a) at the location of strain gauge 4, (b) at the location of the specimen interface.

There is evidence of error propagation after a few iterations thus imprecision is unavoidable as shown in Figure F.4(a). The technique adopted produces cumulative errors that decreases the quality of the results with the distance covered by the waves. An effective error analysis technique should be developed to compensate for the produced cumulative errors.

Revisiting the obtained transmitted wave from the TSHB test, shown in Figure F.4(b), we note a second loading on the signal. To verify the second loading, a Lagrangian diagram (shown in Figure F.5) is constructed to identify the time at which the second loading is expected to arrive and whether it corresponds to the arrival in the actual test. It was found that this was in good agreement.

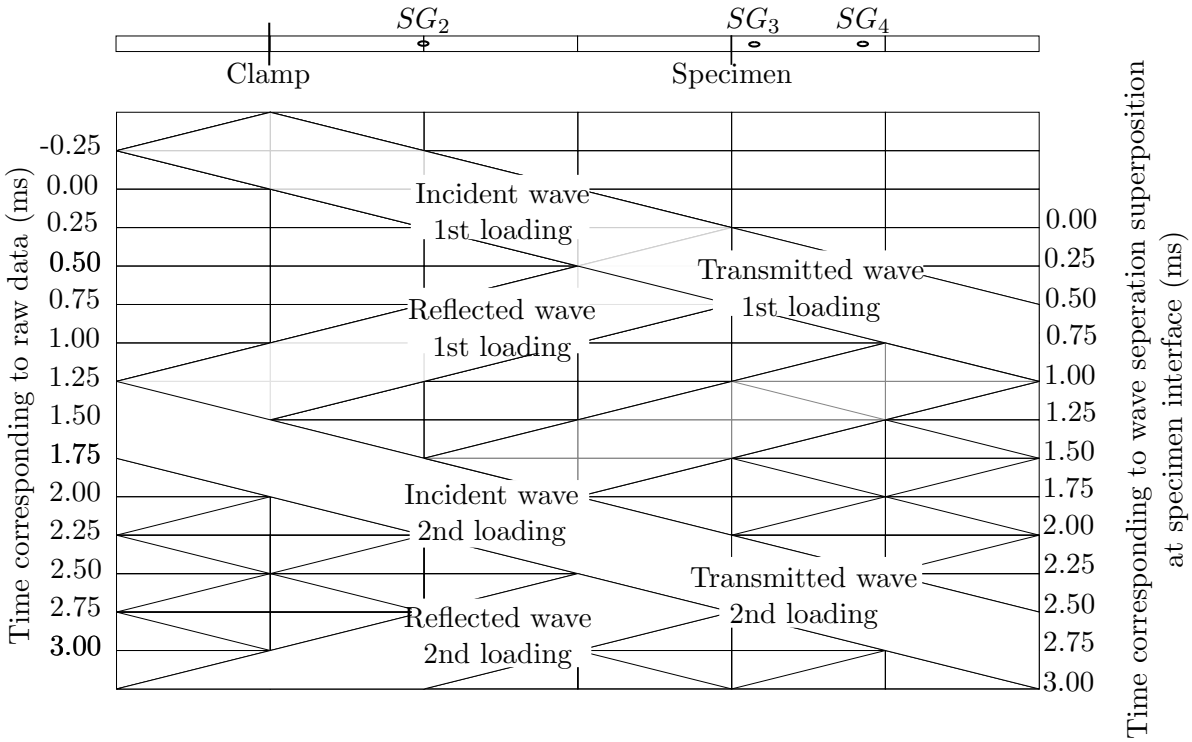

Figure F.5: Lagrangian diagram and configuration of the torsional split Hopkinson bar setup.

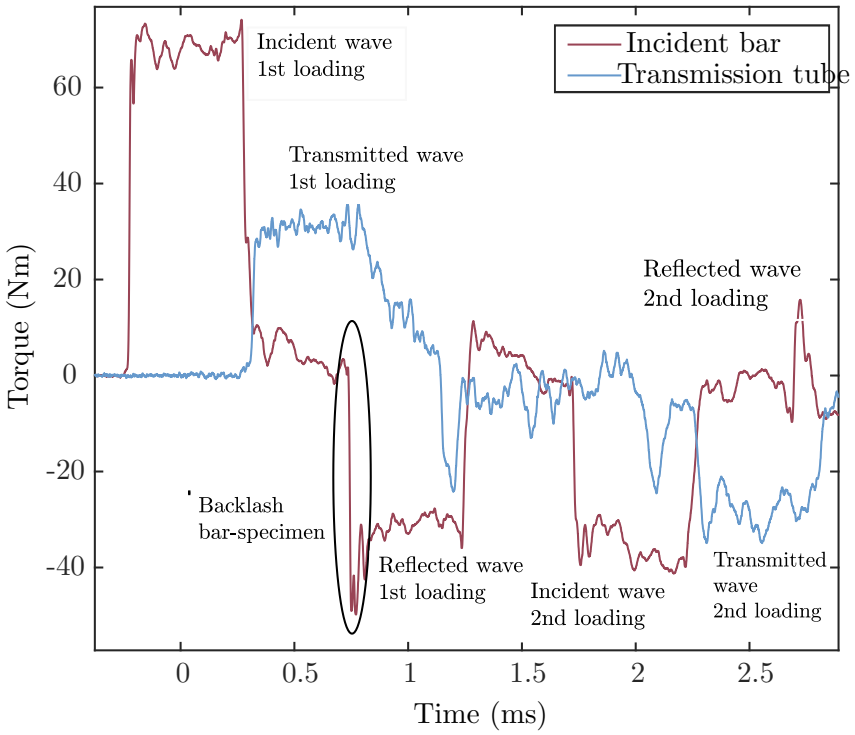

Figure F.6: Strain waves measured in the incident bar and the transmission tube.

Figure F.6 shows the measured strain waves. Note that the reflected wave is opposite to the sign of the incident wave. This reflected wave propagates away from the specimen and towards the loading end after which it reflects a second time at the left end of the incident bar. The sign of

the wave remains unchanged thus the resulting torsional wave has opposite sign to the initial incident wave. Subsequently, the second loading will be in an opposite direction to the first loading.

It is evident from the obtained transmission wave that forward and reverse loading of the specimen takes place successively in the same experiment. Such loading events may be necessary to simulate the real forming processes where strain path changes occur.

F.2 Incident bar

Upon the release of the clamping mechanism, a left-going and right-going wave is generated. For simplicity in the wave separation technique, we ignore the initial left-going wave since after bouncing off the fixed end and returning to the clamp, its torque releases to zero thereby playing no further significant role in the reconstruction. Also, for simplicity, we take t = 0 to synchronize with the left fixed end. We assume $\varepsilon_A = 0$ from the left end to the position of the clamp for This is the initial signal in the right-going wave reconstruction.

For $t < T - t_a$
No reflected wave passes through the strain gauge at $x = a$, thus

$$\varepsilon_2(t + t_a) = 0 \tag{F.11}$$

From (F.2) and (F.11):

$$\varepsilon_A(t) = \varepsilon_1(t - t_a) \tag{F.12}$$

For $T - t_a < t < T + t_a$
No reflected wave passes through the strain gauge at $x = a$, thus

$$\varepsilon_1(t - t_a) = 0 \tag{F.13}$$

From (F.2) and (F.13):

$$\varepsilon_A(t) = \varepsilon_2(t + t_a) \tag{F.14}$$

For $t > T - t_a$
Both $\varepsilon_1(t - t_a)$ and $\varepsilon_2(t + t_a)$ are nonzero in general. However, invoking the fixed boundary condition at $x = 0$, one obtains:

$$\varepsilon_1(t) - \varepsilon_2(t) = 0 \tag{F.15}$$

This, along with (F.2), gives

$$\varepsilon_A(t) = \varepsilon_2(t - t_a) - \varepsilon_2(t + t_a) \tag{F.16}$$

The combination of (F.11)-(F.16) together with changes of variables $(t-ta) \to \varphi$ and $(t+ta) \to \eta$ yields functions ε_1 and ε_2 in terms of the measured strain ε_A as

$$\begin{aligned} \varepsilon_1(\varphi) &= \varepsilon_A(\varphi + t_a) && \text{for } \varphi < T - 2t_a \\ \varepsilon_1(\varphi) &= 0 && \text{for } T - 2t_a < \varphi < T \\ \varepsilon_1(\varphi) &= \varepsilon_2(\varphi) && \text{for } \varphi > T \end{aligned}$$

$$\begin{aligned} \varepsilon_2(\eta) &= 0 && \text{for } \eta < T \\ \varepsilon_2(\eta) &= \varepsilon_A(\eta - t_a) && \text{for } T < \eta < T + 2t_a \\ \varepsilon_2(\eta) &= -\varepsilon_2(\eta - 2t_a) + \varepsilon_A(\eta - t_a) && \text{for } \eta > T + 2t_a \end{aligned}$$

Appendix G

Examples of flow stress

This appendix documents some examples of the regression curve fitted to the TSHB experimental data. The specimen gauge section width along with the strain rate for the corresponding specimens are given in Table G.1.

Table G.1: The specimen gauge section dimensions and corresponding strain rate

Specimen label	**Width (mm)**	**Strain rate (/s)**
SpecR4	4	1065
SpecR5	4	687
SpecP1	3	625
SpecRR2	2	2915
SpecQ1	1	4630
SpecQ3	1	4935
SpecM1	0.8	5955
SpecM4	0.8	6000
SpecH8	0.5	9300
SpecJ2	0.5	7080

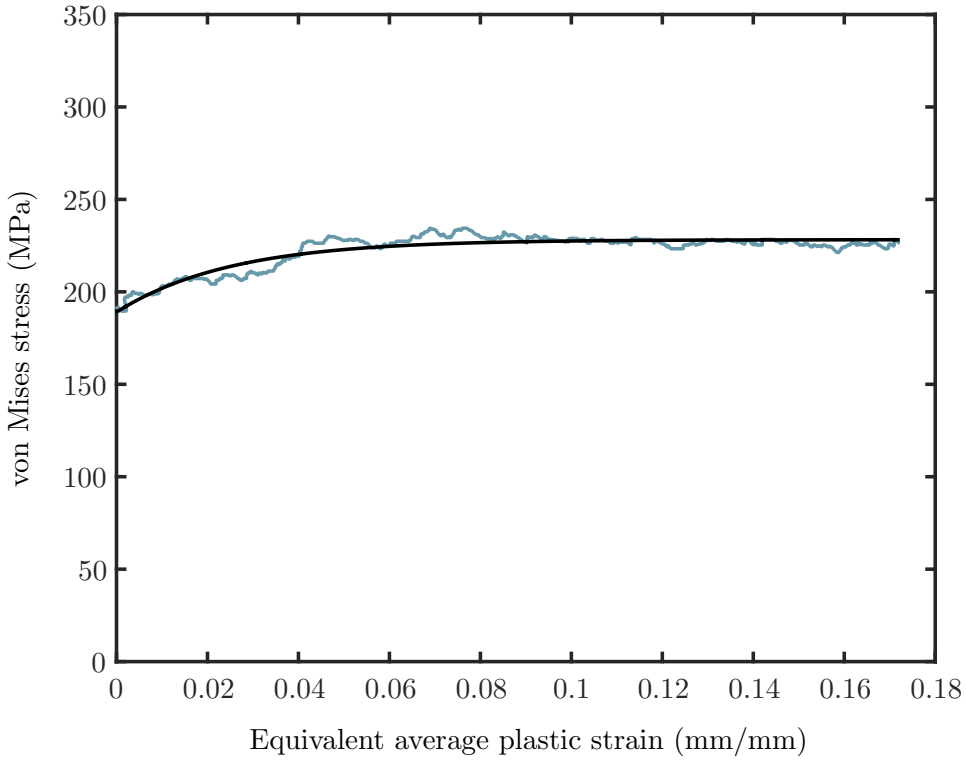

Figure G.1: Regression curve vs experimental data for SpecR4.

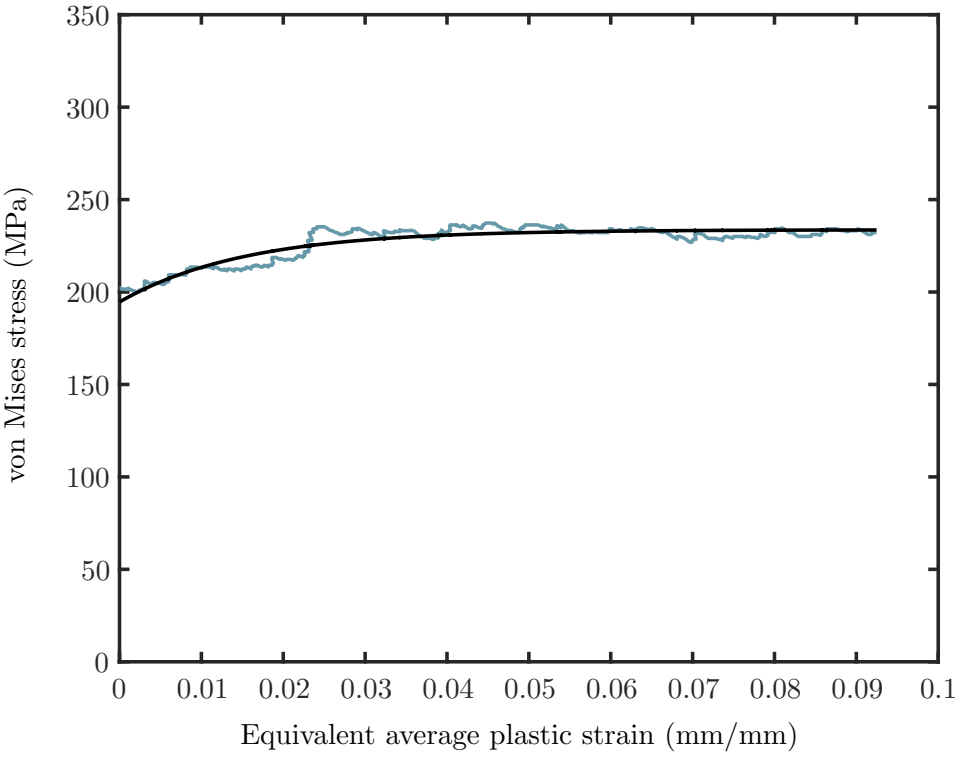

Figure G.2: Regression curve vs experimental data for SpecR5.

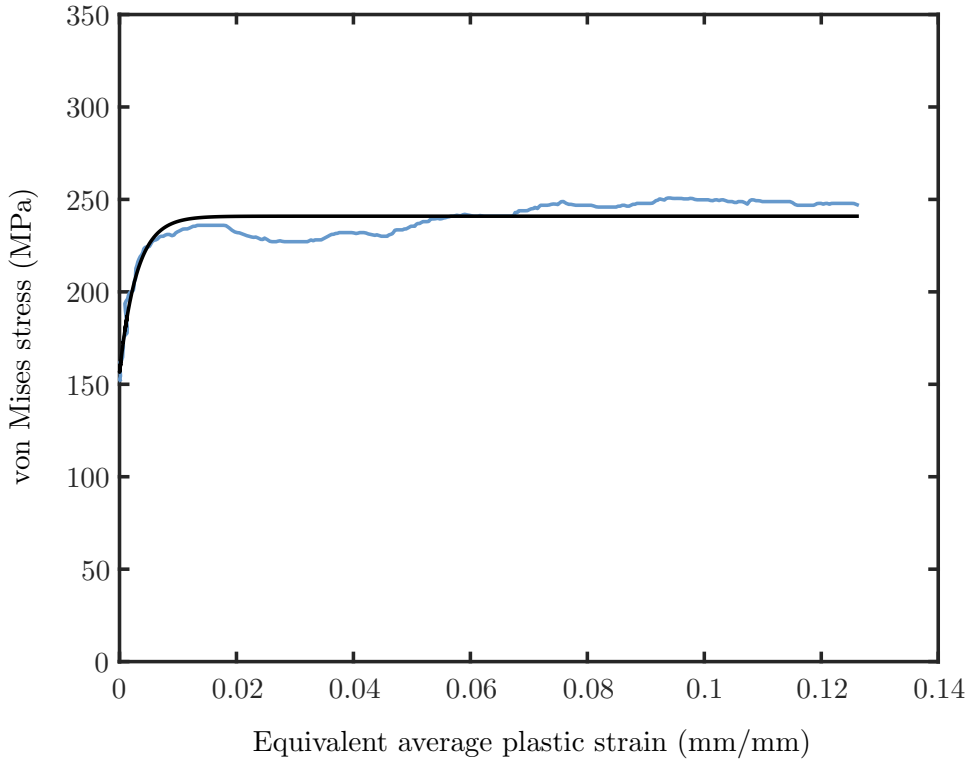

Figure G.3: Regression curve vs experimental data for SpecP1.

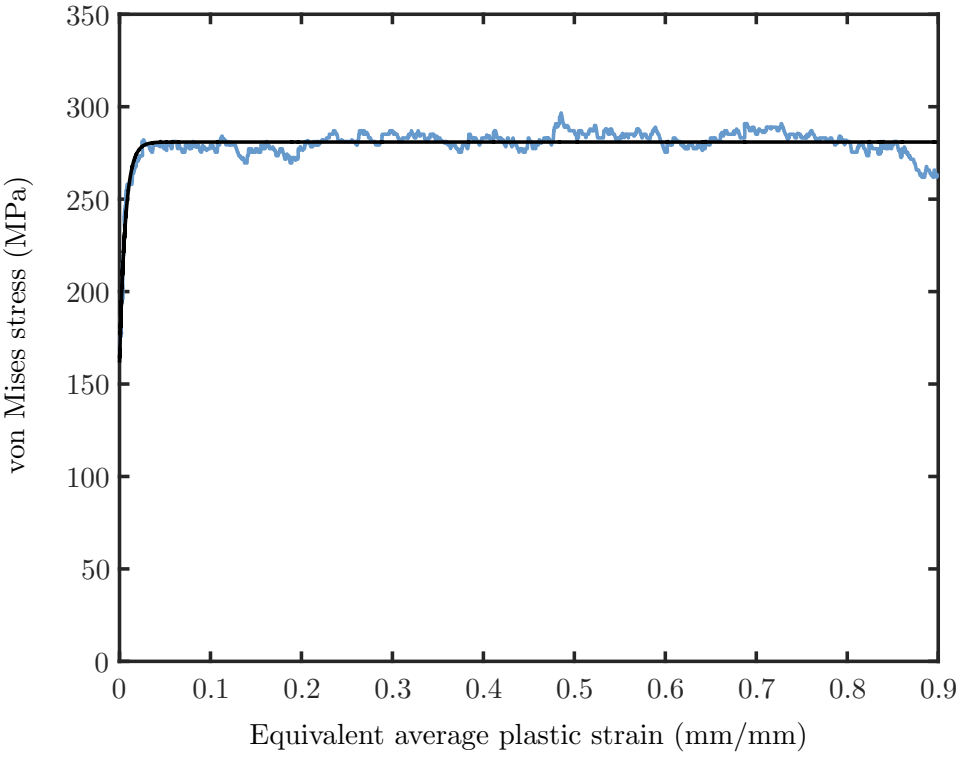

Figure G.4: Regression curve vs experimental data for SpecRR2.

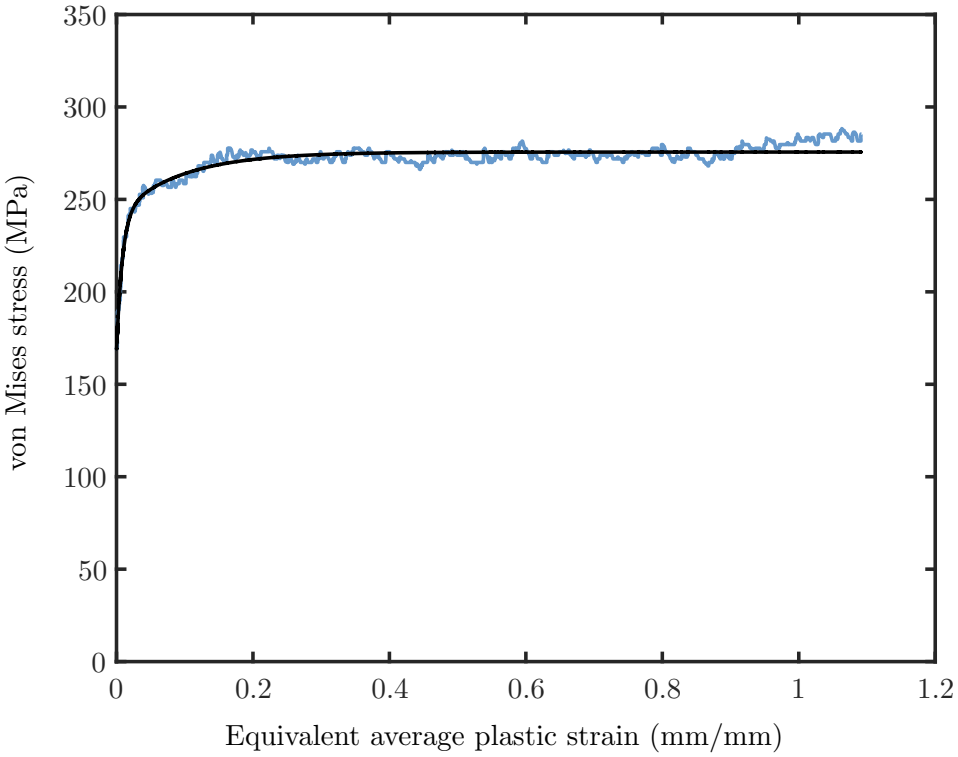

Figure G.5: Regression curve vs experimental data for SpecQ1.

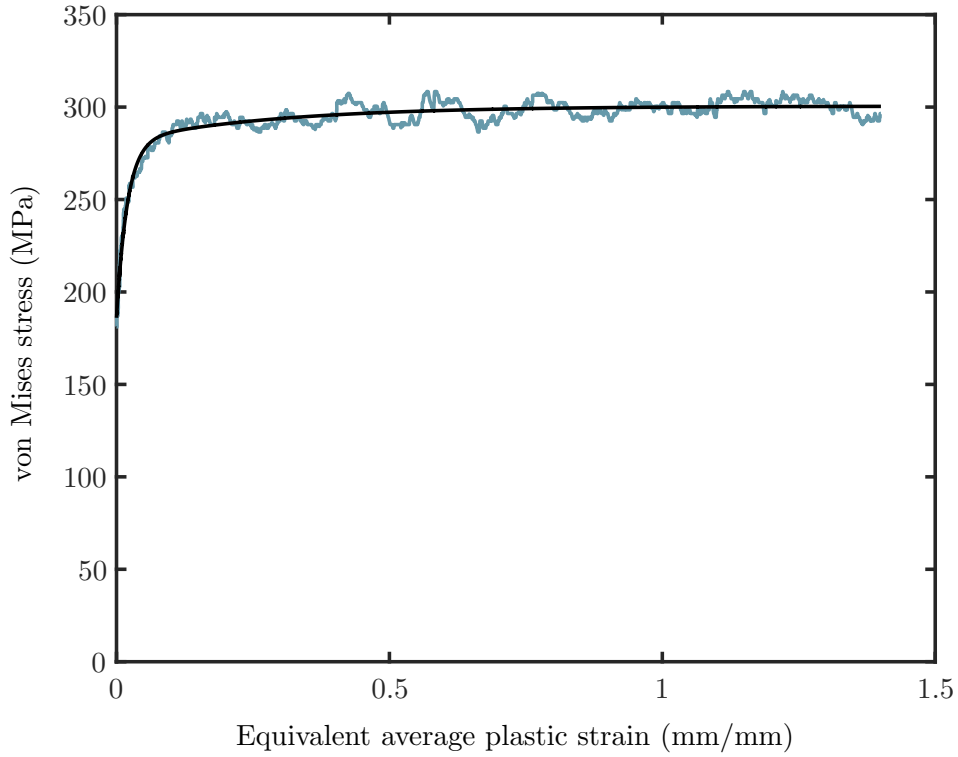

Figure G.6: Regression curve vs experimental data for SpecQ3.

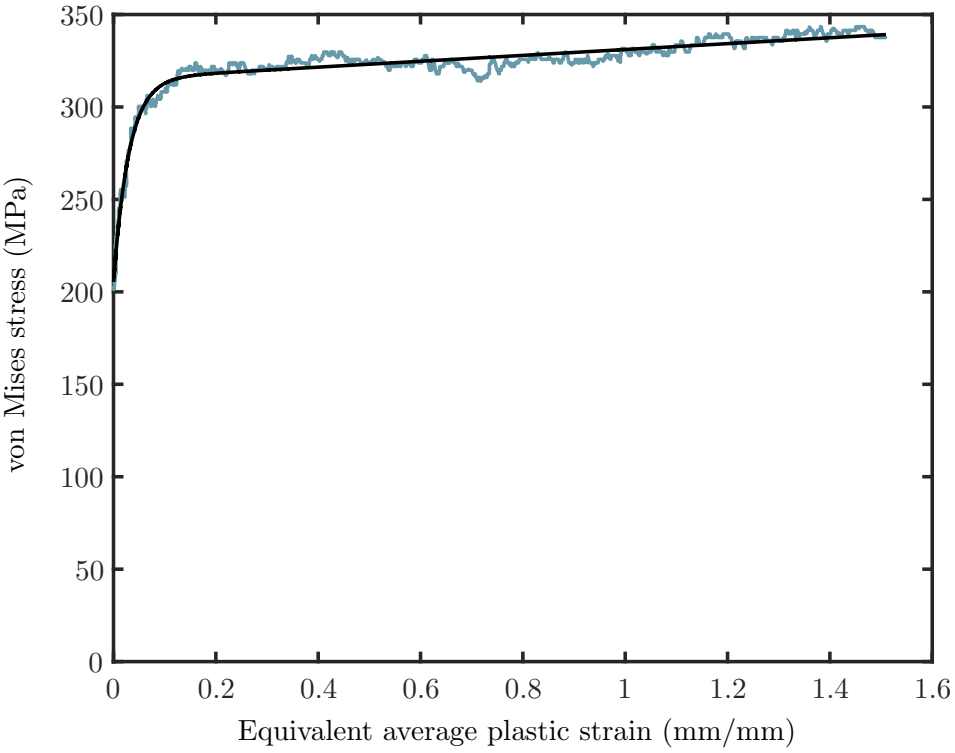

Figure G.7: Regression curve vs experimental data for SpecM1.

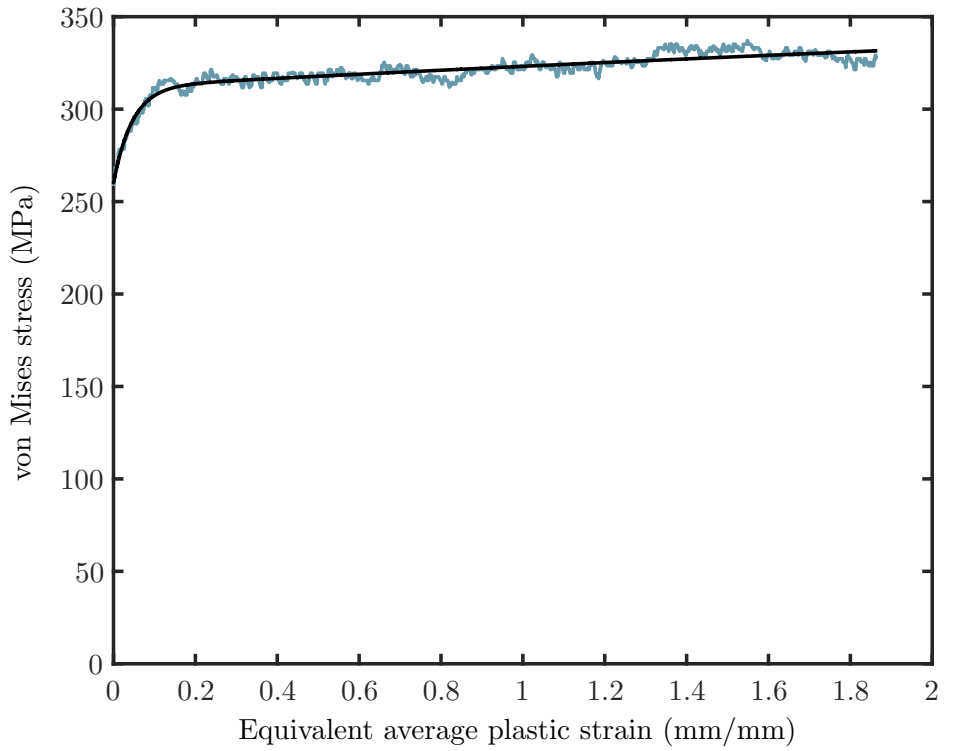

Figure G.8: Regression curve vs experimental data for SpecM4.

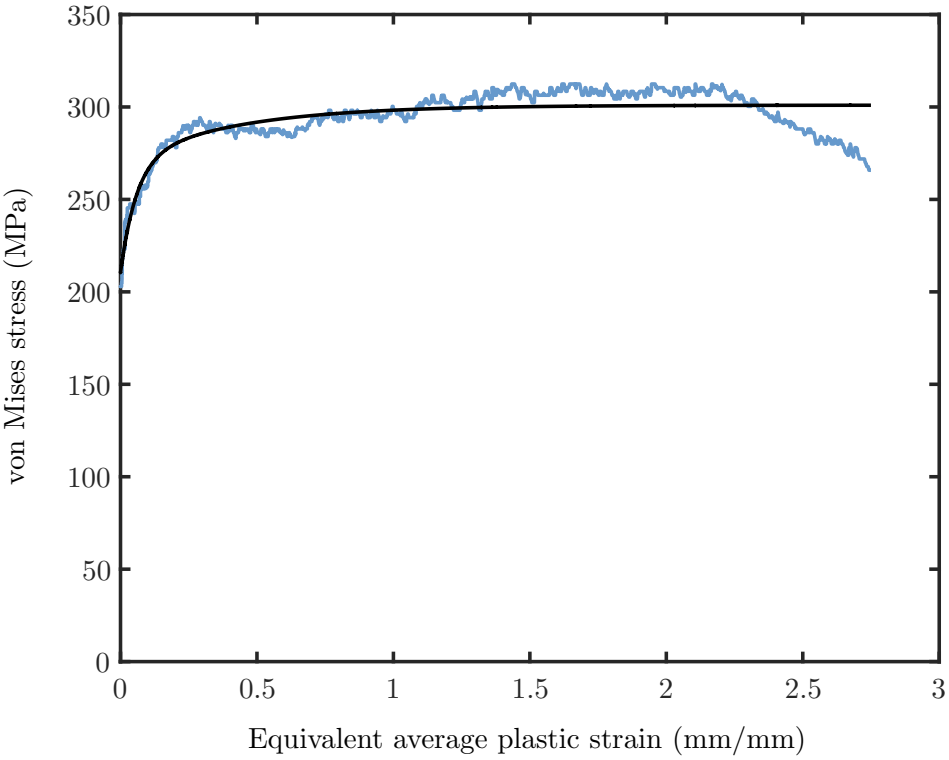

Figure G.9: Regression curve vs experimental data for SpecH8.

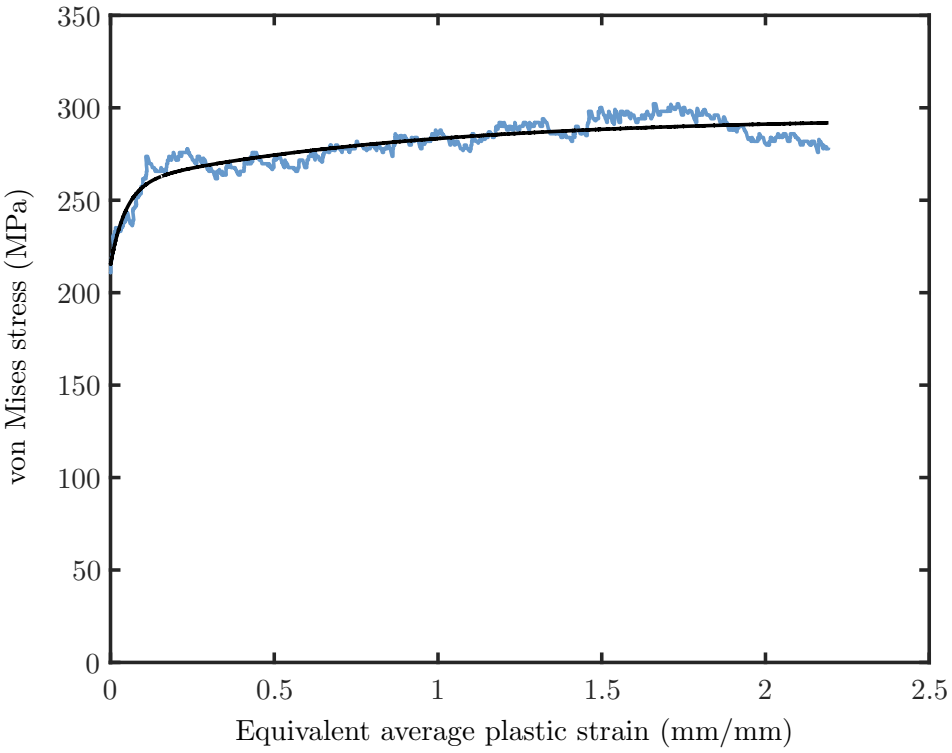

Figure G.10: Regression curve vs experimental data for SpecJ2.

Appendix H

Drawings

This appendix contains some of the technical drawings made for the various components of this project. Further detailed drawings are available in digital format and can be accessed via the UCT DMP library.

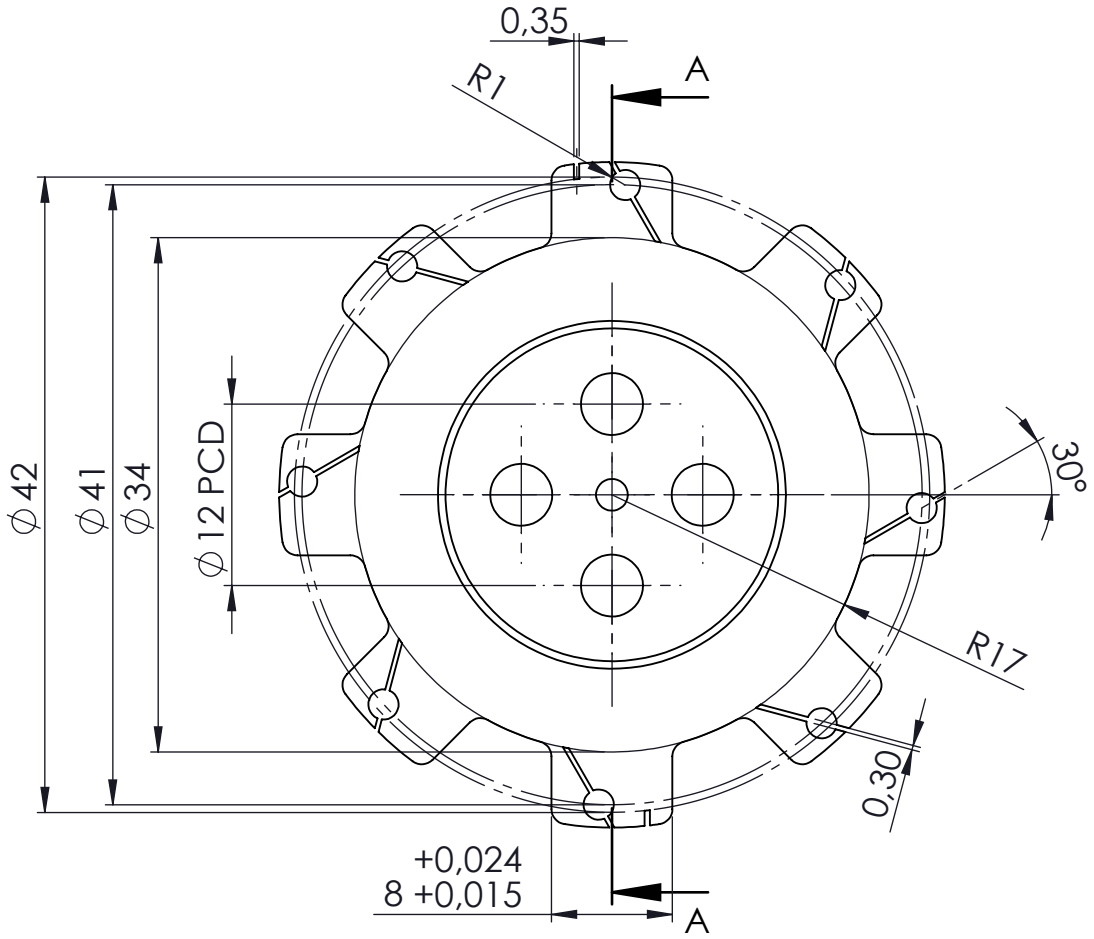

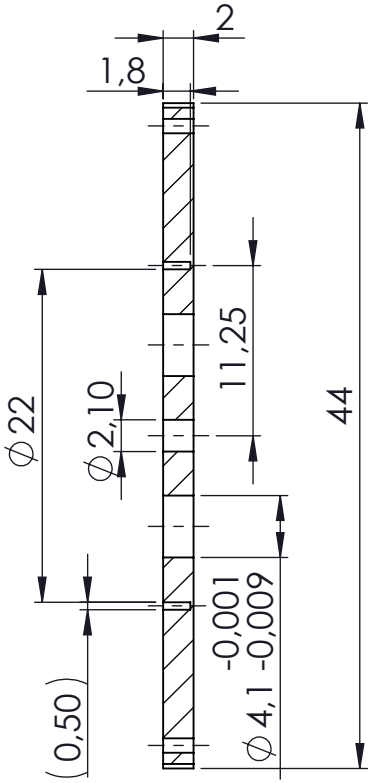

SECTION A-A

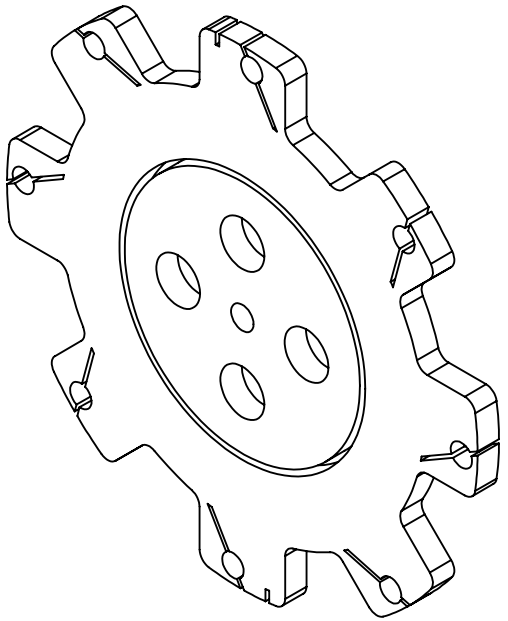

NOTE:
2X 0.35mm slits spaced diametrically opposite one another.
SLITS SHOULD BE PARALLEL TO ROLLING DIRECTION OF SHEET METAL.

INNER EDGE DIAMETER SHOULD ALWAYS BE 22 MM.

QUANTITY: 10

NOTE:
1. 8 x 8mm slotted keyways evenly spaced at 45 degrees apart.
2. 8 x 2.1mm diameter holes evenly spaced at 45 degrees apart(thorugh holes) with 0.3mm slits
3. 4 x 4.1mm diameter holes evenly spaced
4. Fillet radius = 1mm

Scale: 2:1 on A4	University of Cape Town Department of Mechanical Engineering			
Drawn By: Muhsin Osman	All un-toleranced dimensions to adhere to ISO 2768-m	Title: 0.5mm Gauge width specimen		
Checked :	Material : Aluminium 1050-0	Drawing Number :	Rev. : A	Sheet : 1 of 1

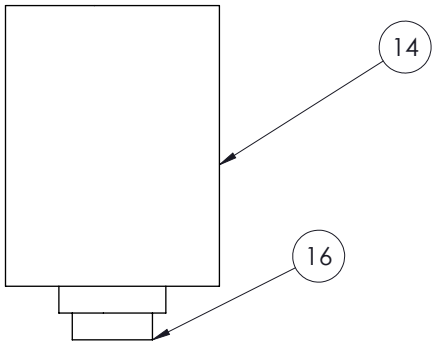

DETAIL B
SCALE 1 : 2

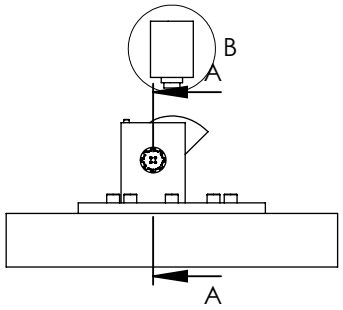

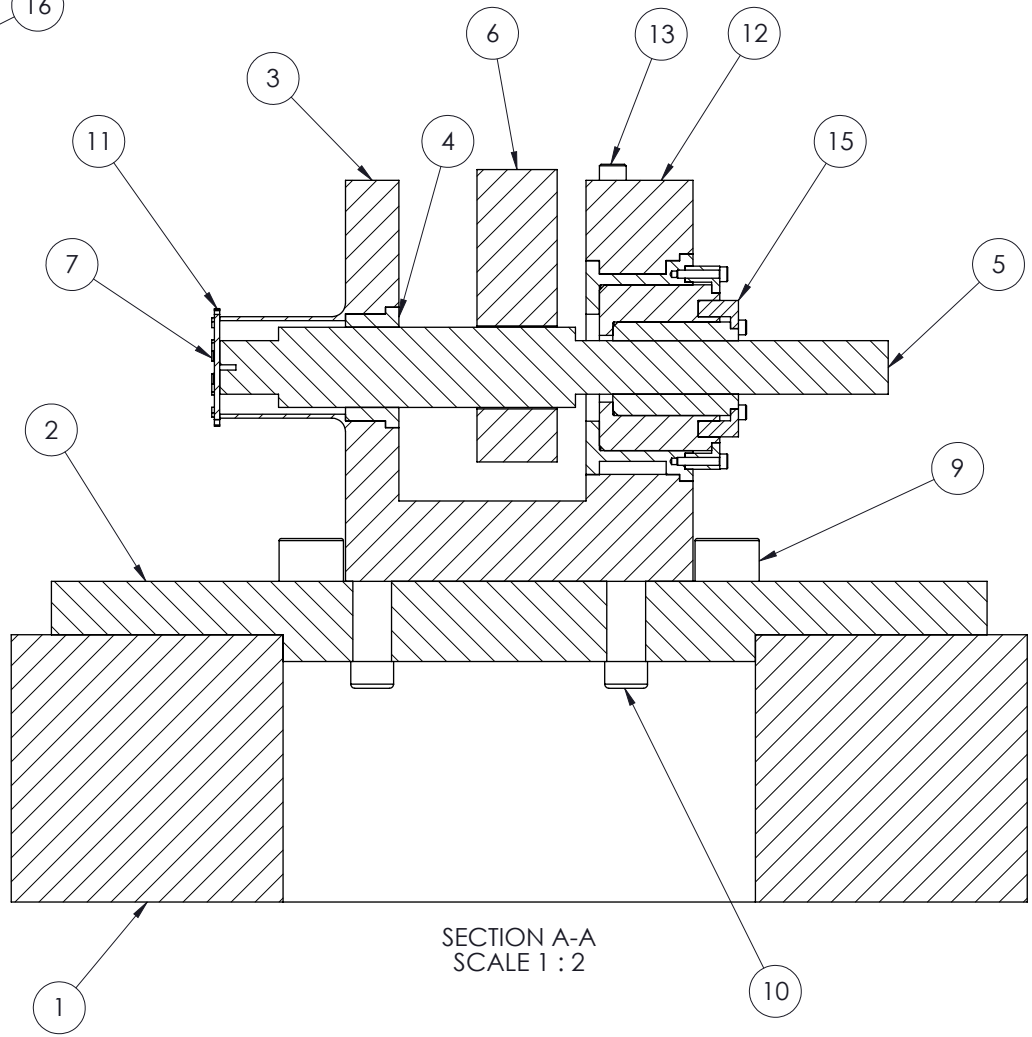

SECTION A-A
SCALE 1 : 2

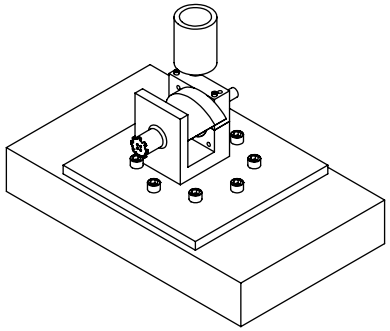

ITEM NO.	PART NAME	MATERIAL	QTY.
16	QSTS CROSSHEAD CONNECTOR SLIDER	AISI 1080 STEEL	1
15	QSTS ECCENTRIC BUSH ASSEMBLY	AISI 1080 STEEL & BRASS	1
14	QSTS CROSSHEAD CONNECTOR	AISI 1080 STEEL	1
13	M6 HEX BOLT	B18.3.1M - 6 X 1.0 X 100 HEX SHCS -- 24NHX	2
12	QSTS BUSHING 2 COVER	AISI 1080 STEEL	1
11	QSTS SPECIMEN	AL/CU/SS	1
10	M10 HEX BOLT	ISO 4762 M10 X 40 - 40N	4
9	M16 HEX BOLT	ISO 4762 M16 X 40 - 40N	8
8	6 MM DOWEL PIN	ISO 8734 - 6 X 32 - A - ST	6
7	4 MM DOWEL PIN	ISO 8734 - 4 X 20 - A - ST	4
6	QSTS CAM	AISI 1080 STEEL	1
5	QSTS INPUT BAR	AISI 1080 STEEL	1
4	QSTS BUSHING 1	BRASS	1
3	QSTS HOUSING	AISI 1080 STEEL	1
2	QSTS BASE	AISI 1080 STEEL	1
1	ZWICH MACHINE BASE	EXISTING	1

Scale: 1:5 on A3

University of Cape Town
Department of Mechanical Engineering

Drawn By: Muhsin Osman

All un-toleranced dimensions to adhere to ISO 2768-m

Title: Quasi-static Torsional System Assembly

Checked :

Assembly drawing

Drawing Number : QSS ASM 1

Rev. : A

Sheet : 1 of 1

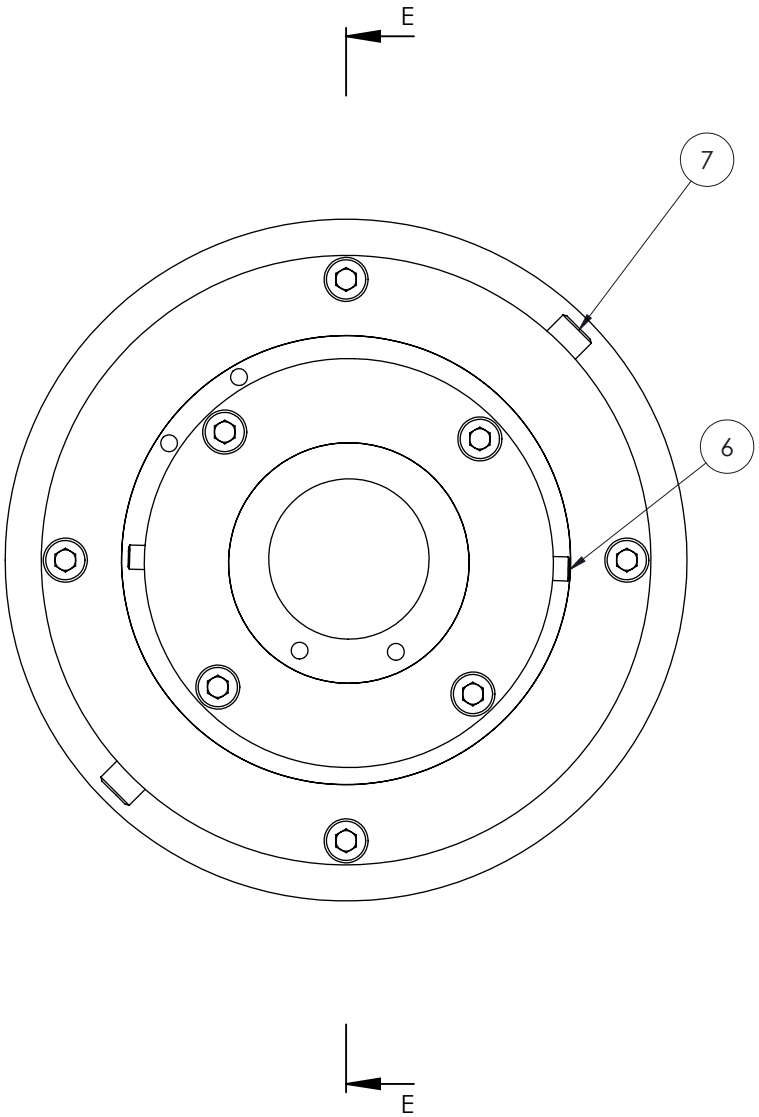

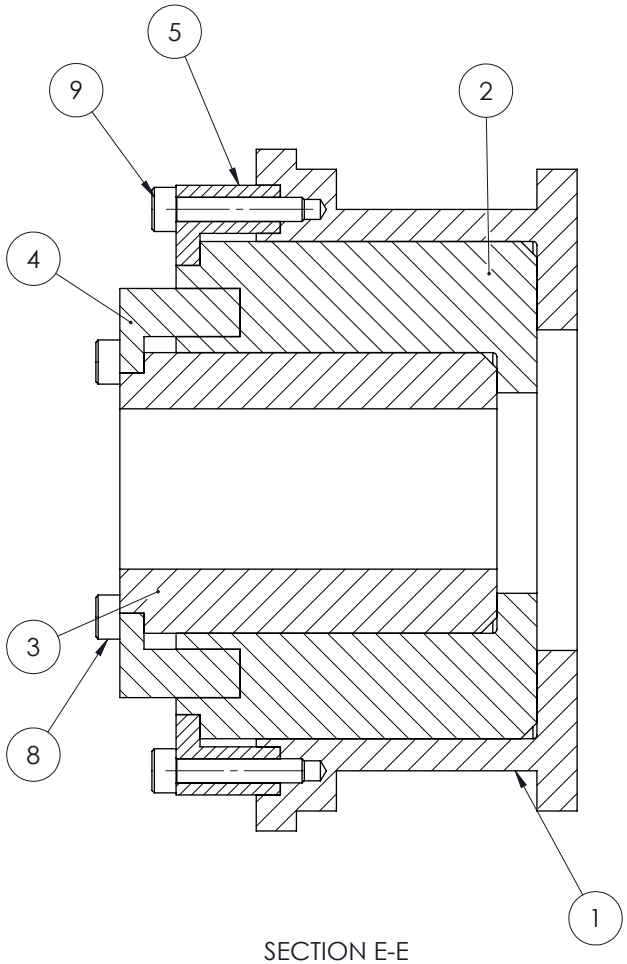

SECTION E-E
SCALE 1.5 : 1

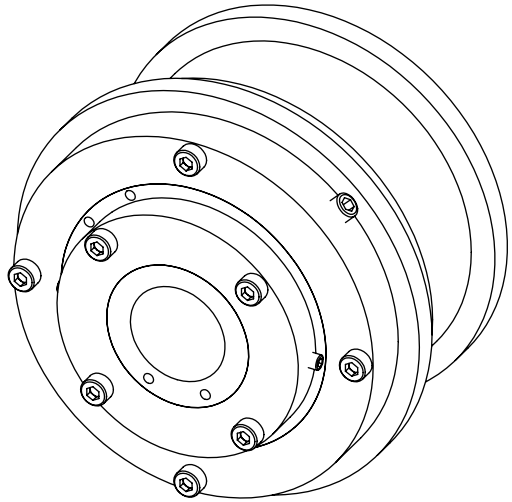

ITEM NO.	PART NAME	MATERIAL	QTY.
9	M3 HEX BOLT	B18.3.1M - 3 x 0.5 x 16 Hex SHCS -- 16NHX	4
8	M3 HEX BOLT	B18.3.1M - 3 x 0.5 x 20 Hex SHCS -- 20NHX	4
7	M5 GRUB SCREW	B18.3.6M - M5 x 0.8 x 10 Hex Socket Flat Pt. SS --N	2
6	M3 GRUB SCREW	B18.3.6M - M3 x 0.5 x 10 Hex Socket Flat Pt. SS - -N	2
5	QSTS Retainer ring 2	AISI 1080 STEEL	1
4	QSTS Retainer ring 1	AISI 1080 STEEL	1
3	QSTS Eccentric Bush 1	BRASS	1
2	QSTS Eccentric Bush 2	AISI 1080 STEEL	1
1	QSTS Bush 3	AISI 1080 STEEL	1

Scale: 1.5:1 on A3	University of Cape Town Department of Mechanical Engineering			
Drawn By: Muhsin Osman	All un-toleranced dimensions to adhere to ISO 2768-m	Title: Double eccentric bushing design		
Checked :	Assembly drawing	Drawing Number :	Rev. : A	Sheet : 1 of 1

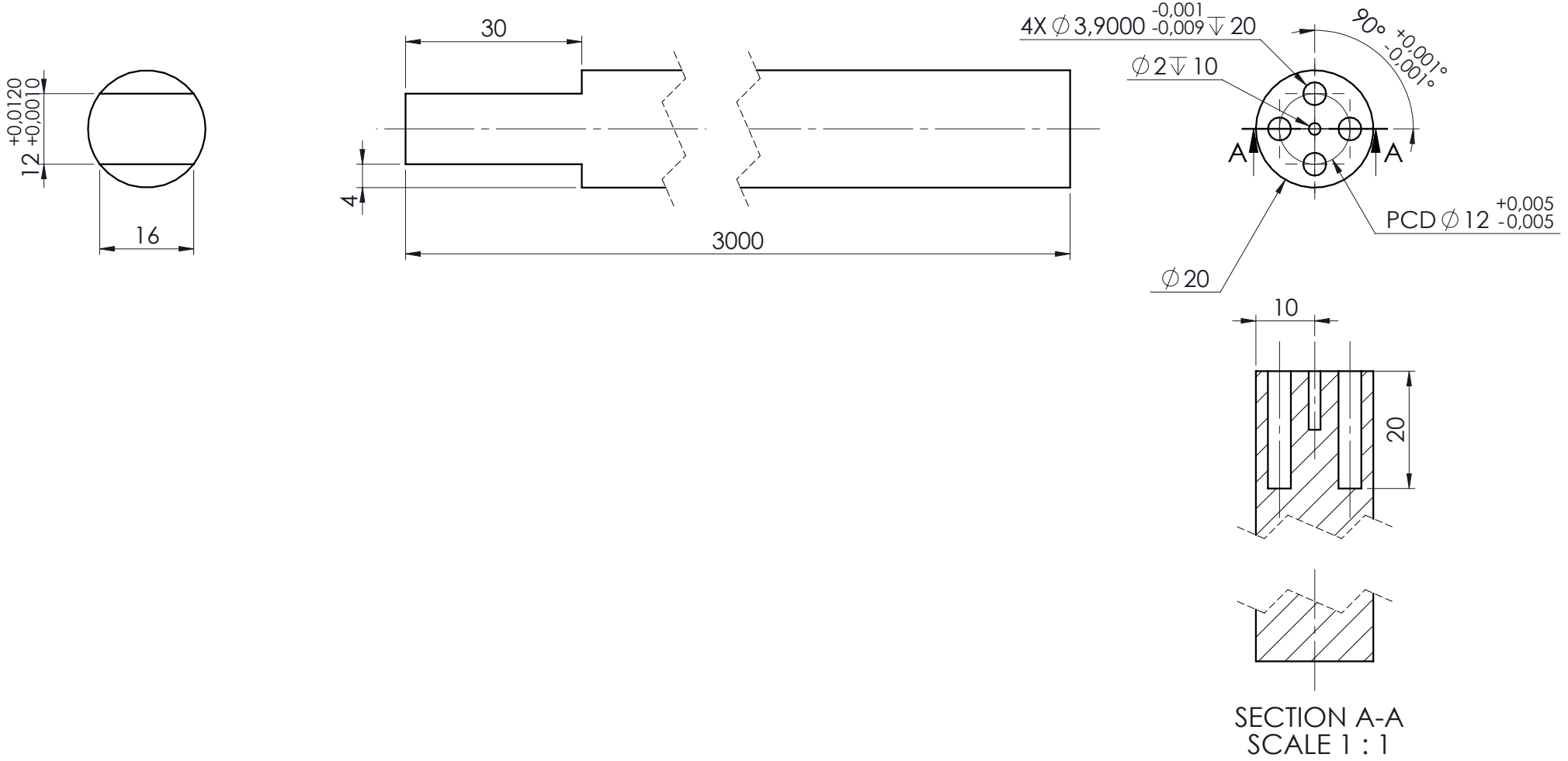

	Scale: 1:50 on A4	University of Cape Town Department of Mechanical Engineering			
Drawn By: Muhsin Osman		All un-toleranced dimensions to adhere to ISO 2768-m	Title: Input bar		
Checked :		Material : Aluminium 7075	Drawing Number : FD 1	Rev. : A	Sheet : 1 of 1

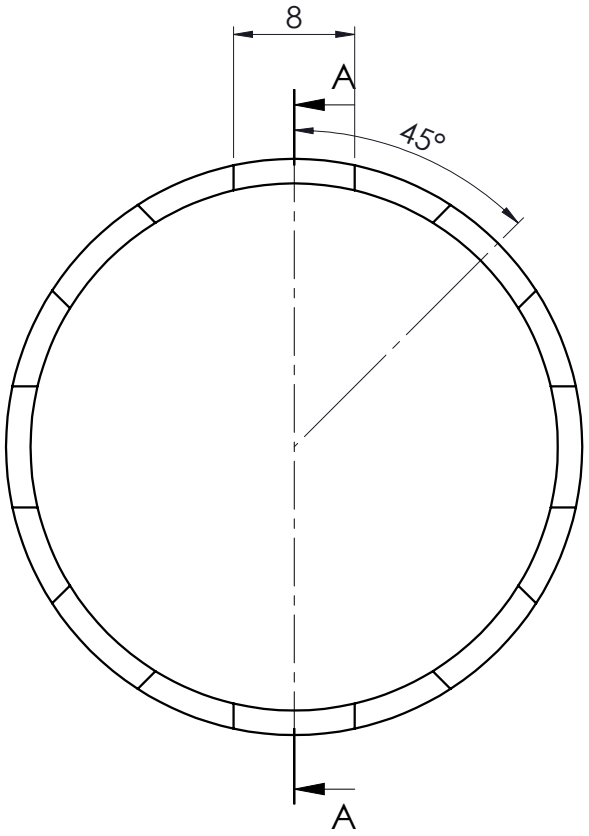

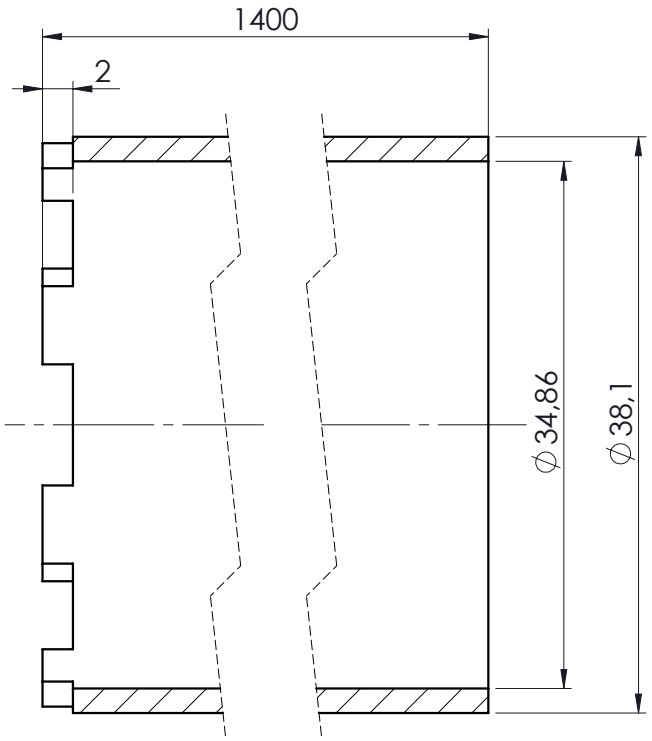

SECTION A-A
SCALE 2 : 1

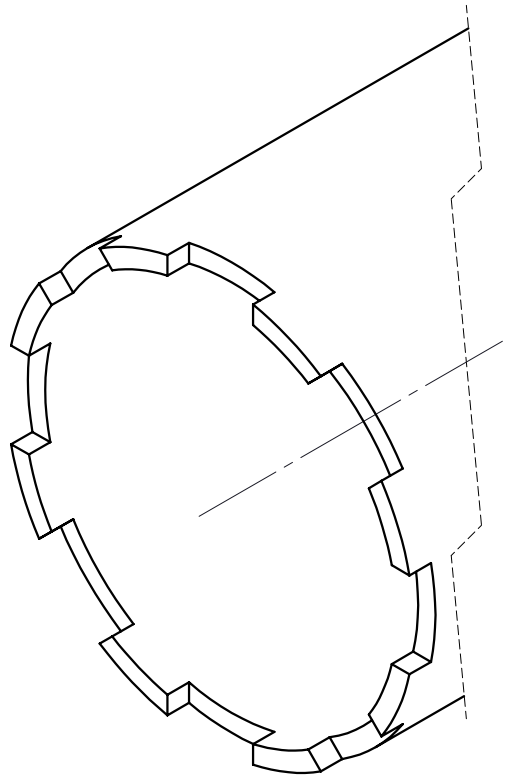

NOTE:
8 X 8mm slotted keyways (2mm deep)
evenly spaced at 45 degrees apart.

Aluminium 6061 OD 38.1 WT 1.62 is standard tube

Scale: 1:20 on A4	University of Cape Town Department of Mechanical Engineering			
Drawn By: Muhsin Osman	All un-toleranced dimensions to adhere to ISO 2768-m	Title: Outer tube Castle shaped		
Checked :	Material : Aluminium 6061	Drawing Number :	Rev. : A	Sheet : 1 of 1

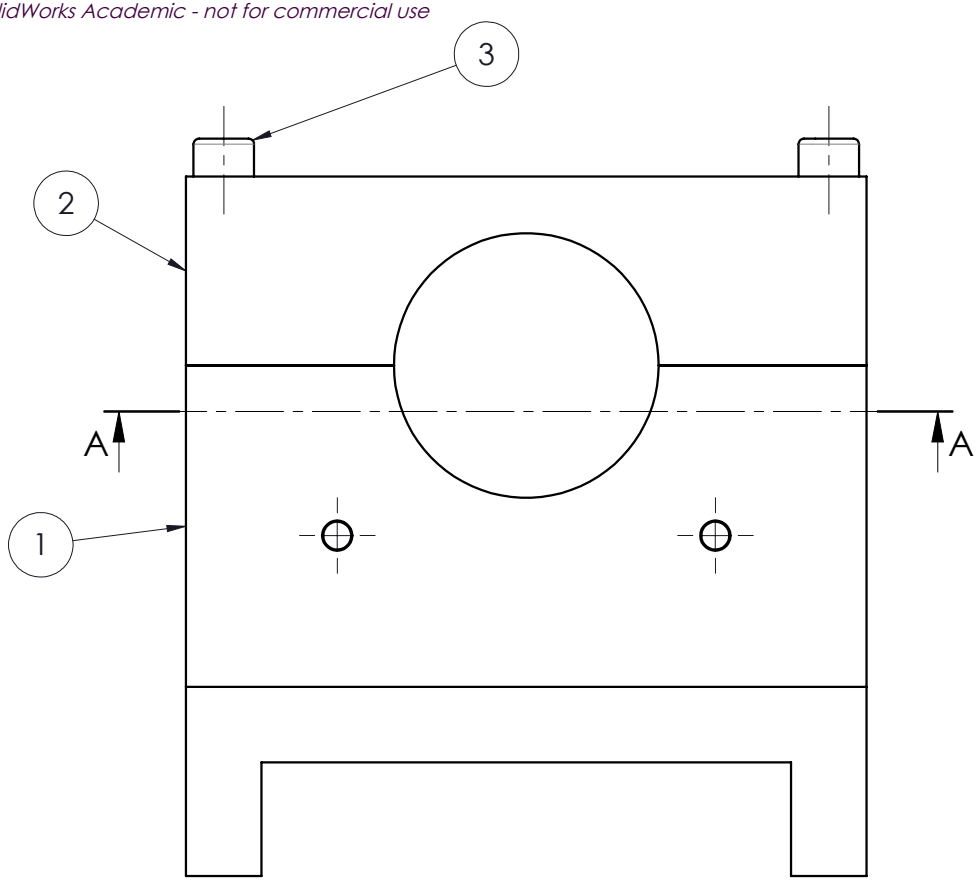

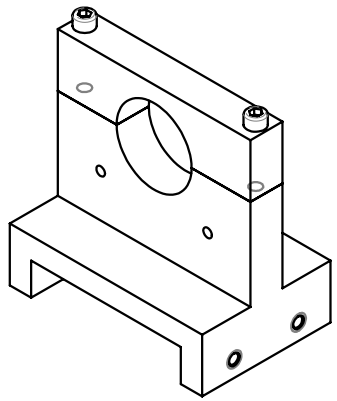

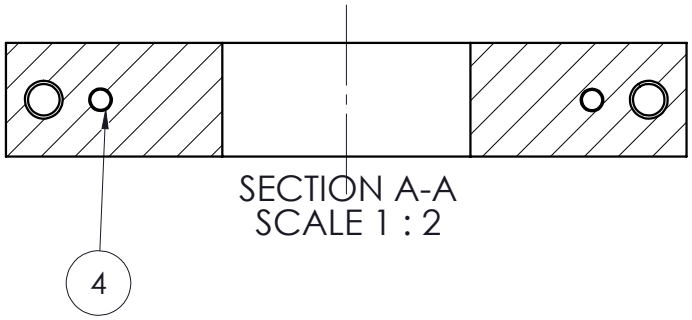

SECTION A-A
SCALE 1 : 2

ITEM NO.	PART NAME	QTY.
4	M6 PARALLEL PIN	2
3	M10 ALLEN CAP SCREW	2
2	BEARING STAND COVER 1	1
1	BEARING STAND 1	1

Scale: 1:5 on A4	University of Cape Town Department of Mechanical Engineering			
Drawn By: Muhsin Osman	All un-toleranced dimensions to adhere to ISO 2768-m	Title: Bearing Stand 1		
Checked :	Assembly Drawing	Drawing Number :	Rev. : A	Sheet : 1 of 1

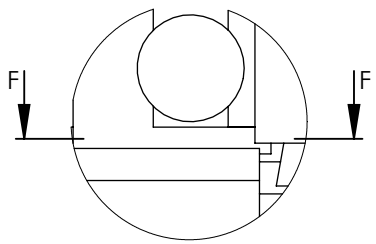

DETAIL E
SCALE 1 : 1

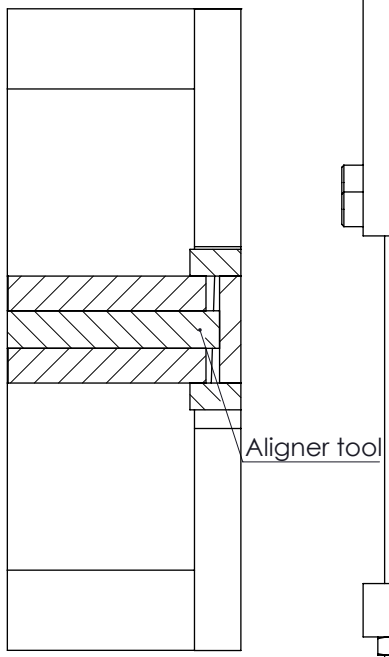

SECTION F-F
SCALE 1 : 1

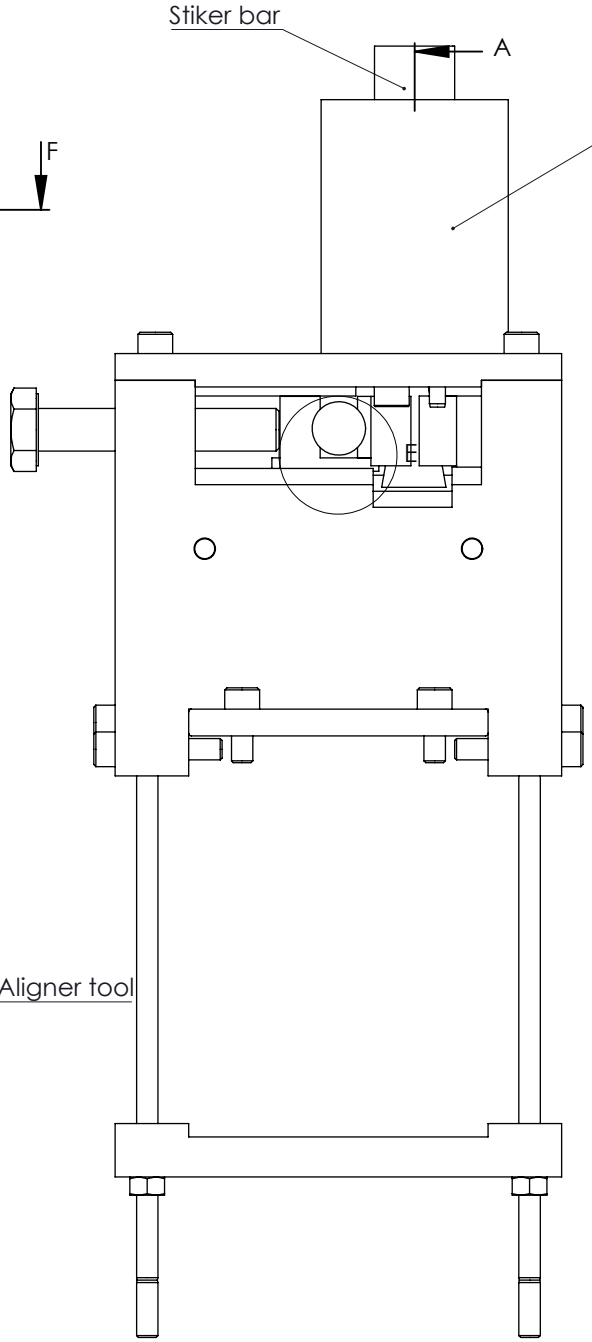

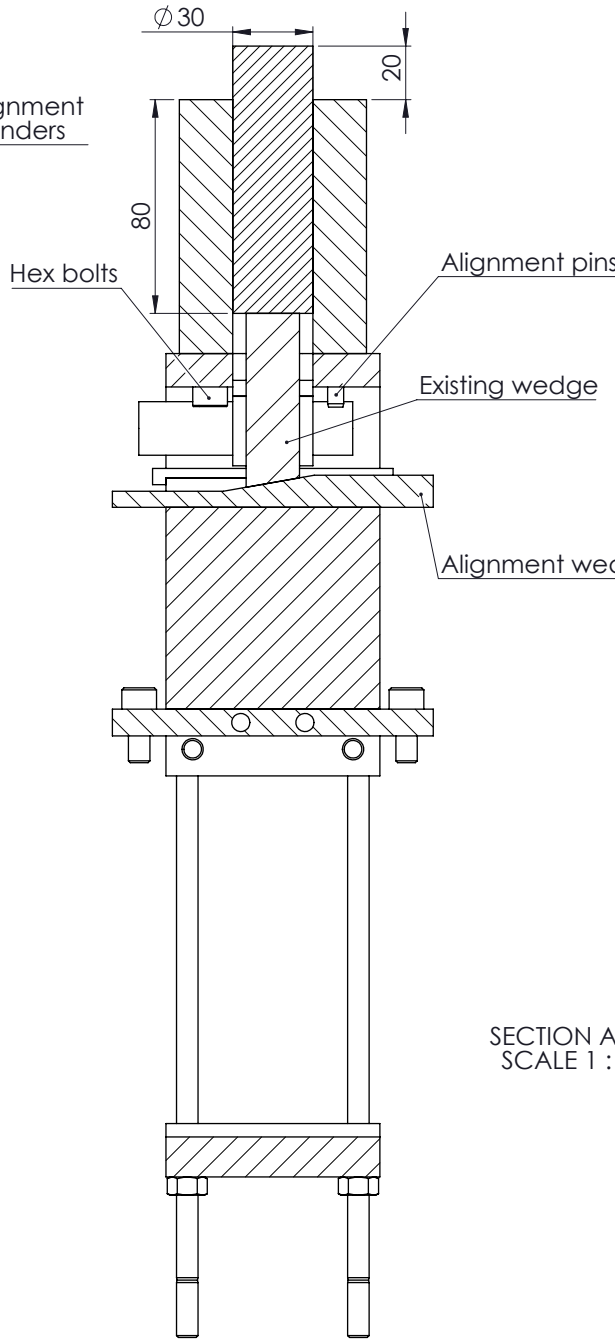

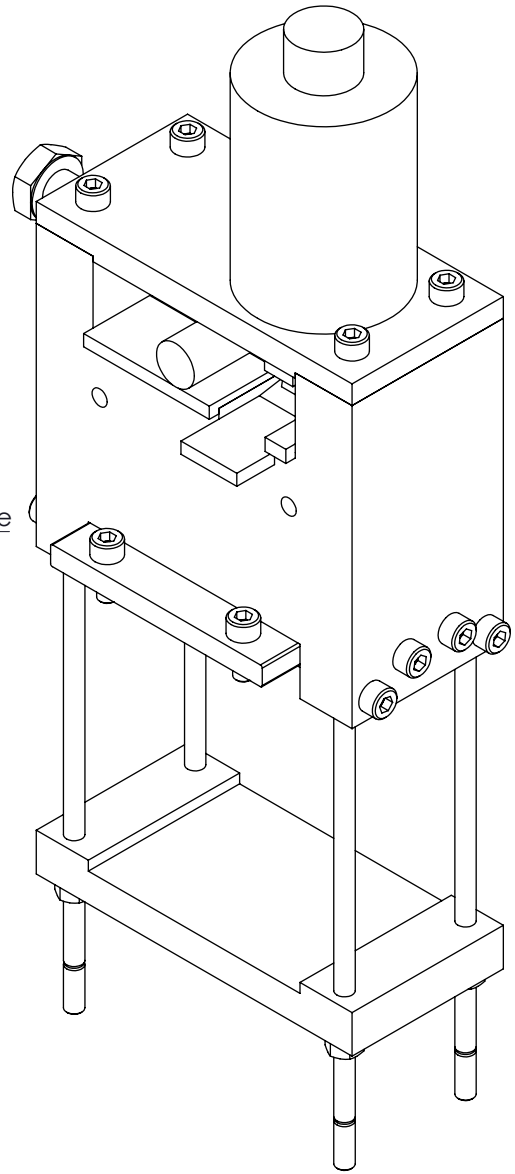

SECTION A-A
SCALE 1 : 2

Scale: 1:5 on A3	University of Cape Town Department of Mechanical Engineering			
Drawn By: Muhsin Osman	All un-toleranced dimensions to adhere to ISO 2768-m	Title: Wedge Release Mechanism		
Checked :	Assembly drawing	Drawing Number :	Rev. : A	Sheet : 1 of 1

Appendix I

Assessment of Ethics in Research Projects Form

This appendix contains the Assessment of Ethics in Research Projects form required for submission.

APPLICATION FORM

Please Note:
Any person planning to undertake research in the Faculty of Engineering and the Built Environment (EBE) at the University of Cape Town is required to complete this form **before** collecting or analysing data. The objective of submitting this application *prior* to embarking on research is to ensure that the highest ethical standards in research, conducted under the auspices of the EBE Faculty, are met. Please ensure that you have read, and understood the EBE Ethics In Research Handbook (available from the UCT EBE, Research Ethics website) prior to completing this application form: http://www.ebe.uct.ac.za/ebe/research/ethics1

APPLICANT'S DETAILS		
Name of principal researcher, student or external applicant		Muhsin Osman
Department		Mechanical Engineering
Preferred email address of applicant:		Muhsin.osman@gmail.com
If Student	Your Degree: e.g., MSc, PhD, etc.	MSc (Eng) (Mechanical)
	Credit Value of Research: e.g., 60/120/180/360 etc.	180
	Name of Supervisor (if supervised):	Ernesto Bram Ismail
If this is a researchcontract, indicate the source of funding/sponsorship		UCT start-up grant
Project Title		Dynamic Torsional Testing of Metals

I hereby undertake to carry out my research in such a way that:

- there is no apparent legal objection to the nature or the method of research; and
- the research will not compromise staff or students or the other responsibilities of the University;
- the stated objective will be achieved, and the findings will have a high degree of validity;
- limitations and alternative interpretations will be considered;
- the findings could be subject to peer review and publicly available; and
- I will comply with the conventions of copyright and avoid any practice that would constitute plagiarism.

SIGNED BY	Full name	Signature	Date
Principal Researcher/ Student/External applicant	Muhsin Osman	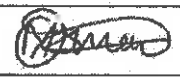	**30 Jan 2018**

APPLICATION APPROVED BY	Full name	Signature	Date
Supervisor (where applicable)	Ernesto Bram Ismail	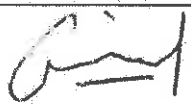	**30 Jan 2018**
HOD (or delegated nominee) Final authority for all applicants who have answered NO to all questions in Section1; and for all Undergraduateresearch (Including Honours).	T. Bello-Ochende		02/08/2018
Chair : Faculty EIR Committee For applicants other than undergraduate students who have answered YES to any of the above questions.			